# SIMULATION AND CHARACTERIZATION OF ZnSe/BeTe RESONANT TUNNELING DIODE ON SILICON

by

MOSHE DAVIS

Presented to the Faculty of the Graduate School of

The University of Texas at Arlington in Partial Fulfillment

of the Requirements

for the Degree of

MASTER OF SCIENCE IN ELECTRICAL ENGINEERING

THE UNIVERSITY OF TEXAS AT ARLINGTON

May 2006

ACKNOWLEDGEMENTS

I would like to first thank Dr. Wiley P. Kirk for giving me an opportunity to work on this project. I would also like to thank him for his guidance and encouragement which immensely helped me throughout my research work. I would like to thank Dr. Meng Tao and Dr. Donald Butler for being part of my thesis committee. I would like to give out a special thanks to members of my research group Bob bate, Kevin Clark, Eduardo Maldonado and other members of the group for their contributions which helped me during my research. I would like to thank Dr. Nasir Basit for training on equipment used in the clean room, Nancy Michael for training me on the wire bonder and other colleagues at nanoFAB for their co-operation and help.

I would like to thank my friends and family members for their patience and encouragement. I would like to thank my brother Charles, my mother Victoria and my father Devarajulu to whom I dedicate this thesis.

April 13, 2006

ABSTRACT

SIMULATION AND CHARACTERIZATION OF ZnSe/BeTe

RESONANT TUNNELING DIODE ON SILICON

Publication No. _____

Moshe Davis, M.S.

The University of Texas at Arlington, 2006

Supervising Professor: Dr. Wiley P. Kirk

ZnSe/BeTe resonant tunneling diodes were grown on silicon with a $Zn_xBe_{1-x}Te$ buffer layer using MBE (Molecular Beam epitaxy). These devices were processed and characterized. The devices showed multiple NDR (negative differential resistance) regions at room temperature with PVR (Peak to valley ratios) between 1.01 to 1.23. Variations to the structure were made in growth and their corresponding current-voltage characteristics were studied. The ZnSe/BeTe resonant tunneling diode showed asymmetrical current voltage characteristics for positive and negative biases. The sources of asymmetry were investigated during fabrication and with the help of simulations. The Al/ZnSe contact was confirmed to be ohmic contact when the

aluminum is deposited in-situ in the MBE chamber. Low temperature measurements were done on the samples and additional NDR regions were observed at 3.2K.

NEMO (Nano-electronic modeling) a quantum device simulator was used to model the experimental current-voltage characteristics of the device. The $sp^3s^*$ tight binding parameters which define the band structure of a material were implemented in NEMO and optimized to get the desired band offsets. The addition of no-common atom interfaces of BeSe and ZnTe to the ZnSe/BeTe hetero-structure were found to qualitatively model the experimental characteristics. The other sources of asymmetry in current-voltage characteristics such as non-equivalent interfaces, asymmetric doping and asymmetric thickness were studied using NEMO.The most important factor contributing to the asymmetry in NEMO current-voltage simulations were found to be the alternating interfaces of BeSe and ZnTe. Thermally assisted tunneling and the effect of Fermi-level raising on PVR were studied using NEMO.

TABLE OF CONTENTS

LIST OF ILLUSTRATIONS

LIST OF TABLES

# CHAPTER 1

# INTRODUCTION

## 1.1 Resonant Tunneling Diodes

Today's state of the art electronic devices have to be continuously scaled to meet the requirements of performance, size and cost. When the size of the system becomes comparable to the electron wavelength quantum effects dominate the transport. Conventional mainstream CMOS technology has already reached the nanometer range and hence the quantum limit. Device working becomes more and more complex as the feature sizes shrink. There has been a great deal of research going on in the replacement for the workhorse of the semiconductor industry-The MOSFET. To meet the challenges of the semiconductor industry the field of nano-electronics has emerged to be a successful one.

After the observation of tunneling phenomenon in semiconductor superlattice by Tsu and Esaki [1] there has been a lot of research going on in this area. The introduction of MBE (molecular beam epitaxy) has opened doors for band-gap engineering and quantum well hetero-structures. Resonant tunneling diodes (RTD) are double barrier quantum well devices grown by MBE. RTDs have exhibited excellent performance characteristics superior to other emerging nano-electronic devices.

RTDs show a NDR (negative differential resistance in their current voltage characteristics which is useful in many oscillator applications. The output characteristics of an RTD have a peak and valley which has been used in memory and logic applications.

Successful working of RTDs have been realized in III-V semiconductors [4, 5]. RTDs using II-VI semiconductors [6] and Si/SiGe [7] have also been demonstrated. There is a requirement for modeling and simulation of quantum electronic devices to understand the quantum transport in these devices. NEMO (nano-electronic modeling) is a powerful quantum device simulator which has been used here [8].

### 1.1.1 Theory of resonant tunneling diodes

Resonant tunneling diodes are double barrier quantum well devices. There are fabricated by bringing together two materials of different band-gaps together such that the conduction band profile has two barriers and a quantum well in between them. A typical conduction band profile is shown in Fig 1.1. A RTD has three regions emitter, active region and the collector. The active region consists of the barriers and the quantum well. Usually the barriers are made of a large band-gap material and the emitter, quantum well and collector are made of a smaller band-gap material. The emitter and collector are doped to have a reservoir of electrons

There are quasi-bound states or resonant states are formed in the quantum well due to the confinement in the growth direction. The requirement for tunneling through a barrier is that the electron should have an available state to tunnel through and the barriers should be sufficiently thin. A typical current-voltage characteristic of a RTD is

shown in Fig 1.2 having three regions named A, B and C. The band-bending due to the applied bias is shown in Fig 1.3.

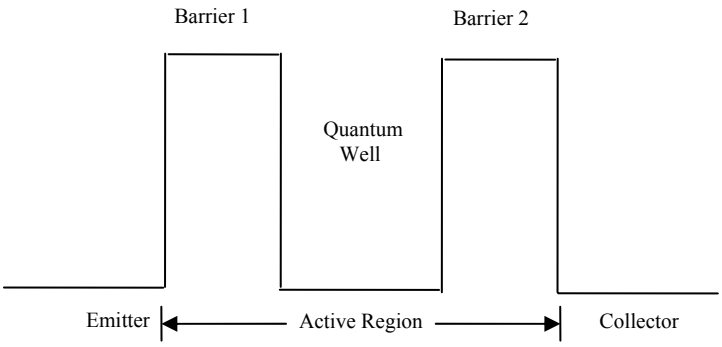


Fig 1.1 Conduction band profile of a typical RTD

The working of an RTD will be explained using Fig 1.2 and Fig 1.3.Suppose we apply a positive bias to the collector, this will cause the bands to bend. If the Fermi-level in the emitter is below the quantized state in the well there will be only current from thermal carriers or other transport this corresponds to the 'A' in Fig 1.2 in the output characteristics and Fig 1.3 a) in terms of band-diagrams.

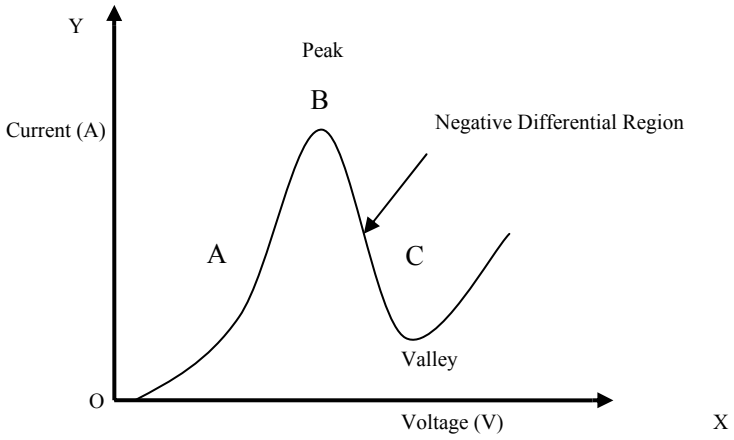


Fig 1.2 Typical current-voltage characteristics of RTD

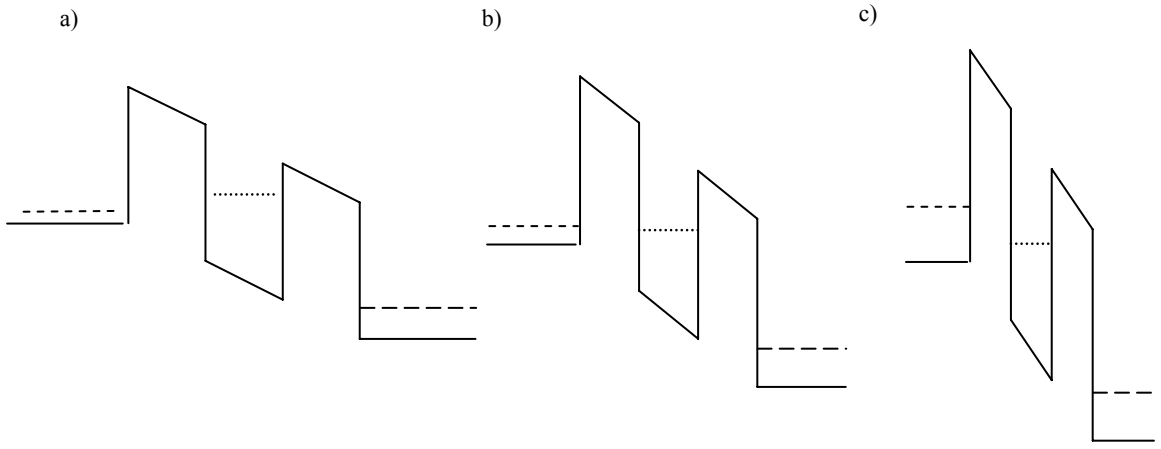


Fig 1.3 a) RTD before resonance b) RTD in resonance c) RTD out of resonance

Now suppose we apply more bias to the collector and this causes the Fermi-level in emitter to come in resonance with the quantized state in the well this causes the electrons to tunnel through the barriers and cause a peak in the current-voltage characteristics in region 'B' of Fig 1.2, this corresponds to Fig 1.3 b).Some more bias is applied and causes the Fermi-level in the emitter to go out of resonance with the quantized state in the emitter shown in Fig 1.3 c), this causes the current in the output characteristics to decrease this region is called NDR (Negative differential resistance) represented in Fig 1.2 as region 'C'. The current will decrease to a point called the valley current of an RTD and after will increase till it breaks-down or goes to a peak and valley if there is another quantized state in the well. The number of NDR regions in the characteristics depends on the number of quantized states present in the well.

It is well known that when dimensions of semiconductors or devices are comparable to the electron wavelength classical physics cannot be applied to explain the

transport phenomenon, this is where the quantum physics comes into the picture. Tunneling of electrons through a barrier is a quantum-mechanical phenomenon.

During fabrication the dimensions in the growth direction are confined in the nanometer range for the active region of RTD hence they exhibit a 2D density of states, whereas the emitter and collector have 3D density of states. Due to low dimensionality in these structures the electron's wave nature plays an important role, because of the wave nature of electrons quantum phenomena such as interference, tunneling and energy quantization are exhibited in RTDs.

The most important characteristic feature of RTDs is NDR (negative differential resistance). The emitter region has a sphere in the k-space and the quantum well has a 2D circle in the k-space. When the electrons are injected from the 3D emitter into the 2D quantum well the transverse momentum is conserved, where as the momentum along the direction of motion of electron is lost. Suppose the transverse momentum is given by $k_{\|} = \sqrt{k_y^2 + k_z^2}$ , the energy in the 3D emitter can be given by

$$E_{3D} = E_C + \frac{\hbar^2 k_X^2}{2m^*} + \frac{\hbar^2 k_{\|}^2}{2m^*} \quad \text{----------(1)}$$

where $k_x$ is the longitudal momentum in the direction of motion or growth. $E_C$ is the conduction band edge and $m^*$ is the effective mass assumed to be constant in the emitter and quantum well. The energy in the quantum well can be given by

$$E_{2D} = E_n + \frac{\hbar^2 k_{\|}^2}{2m^*} \quad \text{----------(2)}$$

Where $E_n$ is the $n^{th}$ energy level in the well.

As we can see from the above equations $k_x$ component is lost when moving from 3D emitter to 2D quantum well. Suppose the is an energy state $E_o$ (n=0) in the well and is available, tunneling will occur only for the electrons with momenta disk $k_x = k_o$ where is given by

$$k_0^2 = \frac{2m^*(E_0 - E_C)}{\hbar^2} \quad \text{----------} \quad (3)$$

When $E_o = E_C$ and $k_o = 0$ the tunneling electrons are maximum and when further the bias is increased the electrons cannot tunnel through without conserving transverse momentum. It can also be thought of the intersection of the 2D momentum disk and the 3D sphere in the emitter for tunneling to happen as shown in Fig 1.4.The NDR is a consequence of conservation of crystal momentum [3].

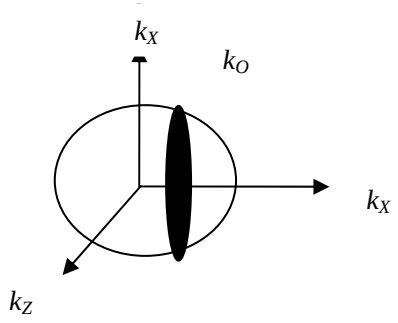


Fig 1.4 k-space showing 3D emitter sphere and 2D momentum disk $k_o$

The current contribution from electrons can be from the following processes [3]

a) When the incident energy in the emitter is in resonance with the resonant energy level in quantum well electrons can tunnel through and produce current.
b) Between the emitter and the first barrier there is a 2D triangular potential well formed during band bending, electrons can be scattered into states in this potential well. Electrons can absorb a phonon and tunnel through the resonant level, this is 2D triangular to 2D quantum well tunneling process.
c) Electron with a certain energy can interact with a lattice vibration and emit a phonon and tunnel through the resonant level.
d) Electrons with sufficient energy can overcome the barriers using thermal energy and cause current in the output.
e) Electrons have a finite probability to tunnel through the barriers even if there are no resonant energy levels in resonance with the emitter Fermi level. This current is responsible for the valley current in RTDs.

Resonant tunneling can be explained in the simplest form by the theory of global coherent tunneling. The energy levels or quantized states in the quantum well can be found by applying boundary conditions for different regions of potentials to the time independent effective mass Schrödinger equation. The transfer matrix method is used to to calculate the transmission probability and the transmission coefficient as described in [2].The tunneling current density will be proportional to the 2D density of states given by

$$J \propto (E_F{}^L - E_o) \quad \text{----------(4)}$$

Where $E_F{}^L$ is the local Fermi-energy in the emitter or left reservoir

The tunneling current is given by the Tsu-esaki expression,

$$J = J_R - J_L \text{ ----------(5)}$$

'$J_R$'is the current density from right and '$J_L$' is the current density from the left.'J' represents the total current transmitted through the device.

The transmission probability and transmission coefficient can be derived using the transfer matrix method given in [2].The Schrödinger equation for the double barrier heterostructure. The potential distribution of RTD is divided into small steps and wave functions for these individual sections is solved using the boundary conditions. The coefficients at the emitter and collector regions are related by the transfer matrix given by, where '$A_E$ ' and '$B_E$ ' are coefficients of the wave function from the emitter and collector.

$$\begin{pmatrix} A_E{}^L \\ B_E{}^L \end{pmatrix} = T \begin{pmatrix} A_E{}^R \\ B_E{}^R \end{pmatrix} \text{ ----------(6)}$$

Transmission probability T(E) is given by,

$$T(E) = \frac{m^{*L}}{m^{*R}} \frac{k^R}{k^L} \frac{(A_E{}^R)^2}{(A_E{}^L)^2} \text{ ----------(7)}$$

Where k and $m^*$ are the complex wave numbers and effective masses of emitter and collector.

The current density is given by the following equations,

$$J_R = \frac{1}{2\pi^2} \int_0^\infty k_{\|} dk_{\|} \int_0^\infty dk e v_z T(E) f_l(k_{\|}, k)[1 - f_R(k_{\|}, k)] \qquad (8)$$

$$J_L = \frac{1}{2\pi^2}\int_0^{\infty} k_{\parallel} dk_{\parallel} \int_{-\infty}^{0} dk e v_z T(E) f_l(k_{\parallel}, k)[1 - f_L(k_{\parallel}, k)] \qquad (9)$$

Where $f_{L,R}(k)$ is the Fermi-distribution functions in the emitter and collectors given by,

$$f_{L,R}(k) = \frac{1}{1 + e\left(\frac{E(k) - E_F^{L.R}}{k_B T}\right)} \text{ ----------} (10)$$

$$v_Z = \frac{1}{\hbar}\frac{dE}{dk} \text{ ----------} (11)$$

The performance characteristic of a RTD is called PVR (peak-to-valley ratio).This is simply given by the dividing the peak current and the valley current of the NDR region. Higher the PVR better the device. Another figure of merit of RTDs is peak current density which depending on applications needing higher or lower current densities.

$$PVR = \frac{I_{peak}}{I_{valley}} \text{ ----------} (12)$$

The current density and transmission coefficients were obtained using the global coherent tunneling theory which excludes scattering events, electron-electron interaction and space charge build-up. In reality electrons in the RTD are out of phase coherence and hence this model cannot be used to model a realistic device. Other theoretical models were used to model a RTD and they are discussed in the next section

### 1.1.2 Theoretical models of RTDs

There is a need to model quantum well devices in order to improve the characteristics of the device. Understanding the mesoscopic transport within these

devices would be the main motivation. Using this knowledge changes can be made in order to get better performance in quantum devices. Quantum electronic devices rely on modeling programs and simulators because of their structural importance and complicated materials. RTD is an open quantum system with both particle and energy interactions with the environment.

Two main factors which need to be considered for successful modeling RTDs

a) The band-parameters and the associated material parameters such as effective mass, band-offsets, and dielectric constants need to be accurately incorporated.
b) The transport formalism needs to account for all the important transport mechanisms. Approximations and simplifications need to be made without violating the fundamental physical and quantum mechanical laws.

Some models trade-off complexity with computation time which turns out to be inaccurate or non-realistic. The most important mechanisms which affect the output characteristics need to be modeled in order to get close to realistic results. There are two kinds of models depending upon the way the electron interacts with its environment [3].

1) Coherent models
2) Kinetic models

From quantum mechanics we know that an electron can be represented by wave function specified by the amplitude, wave number, energy and phase. The time evolution can be described by the time independent Schrödinger equation. When an electron interacts with phonons its phase is changed and it is impossible to account for phase change for all the electrons in the device. According to quantum statistical theory

this changes in state can be characterized by density matrix, Wigner functions and Green's functions.

While modeling a RTD one needs to represent the electron states in the device, this is called the 'model function'. The difference between models lies in the model function. The model function in coherent models is usually the envelope functions and in kinetic models, density matix, Wigner or Green's functions are used [3].

The central equation for the envelope function models is the effective mass Schrödinger equation. In this model the envelope wave function is calculated by integrating the crystal potential with the response of carriers to an external force, this neglects the rapidly varying potential which is an approximation. Another approximation of the envelope function model is that it is limited to pure state calculations, hence it assumes that the phase of the electron does not change during transport. More recent models have incorporated electron correlation and exchange potential due to interaction of electrons. Some new RTD models using envelope functions have included important physical aspects such as space charge effects, the 2D accumulation layer in emitter formed by band-banding, multi-band effects and phonon scattering. There are different methods for including self-consistent potential and charge distribution in these models described, which improve the device characteristics to a large extent [3].

Multiband effects are important for accurate simulations of devices especially if the transport in the structure is interband transport or in indirect band-gap materials with different band-alignments. One of the most important problem of single band models is

that of non-parabolicity. Single band models predict the second turn on of RTDs at a much higher voltage than experimental data. They also show lower current density by a factor of two or more. Another step was taken to introduce the two-band model to introduce the non-parabolicity [10]. Several attempts in including multiband-effects and phonon scattering but no envelope function based model turned out to be successful. There was a fundamental limitation in the coherent models which cannot accurately predict characteristics for different design parameters of RTDs.

To incorporate multi-band effects Rousseau *et al* introduced the tight binding model approach for RTDs [11]. The semi-empirical tight binding parameters were calculated for different materials by Vogl *et al* [12]. The need to change the approach for representing bands to tight binding method is shown by Boykin *et al* [13]. The ten-band nearest neighbor $sp^3s^*$ parameters proved to be an effective way to describe band properties of materials. Empirical tight binding parameters have been further improved in III-V materials for RTD modeling by Bowen *et al* [14].

The fundamental difference between coherent and kinetic models is that the coherent is a single particle picture which is in a pure or coherent state, whereas the kinetic model is based on a many particle picture which is in a mixed state. The kinetic model is more realistic because it includes the effects of electron-electron and electron-phonon interaction in its mixed states. In kinetic models the device is considered to be a particle ensemble represented by density matrix, Wigner function or Green's functions.

The inspiration for kinetic models is for the proper treatment of inelastic electron-phonon scattering. Density matrix and Wigner functions have been used for the

modeling of RTDs, but none of them proved successful to model RTDs for different RTD parameters. Green's functions seem to be the most successful model function in kinetic models. The comparison of Green's functions and Wigner function in RTD modeling has been explained by Kosina *et al* [15]. The use of (NEGF) non-equilibrium Green's functions for quantum transport modeling has been shown by Datta [16]. The NEGF is used in NEMO (nano-electronic modeling) - a quantum device simulator, which has been used in this work.

### 1.1.3 NEMO simulation tool

NEMO (Nano-Electronic MOdeling) is powerful quantum device simulator specifically developed for RTDs by Applied research laboratory of Raytheon TI systems [17]. NEMO is based on NEGF(non-equilibrium Green functions) using empirical tight binding parameters for generating band structures. NEMO is capable of simulating one-dimensionally confined layered hetero-structures with a spatially varying potential [20].

The non-equilibrium Green functions are the theoretical basis of the NEMO simulation tool. Dyson's equations are used to generate the tunneling formula and hence the current density. The NEGF used in NEMO will be discussed in detail in chapter 4 Lake et at have described the theoretical background of NEMO [18].

NEMO as a quantum device simulation tool has been successful because of proper treatment of extended contacts in realistically long devices including quasi bound states, accurate description of band structure using empirical tight binding parameters, quantum charge self-consistency and numerical integration over the

transverse momentum. NEMO is designed to treat the central active region of device as a non-equilibrium part, this is coupled with the drift diffusion model in the emitters and collectors. Poisson's equations are solved to find the charge distribution and the electrostatic potential; this is iteratively solved with the NEGF to obtain the current density [21].

Some of the main features of NEMO are listed below

1) Constructing a computational model of a one-dimensional two terminal heterostructure device.
2) Calculating current as a function of applied bias.
3) Finding and calculating quantum resonant states in the quantum well.
4) Calculating transmission coefficients through the structure.
5) Display of E-k dispersion for bulk materials from $sp^3s^*$ tight binding parameters.
6) Electron density as a function of position.

NEMO layered structure input window is shown in Fig 1.5. The terminal numbers indicate the emitter, active and collector regions of the RTD. A graded doping typical in RTDs is shown in the emitter and collector.

Layer Arrangement

| | Layer Name | Material System | X-Mole Fraction | DopConc (cm-3) | Thickness (nm) | Monolayers | Roughness (nm) | Terminal Number |
|---|---|---|---|---|---|---|---|---|
| 1 | L0 | Mat1 | 0 | 1e+18 | 30.0298 | 106 | 0 | 1 |
| 2 | L1 | Mat1 | 0 | 1e+17 | 35.1292 | 124 | 12.5 | 1 |
| 3 | L2 | Mat2 | 0.4 | 0 | 4.5328 | 16 | 12.5 | 0 |
| 4 | L3 | Mat1 | 0 | 0 | 8.499 | 30 | 12.5 | 0 |
| 5 | L4 | Mat2 | 0.4 | 0 | 4.5328 | 16 | 12.5 | 0 |
| 6 | L5 | Mat1 | 0 | 1e+17 | 35.1292 | 124 | 0 | 2 |
| 7 | L6 | Mat1 | 0 | 1e+18 | 30.0298 | 106 | 0 | 2 |
| 8 | | | | | | | | |

Fig 1.5 Typical arrangement in NEMO showing thickness, doping and roughness

An example of calculation of resonant states in the quantum well done in NEMO is shown in Fig 1.6

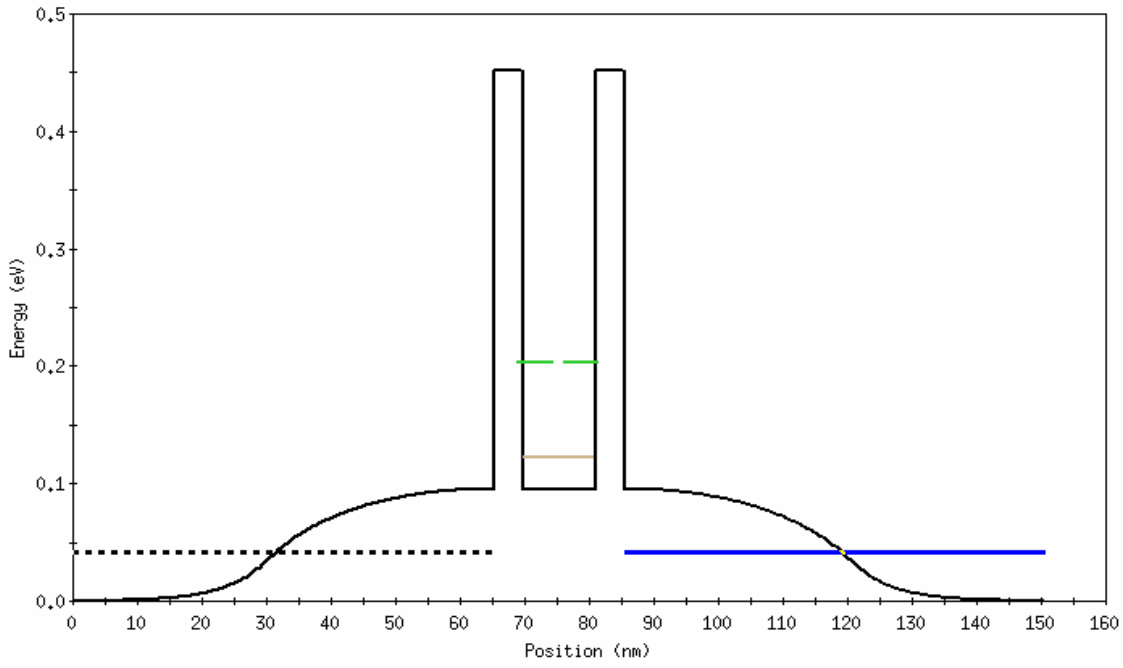


Fig 1.6 Resonant states in quantum well calculated by NEMO for zero bias

The band structures available in NEMO are given below

1) Single band tight binding model.

2) Coupled two band model.

3) $sp^3s^*$ nearest neighbor model.

4) $sp^3s^*$ second nearest neighbor model.

The use of different band structure models depend upon the accuracy needed to simulate these devices. Single band models are very fast, but give an approximate idea of characteristics or resonant states. The two-band model is a better than the single band model. As the model gets more and more accurate the complexity increases and hence the simulation time. The E-k diagram shown in Fig 1.7 shows the parabolicity in single band model and non-parabolicity in full or multi-band models.

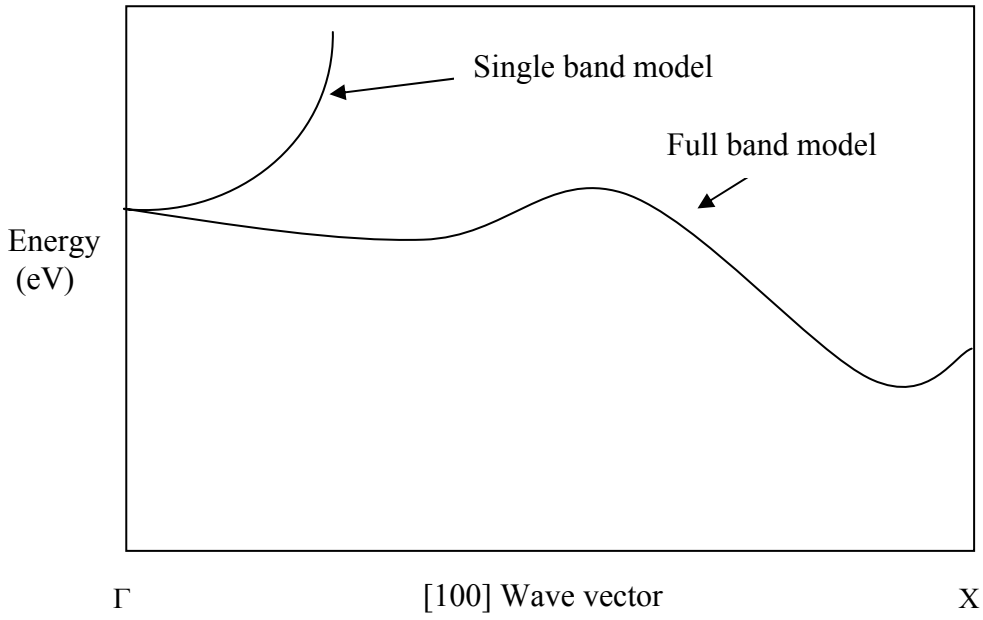


Fig 1.7 E-k diagram showing single and full band models

To accurately model experimental data the use of $sp^3s^*$ tight binding band structure model is necessary. This requires 15 parameters to reproduce the main features

of the conduction and valence band; these include the 2 spin-orbit interaction energies [19]. This is a ten band model which is non-parabolic. NEMO can also simulate $sp^3s^*$ second nearest neighbor model which requires 37 parameters to define the band-structure of a material. In this work we have used the $sp^3s^*$ nearest neighbor model in NEMO and simulated our structures which will be discussed in detail in chapter 4.

The electrostatic models available throughout the device

1) Linear drop model.
2) Thomas Fermi model
3) Hartree model.
4) Hartree plus local density approximation for exchange correlation.

In the linear drop is applied across the device in the first model. The next three potential models the potential is calculated self-consistently with charge distribution. The Thomas Fermi and the hartree models the potential is obtained from the solutions of the poisson's equations. Thomas Fermi model calculates the electron density semi-classically in the contacts and set to zero in the central region, whereas in the hartree model it is calculated quantum mechanically in the central region and user defined to be calculated semi-classically.

The calculation of charge or current requires for integration over the transverse momentum in NEMO we can specify for an analytical or numerical integration. Numerical integration tends to give more accurate quantitative results, but this is also time-intensive.

NEMO handles in-coherent scattering such as alloy disorder, interface roughness, acoustic phonons and polar optical phonons. NEMO uses perturbation theory to incorporate scattering. It can be treated as self-consistent born approximation or a multiple sequential scattering. The effect of alloy disorder and acoustic phonons are small compared to interface roughness and polar optical phonon scattering. The polar optical phonon and interface roughness is defined by a monolayer in which there are cluster islands of cations from a particular material. Incoherent scattering affects the valley current of the RTDs.

## 1.2 Materials and fabrication of RTDs

The introduction of MBE (Molecular beam epitaxy) lead to successful band-engineering and heterostructures. MBE allows for controlled growth of epitaxial layers down to a few monolayers. MBE is capable for binary, ternary and quaternary growth of compound semiconductors. Various materials from the IV group, III-V group and II-VI group are grown with good crystal quality. A heterostucture is formed when two semiconductor materials of different band gaps are brought together or grown on each other. Usually materials grown are lattice matched. If they are not lattice matched they can be grown to a certain critical thickness before they relax to their lattice contents. The quality of the interfaces in RTDs affects the transport because of scattering of electrons. The structural quality of MBE grown heterostructures are important for proper electronic transport.

### 1.2.1 Molecular beam epitaxy

MBE was developed to grown high purity epitaxial layers of compound semiconductors. It uses sources of single elements which are combined to form compounds. MBE is capable of growing high purity layers with abrupt interfaces and a good control over thickness, doping and composition.

MBE is a technique of epitaxial growth by the interaction of atomic or molecular beams on a heated crystalline surface. The requirement of good epitaxial growth is to have highly pure element sources and the growth done in a ultra-high vacuum (UHV) environment. The materials used are 99.9999% pure and vacuum levels in the low $10^{-11}$Torr range. The growth rates of materials are a few Å/s which results in almost atomically abrupt transitions from one material to another.

The solid sources are placed in effusion cells in which they are thermally evaporated onto a heated substrate. The substrate is continuously rotated to improve growth homogeneity. All the parts of the MBE which need to be heated are made of Ta, Mo or pyrolytic boron nitride (PBN) these materials do not decompose or outgas upto temperatures of 1400$^{o}$C. The materials are heated until a certain amount of flux is obtained required for the formation of the compounds. There are separate chambers used for III-V group,II-VI group and IV group materials and they are separated by buffers in which samples can be transferred in-situ. In order to get a stable flux the temperature must be controlled accurately and this is done with Proportion, integral and derivation (PID) controllers. The opening and closing of shutters is computer controlled to a fraction of a second.

There are ion gauges placed in the chamber facing the beams which can measure the beam equivalent pressure (BEP) of the sources. To monitor the residual gases and analyze source beams a mass spectrometer is used. The most important in-situ monitoring tool used in MBE is Reflection high electron energy diffraction (RHEED). The RHEED gun emits high energy electrons which hit the surface a shallow angle, the electrons reflect from the surface and reach the phosphor screen forming a pattern consisting of specular reflection and diffraction indicative of the surface crystallography. RHEED can be used to calibrate growth rates, monitor the arrangement of surface atoms and give a feedback about the surface morphology.

The growth flux rates and RHEED patterns for our particular structure will be discussed in Chapter 2. A typical MBE chamber is shown in Fig 1.8.

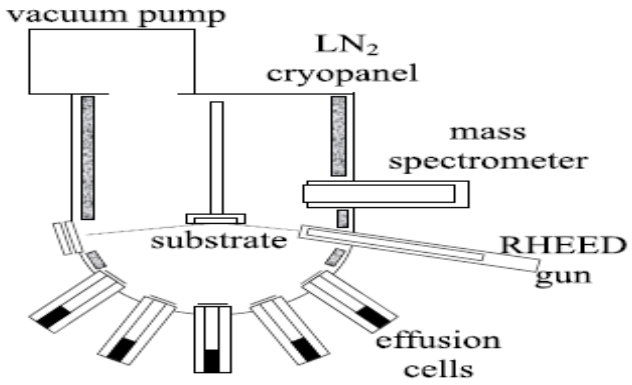


Fig 1.8 MBE chamber

The growth of RTD consists of a quantum well, emitter and collector which are doped. The emitter and collector have a graded doping. The growths of these layers are shown with a conduction band profile beside it in Fig1.9.

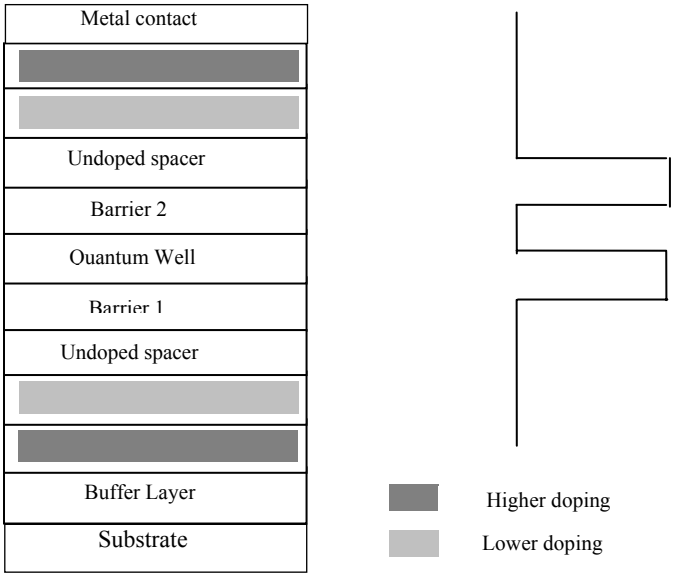


Fig 1.9 Typical layers in RTD fabrication and respective conduction band profile

### 1.2.2 Band alignment

Band engineering in hetero-structures has allowed for increased electronic and optical applications. When two semiconductors of different materials are brought in contact there will have conduction band and valence band discontinuities. These discontinuities are also called conduction and valence band offsets. The requirement for resonant electron tunneling is to have a good conduction band offset.

For the description of different band alignments $E_C$ defined as the conduction band edge and $E_V$ defined as the valence band edge. Depending upon the band gaps

they form different configurations when two semiconductors are brought together. For this description two semiconductors with different band gaps are chosen Fig 1.10.

$$\Delta E_G = E_G{}^B - E_G{}^A \text{ ----------(13)}$$

which is the difference between band gaps of semiconductor 'B' and semiconductor 'A' The valance band offset is given by,

$$\Delta E_V = E_V{}^A - E_V{}^B \text{ ----------(14)}$$

The conduction band offset is given by,

$$\Delta E_C = E_C{}^B - E_C{}^A \text{ ----------(15)}$$

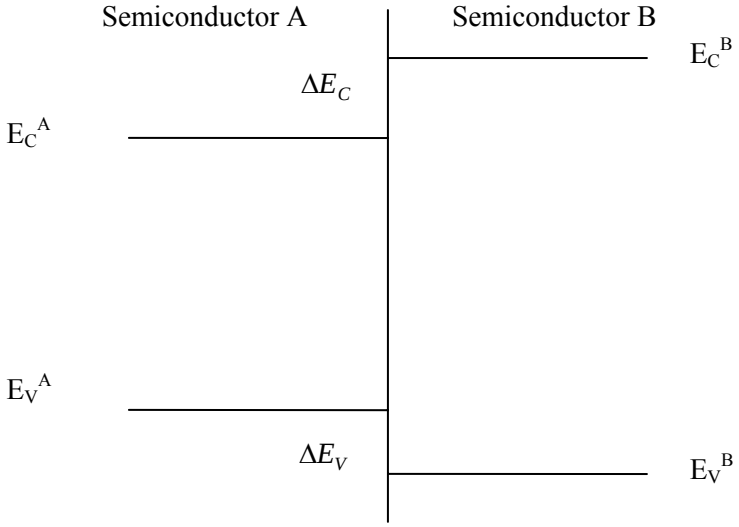


Fig 1.10 Band alignment with two different semiconductors

Band alignments are shown based on examples, the common type of alignment is the Straddling alignment shown for the $In_{0.53}Ga_{0.47}As$-InP system in Fig 1.11.

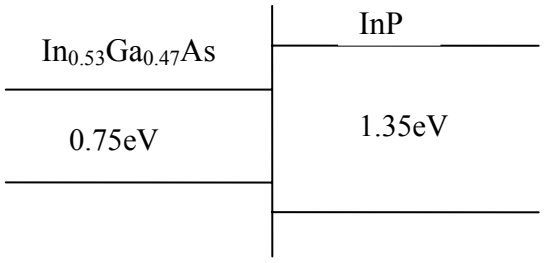


Fig 1.11 Band alignment of $In_{0.53}Ga_{0.47}As$-InP system

The band gaps need not overlap, like the conduction band of the smaller band gap material can be above the conduction band of the higher band gap material or valence might below lower than that of the valence band of the higher band gap material, this is called a staggered band profile an example of it is the AlSb-InAs system shown in Fig1.12

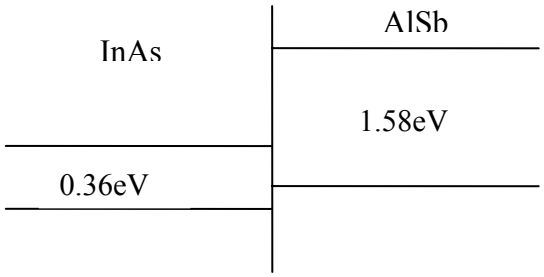


Fig 1.12 Band alignment of InAs-AlSb system

The staggering can become extreme such that the band gaps cease to overlap and this is called broken band gap which is in the GaSb-InAs system. Another nomenclature is used describing super lattices. If the maxima and minimum of the conduction and valence bands lie in the same layers the super lattice is called " Type-I", whereas if the band extrema lie in different layers the super lattice is referred to as "Type-II".

### 1.2.3 Compound semiconductor materials

Usually the barriers are made of a high band-gap material and well, emitters and collector are made of a small band-gap material in order to get a good conduction band offset which is a major requirement of RTDs. The most common materials used for RTDs are III-V group materials such as GaAs, $Al_xGa_{1-x}As$, $In_xGa_{1-x}As$, AlAs, InAs and AlSb. The use of III-V materials used for barrier and well materials has been described Seabaugh [22]. The use of II-VI materials such as $Hg_xCd_{1-x}Te$,HgTe,ZnSe,BeTe, CdTe for RTDs is given in [6,22]. The use of IV group materials such as Si and $Si_xGe_{1-x}$ has also been demonstrated in RTDs [23,24] , but there is a limitation of small conduction band offset to improve the characteristics of these RTDs.

The most of the III-V and II-V RTDs were grown on GaAs or InP substrates. There are very few which have used Si substrates, this is because of the lattice mismatch between the materials grown and substrates. When materials with different lattice constants are grown over each other they get strained in a tensile or compressive way, If they are grown above a certain thickness they relax and form dislocations and defects in the structure. These defects affect the electronic transport across the structure and through the interfaces. The strained semiconductor also alters the curvature of the bands because of the change in the atomic spacing which changes the effective mass of the electrons deviating from its actual bulk material. For successful fabrication of RTDs not only the electronic aspect of it has to be thought but the material and structural aspect must also be given equal importance.

Our goal is to grown II-VI RTDs on Si for the compatibility in CMOS circuits, therefore II-VI materials ZnSe and BeTe were chosen. In our case we use BeTe as barrier since it is has a direct band gap of 4.1eV and the quantum well region is formed using ZnSe which has a band gap of 2.8eV.This material system of ZnSe/BeTe has a good conduction band offset of 2.3eV. These materials are grown on Si with the help of a buffer layer to reduce the lattice mismatch between the II-VI materials and Si. The buffer layer used is $Zn_x Be_{1-x}Te$ with a very small composition of 'Zn'and this buffer layer is known to be lattice matched to GaAs.

The ZnSe/BeTe material system forms a type II band alignment, the conduction band and the valence band offsets of the double barrier hetero structure is shown in Fig 1.13

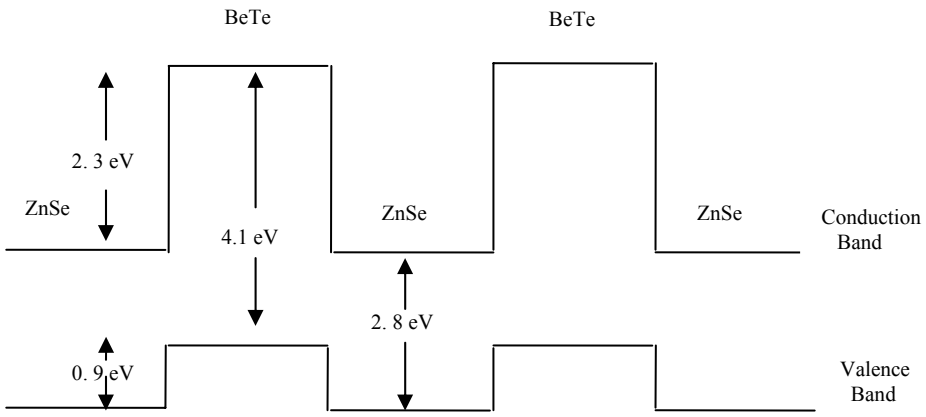


Fig 1.13 Band alignment, band gaps and band offsets shown in ZnSe-BeTe system

## 1.3 Applications of RTDs

RTDs have current voltage characteristics which exhibit NDR and have a peak current and a valley current at different voltages. NDR can be used in oscillator circuits and the peak and valleys are used for logic and memory applications. Some of the applications of RTDs are logic, memory, analog to digital converters and tunnel photodiodes [22].

RTDs have very fast operation because of the tunneling process, because of this they are considered for cache memory and high-speed registers in memory applications. They also have very stable points of operation. Multiple NDR regions in the device serve for multiple valued memories as well as multiple valued logic. These multiple NDRs are usually obtained by stacking RTDs in growth. The use of RTDs for digital circuit applications for logic and memory are shown by Mazumder et al [26] Multi-valued SRAM (Static random access memory) using RTDs by Seabaugh et al [27] and Wei at al [28]. Multi-valued digital applications by Lin et al [32]. Our devices have multiple NDRs which qualify for all multi-valued digital logic and memory applications.

The use of RTDs for analog to digital converter applications is demonstrated by Potter et al [29] and Wei et al [30]. RTDs when biased in the NDR region generate oscillations of very high frequencies which can be used as signal sources. Oscillations upto 712 GHz was described by Brown et al [31].

# CHAPTER 2

## FABRICATION OF RTD

It has been mentioned that our goal was to grow RTDs with excellent characteristics on silicon for compatibility with CMOS circuitry. Two important factors to be considered for compatibility with CMOS is that the structure should be on silicon and the temperatures used for processing should not decompose the grown layers and destroy the device. The growth of ZnSe/BeTe resonant tunneling diodes were done using MBE, the structure was grown on $4^0$ off cut Si (100) substrate. To compensate for the lattice mismatch between the ZnSe layers and Si, a buffer layer of $Zn_{0.06}Be_{0.94}Te$ is used which is lattice matched to GaAs. The lattice constants of ZnSe, BeTe and GaAs are 5.6687 Å and 5.6269 Å and 5.6533 Å respectively. The lattice mismatch between ZnSe and BeTe is 0.74%. The lattice mismatch between ZnSe and GaAs is 0.27%, the mismatch between BeTe and GaAs is 0.46%.The buffer layer is mostly BeTe with a very small composition of 'Zn', BeTe inspite of a 3.5% lattice mismatch with Si grows epitaxially. The structural quality of these hetero structures is important for producing good electronic properties. The choice of materials have been made because of their good conduction band-offset of 2.3eV and also considering their material properties and the ability to be grown on silicon. ZnSe/BeTe RTDs have been grown on GaAs but our group is the first in attempting to grow these devices on silicon [36]

BeTe is known to be covalent in nature which has a high bonding force when used with ZnSe inspite of being ionic in nature produces a closely lattice matched material system. The interest in using ZnSe-BeSe system is well understood for blue-green lasers, but the interesting type-II band-alignment with high conduction band offset and closely lattice matched materials make it interesting for use in RTDs [37,38] .BeTe and ZnSe superlattices have been extensively grown on GaAs and the structural aspects have been analyzed by different groups. The lattice constant of BeTe is smaller than GaAs by 0.46% and that of ZnSe is larger than GaAs by 0.27%.Therefore BeTe and ZnSe are combined to form super lattices with alternating compressive and tensile strain. The strain and structural aspects of short period ZnSe-BeTe superlattices with varying periods and thickness of materials have been studied. The effect of compressive and tensile stress conditions were obtained by growing BeTe and ZnSe of different thickness [39]. The shortest period included in their study is 5 periods and one of their method of growth matches our type of growth which is in a group-VI rich environment. After characterization using High resolution transmission electron microscopy (HRTEM) they found that these particular type of growth and thickness has low density of threading dislocations and no misfit dislocations. Misfit dislocations occurring by cracks were found with higher periods of super lattices. The dislocations were predominately found at the interfaces and very less between the super lattice and the substrate [40]. This gives a structural idea of growing ZnSe-BeTe heterostructures on GaAs or materials that are lattice matched GaAs.

The growth of buffer layer of ZnBeTe plays an important role in our device the to reduce the lattice mismatch which affects the structural properties of the RTD grown on it. The $Zn_xBe_{1-x}Te$ with different compositions of 'x' have been grown on GaAs and characterized using x-ray diffraction by groups and found that a composition of x=0.05 is lattice matched to GaAs and x=0.08 is lattice matched to ZnSe [41]. Growing of 'Se' or 'S' containing compounds which have known to be very reactive and cause very bad interfaces have been eliminated by using 'Te' containing compounds which considerably reduce the defect density in the layers.

## 2.1 Fabrication using MBE

Growth of sample Z 543 is explained below. The growth details of sample Z 543 is given in Fig 2.1.The substrate temperature is represented by '$T_S$'.The rest of the materials are represented by '$T_X$' where 'x' can be the element materials such as 'Zn','Se','Be','Te','As' and '$ZnCl_2$'.The beam equivalent pressure of the sources are represented by '$P_X$' where 'x' is the material.

The growth is done with a p-type Si(100) $4^0$ off-cut wafer. The silicon wafer just acts as a carrier and does not participate in electronic transport of the RTD. Good epitaxial growth of the heterostructure is facilitated by epitaxial growth of silicon, about 500 Å of epitaxial silicon is deposited. The surface is passivated using arsenic to eliminate dangling bonds. The emitter and collector have graded doping, which consists of highly doped 'ZnSe', lower doped 'ZnSe' and un-doped 'ZnSe' Fig 2.1. The doping used is n-type which is incorporated by using '$ZnCl_2$'. The substrate as well as the effusion cells are heated in order for the materials to come from the source and combine

with other materials and form compounds on the surface of the substrate. The growth and quality of the growth is monitored by RHEED (Reflection-high-electron energy diffraction). The diffraction patterns observed in RHEED give us an idea about the surface of the grown layers. The growth in MBE must be two-dimensional; the growth must be deposited layer by layer. This indicates good crystalline growth. In RHEED this is shown by long streaks in the diffraction pattern. The long streaks indicate that there is a two-dimensional growth of layers in MBE. The narrower and brighter the streaks in RHEED the better the crytallinity. A circular or round diffraction pattern in RHEED indicates three-dimensional growth which results in polycrystalline growth , which is not good for heterostructures and their interfaces [42].

The flux of the material is related to Beam equivalent pressure (BEP) which is monitored in the MBE. The fluxes of two species is related to the BEP is given by the following equation [42]

$$\frac{J_X}{J_Y} = \left(\frac{P_X . \eta_X}{P_Y . \eta_Y}\right) . \left[\left(\frac{T_X . M_Y}{T_Y M_X}\right)\right]^{1/2} \text{----------} (**)$$

where '$J_X$' and '$J_Y$' are the fluxes of species 'X' and 'Y', '$P_X$' and '$P_Y$' are the BEPs,'$M_X$' and '$M_Y$' are the molecular weights,'$T_X$' and '$T_Y$' are the absolute temperatures of the source and '$\eta_X$' and '$\eta_Y$' are the ionization efficiencies.

The growth was started with a 500 Å of epitaxial silicon is grown at the rate of 0.09 Å/s with $T_S$=685$^0$C. The surface of silicon is passivated with 'As' at $T_S$=745$^0$C and $T_{As}$= 280$^0$C a streaky 1x2 pattern in the RHEED was seen. Next 1000 Å of $Zn_{0..06}Be_{0.94}Te$ buffer layer was grown with $T_S$=410$^0$C the 'Zn','Be' and 'Te' shutters

were open and growth was done at a rate of 0.61 Å/s, a streaky 1x2 RHEED pattern was observed. The BEP for this buffer layer growth are $P_{Zn}$= 2.1x10$^{-8}$ mbar, $P_{Be}$= 1.2x10$^{-8}$ mbar, $P_{Te}$= 1.3x10$^{-6}$ mbar.

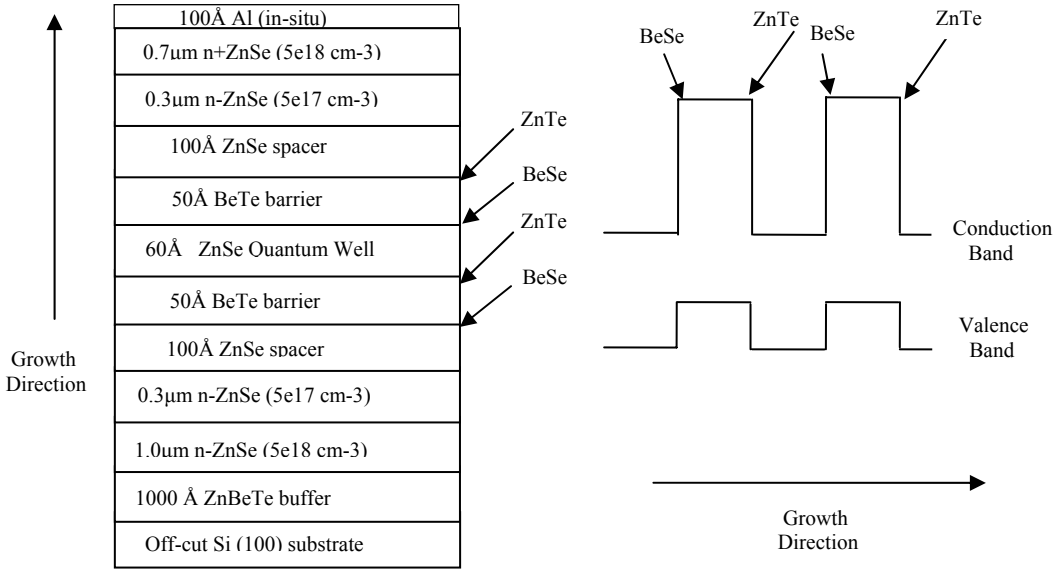


Fig 2.1 Growth details of sample Z 543

The growth of the RTD structure is started with a 1.0um growth of n-ZnSe layer at the rate of 0.85 Å/s with $T_S$=360$^0$C and $T_{ZnCl2}$=152$^0$C by opening the 'Zn','Se' and the '$ZnCl_2$' shutters. The BEPs are given by $P_{Zn}$=5.29x10$^{-7}$ mbar, $P_{Se}$=1.06x10$^{-6}$ mbar, $P_{ZnCl2}$=6.0x10$^{-11}$ mbar. The target doping for such a recipe is 5e$^{18}$cm$^{-3}$.The doping recipes were verified by vanderpau measurements. The next is 0.3um of the lower doped layer of ZnSe in which the fluxes and temperatures are maintained but the doping is done by changing the temperature to $T_{ZnCl2}$=140$^0$C, which is a lower temperature for lower doping. The shutters are opened for a shorter period for lesser thickness. Un-

doped ZnSe layer of 100 Å is grown by opening only ‘Zn’ and ‘Se’ shutters at same parameters.

The next part deals with the barriers and the quantum well. This is more critical because working of the device depends on the quality of interfaces when going from one material to another material. The growth of BeTe on ZnSe which are lattice mis-matched by 0.74% could raise some problems regarding the interface roughness and the chemical nature of materials. The growth quality is known to be greatly increased by terminating a growth in a Group-VI rich environment, therefore when going between two different materials the growth is terminated with ‘Se’ or ‘Te’. The barrier which is 50 Å of BeTe is grown at 0.61 Å/s by opening ‘Be’ and ‘Te’ shutters, a streaky 1x2 pattern was seen. This growth was terminated in’Te’. The next layer is the well region consisting of 60 Å of ZnSe which was terminated with ‘Se’. The second barrier is grown with the same parameters as the first barrier growing 50 Å of BeTe. The next layer is the un-doped ZnSe, the lower doped ZnSe and the higher doped ZnSe which is grown with identical parameters as described before to complete the symmetric structure of the RTD. The ZnSe is known for getting oxidized easily forming an oxide layer on top. In order to avoid this, the sample is transferred in-situ to a III-V chamber and 100 Å of Aluminum is deposited on it. This serves as a protection for the ZnSe layer. Another 2000 Å is thermally evaporated for a thick enough layer for probing measurements and bonding.

It is seen now that the growth of a material layer of either ZnSe or BeTe is terminated either in ‘Se’ or ‘Te’ environment. Now from Fig 2.1 the growth direction

from the un-doped ZnSe below to the BeTe first barrier, the un-doped ZnSe layer is terminated with ‘Se’ and when the ‘Be’ and ‘Te’ shutters are open BeSe interfaces are formed. When BeTe is grown the growth is terminated with ‘Te’, the next well region of ZnSe is grown by opening the ‘Zn’ and ‘Se’ shutters. The interface is now ZnTe. This is also true for other parts. It can be said that when ‘BeTe’ is grown on ‘ZnSe’ the interfaces are ‘BeSe’ and when ‘ZnSe’ is grown on ‘BeTe’ the interfaces are ‘ZnTe’, These interfaces are believed to be 2-3 monolayers. These interfaces neither share a common anion nor a common cation with the hosts and hence a no-common atom system. In a no-common atom system like the ZnSe-BeTe system the interfaces are of a different material and hence different electronic properties such as band gap and band-offsets. In our type of a growth we expect the interfaces to be alternating which is shown in Fig 2.1. These alternating interfaces of BeSe and ZnTe alter the transport of electrons in the structure which affect the overall characteristics of the device. The interfaces can be controlled to an extent in MBE. There is a tendency depending upon the material ‘Se’ or ‘Te’ to be incorporated more than the other, this is why it is difficult to control the interfaces. The way in which the interfaces change the electronic transport in RTD in explained in Chapter 4 using NEMO simulations. The effect of having a mixture of BeSe and ZnTe interfaces, only BeSe or only ZnTe interfaces on the structural aspects [39, 40, 43] will be discussed in detail in Chapter 5.

A total of six samples were grown with variations made in the layers to understand the transport and improve the characteristics. The thickness of layers in the following samples are controlled by reducing the growth times and keeping the BEP

constant. The doping is changed by increasing the temperature of the '$ZnCl_2$' source. The next sample grown was Z 563 is to reproduce the results as above with the same thickness and doping of all layers.

From our characterization and simulations we have found that the thickness of doped layers of emitter and collector were too thick compared to the quantum well size itself , therefore the sample Z 586 the thickness of the doped layers were halved and details are shown below.

Table 2.1 Growth details of sample Z 586

| Material | Thickness (nm) | Doping n-type ($cm^{-3}$) |
|---|---|---|
| Al | 10 | - |
| n+ZnSe | 500 | 5e+18 |
| n-ZnSe | 150 | 5e+17 |
| ZnSe | 10 | - |
| BeTe | 5 | - |
| ZnSe | 6 | - |
| BeTe | 5 | - |
| ZnSe | 10 | - |
| n-ZnSe | 150 | 5e+17 |
| n+ZnSe | 500 | 5e+18 |
| ZnBeTe | 100 | - |
| Si buffer | 50 | - |
| Si | substrate | p-type |

There is a triangular well formed between the emitter and the double barrier heterostructure because of the graded doping and the undoped spacer when the device is biased or in band bending condition. The states formed in this triangular well is called quasi-emitter states and the electrons experience 2D-2D tunneling from this well into the main quantum well. It is known having an un-doped spacer aids in forming the triangular well and increases the PVR (peak to valley ratio) of these devices [2].The

increased 2D-2D tunneling also realizes in sharper resonances in the current voltage characteristics. In sample Z 586 the effect of decreasing the thickness of doped layers changes the width of the triangular well.

Engineering the triangular potential well can get some interesting characteristics. The graded doping done in the contacts affect the current density and the PVR. Apart from changing the thickness of barriers and well in order to increase current density , position of NDRs and PVR the triangular potential well is an additional parameter which can be changed to get better characteristics. The effect of changing the graded doping is studied in the next sample Z 593 in which the lighter doped ZnSe layer was removed and the un-doped spacer was made smaller to 20 Å. Also sample Z 594 in which the un-doped spacer was increased back to 100 Å. Another inspiration for growing samples Z 593 and Z 594 was to eliminate the cause of asymmetry in currently voltage characteristics from asymmetric doping which is discussed in detail in Chapter 5. The details of Z 593 and Z 594 are given below.

Table 2.2 Growth details of sample Z 593

| Material | Thickness (nm) | Doping n-type ($cm^{-3}$) |
|---|---|---|
| Al | 10 | - |
| n+ZnSe | 500 | 5e+18 |
| ZnSe | 2 | - |
| BeTe | 5 | - |
| ZnSe | 6 | - |
| BeTe | 5 | - |
| ZnSe | 2 | - |
| n+ZnSe | 500 | 5e+18 |
| ZnBeTe | 100 | - |
| Si buffer | 50 | - |
| Si | substrate | p-type |

Table 2.3 Growth details of sample Z 594

| Material | Thickness (nm) | Doping n-type ($cm^{-3}$) |
|---|---|---|
| Al | 10 | - |
| n+ZnSe | 500 | 5e+18 |
| ZnSe | 10 | - |
| BeTe | 5 | - |
| ZnSe | 6 | - |
| BeTe | 5 | - |
| ZnSe | 10 | - |
| n+ZnSe | 500 | 5e+18 |
| ZnBeTe | 100 | - |
| Si buffer | 50 | - |
| Si | substrate | p-type |

While doing low temperature measurements it was found that the current density changed with temperature. As the temperature was reduced the current density reduced. To address this problem another sample was grown attacking the problem of thermally assisted tunneling and reduction of type-II transitions by increasing the Fermi-level in the contacts by increasing the doping of the emitter and collector. This also will be discussed in detail in chapter 5. In Sample Z 599 the doping of the emitter and collector is doped to the maximum. The temperature of the $ZnCl_2$ source is increased to $170^0$C. The target doping of the n+ZnSe is 5e+19 $cm^{-3}$ and the target doping of n-ZnSe is 5e+18 $cm^{-3}$. The characteristics pertaining to the above described samples will be discussed in the next chapter.

Table 2.4 Growth details of sample Z 599

| Material | Thickness (nm) | Doping n-type ($cm^{-3}$) |
|---|---|---|
| Al | 10 | - |
| n+ZnSe | 500 | 5.00E+19 |
| n-ZnSe | 150 | 5.00E+18 |
| ZnSe | 10 | - |

Table 2.4 –*continued*

| | | |
|---|---|---|
| BeTe | 5 | - |
| ZnSe | 6 | - |
| BeTe | 5 | - |
| ZnSe | 10 | - |
| n-ZnSe | 150 | 5.00E+18 |
| n+ZnSe | 500 | 5.00E+19 |
| ZnBeTe | 100 | - |
| Si buffer | 50 | - |
| Si | substrate | p-type |

## 2.2 Processing of RTD

Posts processing of the MBE grown layers were done using standard processing techniques such as Photolithography, wet chemical etching, silicon dioxide sputtering and metal deposition described below. A three mask layer process was done to include bonding pads for wire bonding.

Photolithography was done using a Karl suss i-line aligner and positive photo resist for the first layer. The feature size used was 150um diameter. The second and third layer was done using negative photo resist AZ 2020. The sputtering of silicon dioxide is done using a home built RF sputtering machine. Wet chemical etching of ZnSe, BeTe and sputtered $SiO_2$ was done. Aluminum metal was deposited using a NRC thermal evaporator. The processing steps are explained below.

1. Positive photolithography using Shipley S1808, The sample was coated with photo resist at 3500 rpm for 60s, approximately 1um of photo-resist is coated. Pre-bake was done for 60s at 90$^{o}$C.

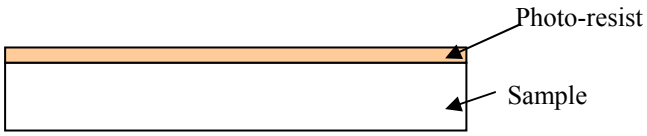


Fig 2.2 Spinning of photo resist

2. Exposure was done using a mask for 3s in aligner with a power of 18W/cm$^2$, after exposure post exposure bake was done for 60s at 110$^o$C.

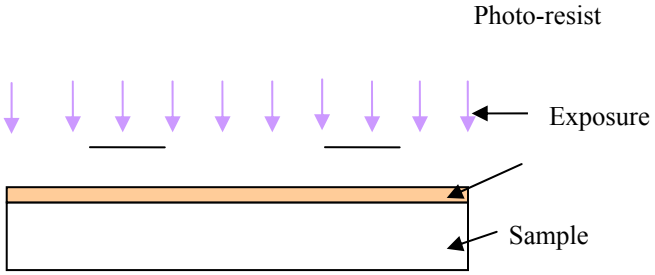


Fig 2.3 Exposure using mask

3. Next the sample is developed in MF 320 for 10-15 s till pattern appears.

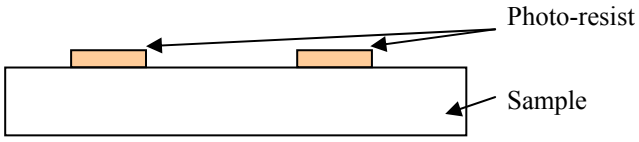


Fig 2.4 Developing of photo resist

4. The RTD layers grown in MBE are protected by the photo-resist and the etching of the Aluminum metal is done first and then the etching of the ZnSe and BeTe layers will be etched till the lower doped layers to form the mesas. Usually the depth is ~1um. The etching is done in small steps and checked with the profilometer. After the etch the photo-resist is stripped off.

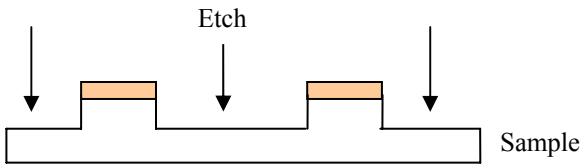


Fig 2.5 Etching the ZnSe and BeTe

The aluminum etch is a wet etch containing phosphoric acid, water, Acetic acid and nitric acid in the ratio 16:2:1:1. The chemical used to etch ZnSe and BeTe is sulphide etch which is a mix of potassium dichromate, sulfuric acid and water with an etch rate of 200 Å/s.

5. In this step isolation layer of silicon dioxide is sputtered all over the sample. The thickness is about 0.2um.

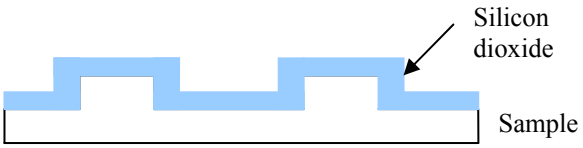


Fig 2.6 Silicon dioxide sputtering

6. A negative photo-resist AZ 2020 is used to pattern the next layer in which windows are etched in the isolation layer smaller than the device size. Device sizes are usually 150um circles and the etch windows are 50um circles. Silicon dioxide is etched using 50:1 hydrofluoric acid. Etch rate was 0.1um/min.

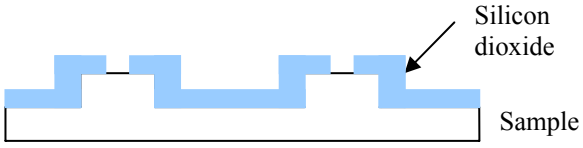


Fig 2.7 Etching silicon dioxide

7. In this step the devices are patterned to have metal covering the devices and are connected to 200um by 200um pads by fingers. These pads are used for wire bonding. The goal was to connect the devices using pads and the bonding place to be away from the devices because the bonding force and temperature was known to damage the devices if bonding was done directly on the devices. Once patterned

metal is deposited and metal-lift-off is done using AZ 400T resist stripper.

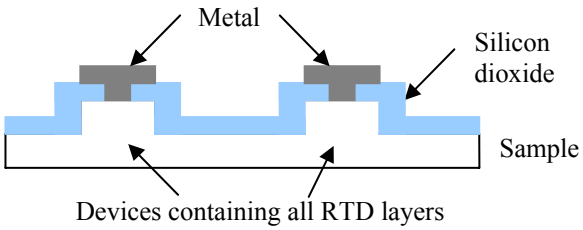


Fig 2.8 Metal deposition and lift-off to make contact to first layer metal

The top view of the sample for an example of bonding pads connected to the device by fingers which is all aluminum metal shown in Fig 2.9.

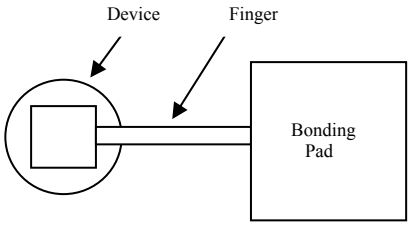


Fig 2.9 Top view showing bonding pads connected to devices by fingers

The etch profile after etching the II-VI layers is shown in Fig 2.10.The fabricated sample using the above process is shown in Fig 2.11.After the fabrication the devices are tested. The devices can be tested in the probe station even after the fourth step of the process. The rest of the steps are done so that these devices can be wire-bonded in packages and measured at low-temperatures in the cryostat.

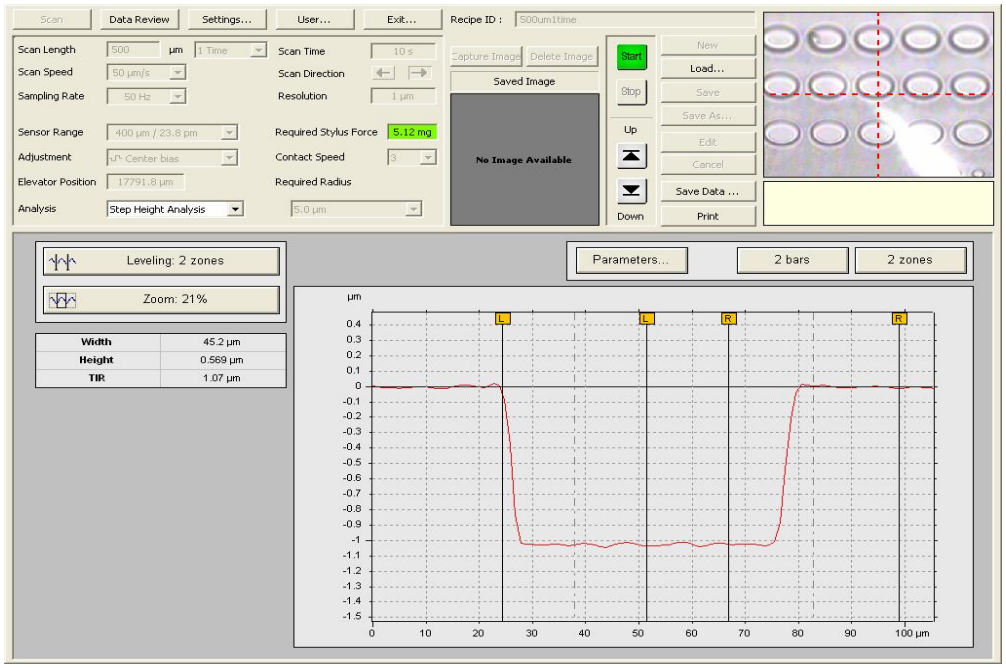


Fig 2.10 Etch profile after etch using profilometer

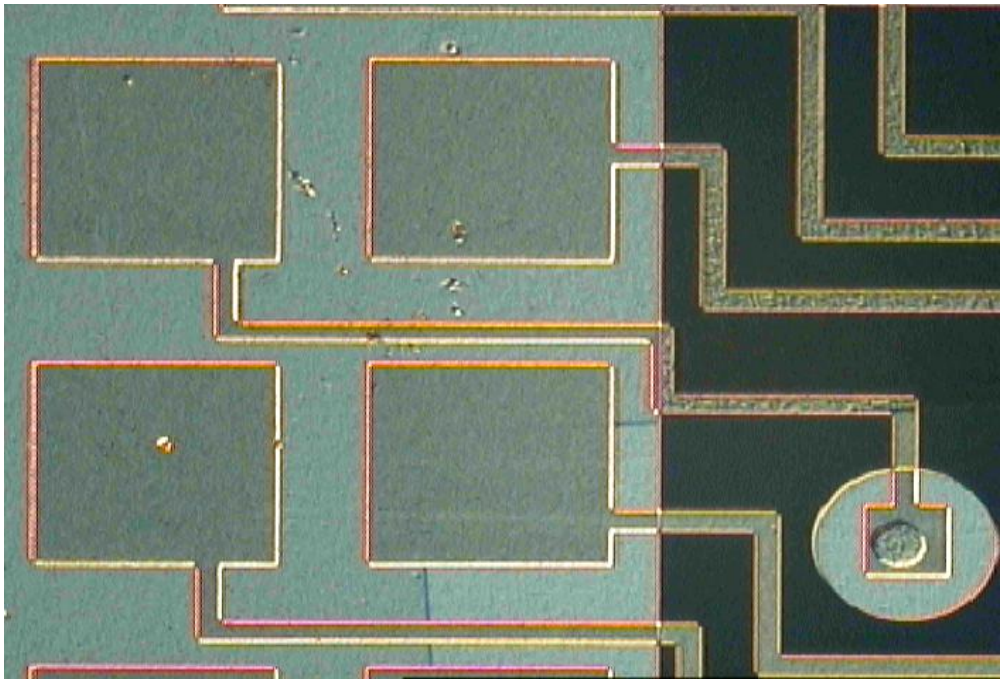

Fig 2.11 Fabricated sample with the above process

## 2.3 Packaging

After final testing the devices are cleaved into individual dies using a titanium tip pen and glued to 16-pin dual in-line packages (DIP) and wire bonded. The wire bonder used is a Kulicke & Soffa thermo sonic ball bonder. The bonds are made using a 1mil thin gold wire. The first bond made is a ball bond and the second bond made is a wedge bond. The sample holder is also heated to facilitate bonding to $110^0$C.

A picture of the wire bonder is shown in Fig 2.12 below. The gold wire rests in a spool which is on top and the wire is pulled through various tension springs and small mechanics and brought through the capillary. The capillary is shown in Fig 2.13 along with the DIP package sitting on the heated chuck.

Fig 2.12 Kulicke & soffa thermo sonic ball bonder

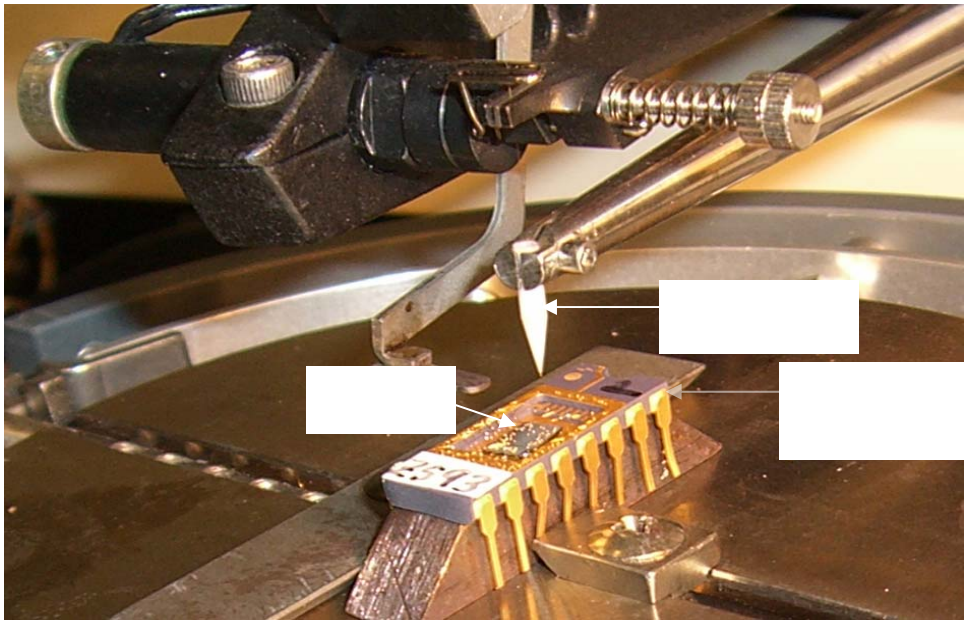

Fig 2.13 Capillary and 16 pin DIP package on chuck

The wire bonder used is a thermo sonic wire bonder which makes use of heat and ultrasonic power to make the bonds. After completion of bonds a spark cuts off the wire melting the wire forming a ball at the edge of the wire, this prevents the ball from coming off the capillary. There is a two-axis motion in which the bonding can be done the height is fixed prior to actual bonding. For the first bond the capillary is made to come above the device to be bonded and the first bond is initiated by sending an ultrasonic wave of a certain power. This causes the ball at the capillary which is in contact with the device top metal to melt and form the bond. The second bond is wedge bond in which the wire is pressed against the surface of the package and is bonded using heat. Examples of the first bond on our RTDs are shown in Fig 2.14, this is a ball bond on top metal aluminum. The second bond is wedge bond on the DIP package is shown in Fig 2.15.

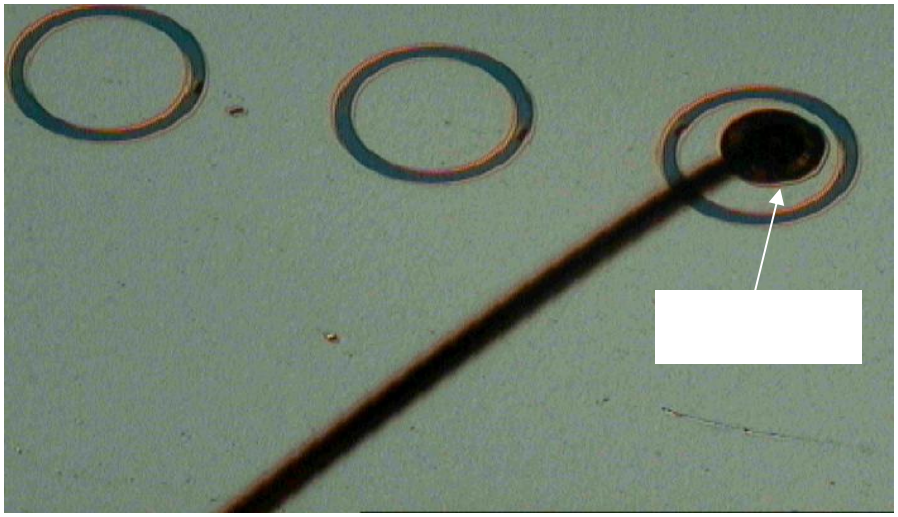

Fig 2.14 Ball bond on sample

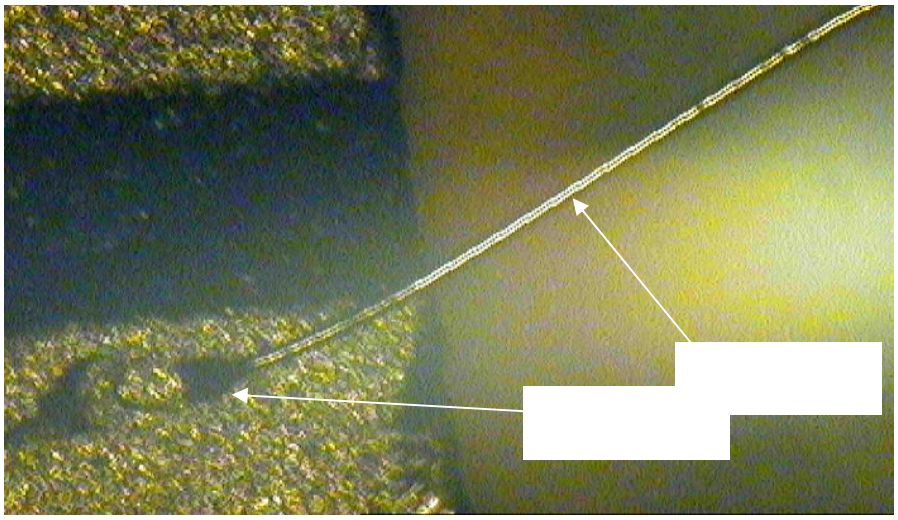

Fig 2.15 Wedge bond on the package lead

There are some parameters which can be controlled for bonding on different surfaces and conditions. The parameters are loop size, force, time and power of the first and second bond. There is also chuck heating capability to help bonding, the substrate can be heated from room temperature to $170^0$C. The ultrasonic power can be adjusted between 1.3W and 2W, the time can be adjusted between 10ms and 100ms and the

force can be adjusted between 10-160g. The external controls convert these above mentioned values into a scale from 1 to 10 in steps of 0.1.The parameters used for our bonding is shown in Table 2.5.

Table 2.5 Bonding parameters

| Bond | Force | Time | Power |
|---|---|---|---|
| First bond | 3.5 | 5.1 | 3.1 |
| Second bond | 5.5 | 5.5 | 6.1 |

Our top layer metal was aluminum and gold was used to bond the devices. The bonding worked well for us but the force and power used by the ultrasonic supply were found to damage our devices and which consists of multi-layers material structure of our RTDs. Our device characteristics were modified by the bonding process. Sometimes the parameters need to be optimized for the particular sample. The chuck temperature can be changed if the devices are not affected by high temperatures. The bond force and power can be changed depending on the device. For our devices since the power and force was suspected to damage the devices. The minimum force, time and power were used for the bonding to happen and these devices seem to be damaged by these forces too. The gold-aluminum bond did not seem to have any purple plague because various other devices were bonded in a similar manner and did not show any change in characteristics. A new process was developed in which the bonding pads were placed away from the device top as shown in previous section in Fig 2.9 and Fig 2.11.This was done in order to eliminate the bonding place to be above the device. Another problem encountered was the sticking of aluminum to insulating layers like polyimide and

sputtered silicon dioxide. The thermally evaporated aluminum did not stick very well to the polyimide and the silicon dioxide and during the bonding process found that the aluminum came off with the first bond. Although aluminum on thermally grown silicon dioxide and silicon seem to stick very well and showed excellent bonds.

# CHAPTER 3

# CHARACTERIZATION

After the fabrication of the RTD, the device is checked for the d.c current-voltage characteristics. In this chapter the characterization method, the current voltage characteristics of the samples and checking of ohmic contacts on n-ZnSe is discussed.

## 3.1 Measurement method and equipment

A d.c voltage is applied and the current is measured across the device using a micromanipulator with probes. The current-voltage characteristics (I-Vs) of RTDs are usually done for both positive and negative biases , the currents obtained represents the electrons moving from the left to the right and right to the left.A typical set-up for I-V measurement is shown below which contains a semiconductor parameter analyzer which is controlled by a computer through HP-VEE software and GPIB cables.

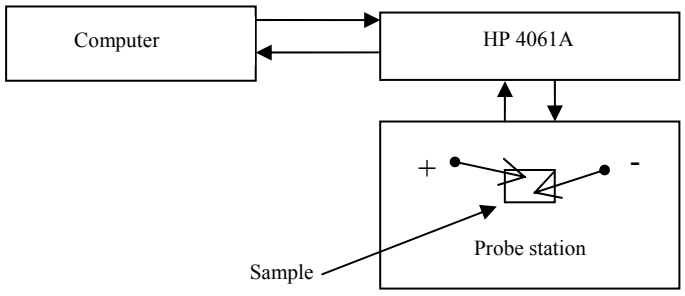


Fig 3.1 Probe station and meter controlled by computer

The HP-VEE program is setup to send the measurement parameters such as range of voltages, voltage steps, step delay and the type of sweep to the instruments and the measured data is sent from the instrument back to the computer where it can be plotted and recorded.

The d.c current voltage characteristics taken from the RTD are done by putting the positive probe on the top of the device and negative probe on a large area contact such that the resistance of the device is much smaller when compared to the large area contact and the current measured will be the current though the device. The diagram for measurement is shown in Fig 3.2.

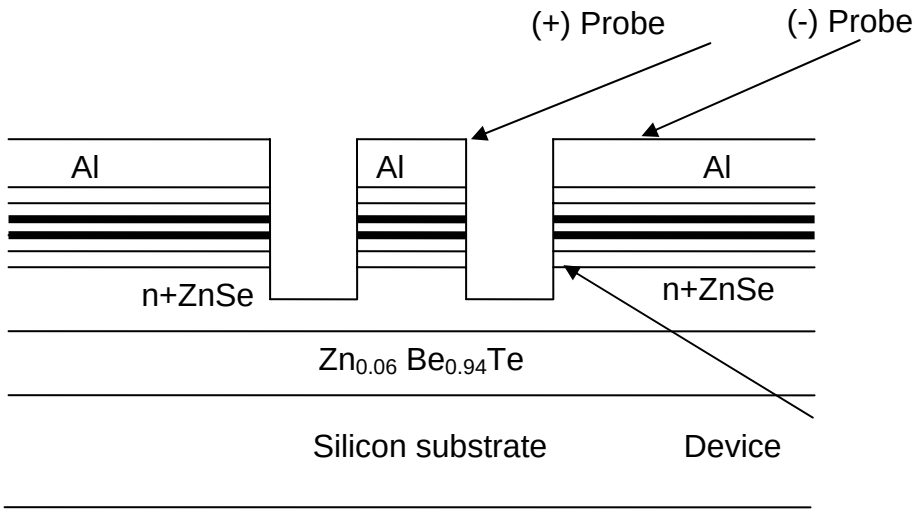


Fig 3.2 Measurement method

The instrument used for current voltage measurement is HP 4061A semiconductor parameter analyzer. The current-voltage characteristics were taken in the negative and the positive bias. The voltage steps are 30mV and the step delay time was 20ms.The measurements were taken with a round trip scan in which the voltage is wept from ‘0V’ to the positive mentioned voltage and from there back to ‘0V’ and from ‘0V’

to negative voltages and then back to '0V'.This was done in order to check for hysteresis and retracing of NDRs.

The resistance of the circuit was measured using a short circuit condition by putting both the probes next to each other on metal. The voltage was swept between positive and negative voltages and the resistance was measured to between 8 ohms to 10 ohms depending upon the pressure applied by the probes. The devices were found to be very highly resistive compared to this series resistance. The loading affect on these devices is not significant.

## 3.2 Experimental I-V characteristics

The ZnSe/BeTe RTDs exhibit multiple NDR regions. These multiple NDRs can be used for many multi-valued digital applications such as logic and memory. The experimental current-voltage (I-V) characteristics of samples Z 543, Z 563, Z 586, Z593, Z 594 and Z 599 are discussed below. The device sizes are 150um in diameter.

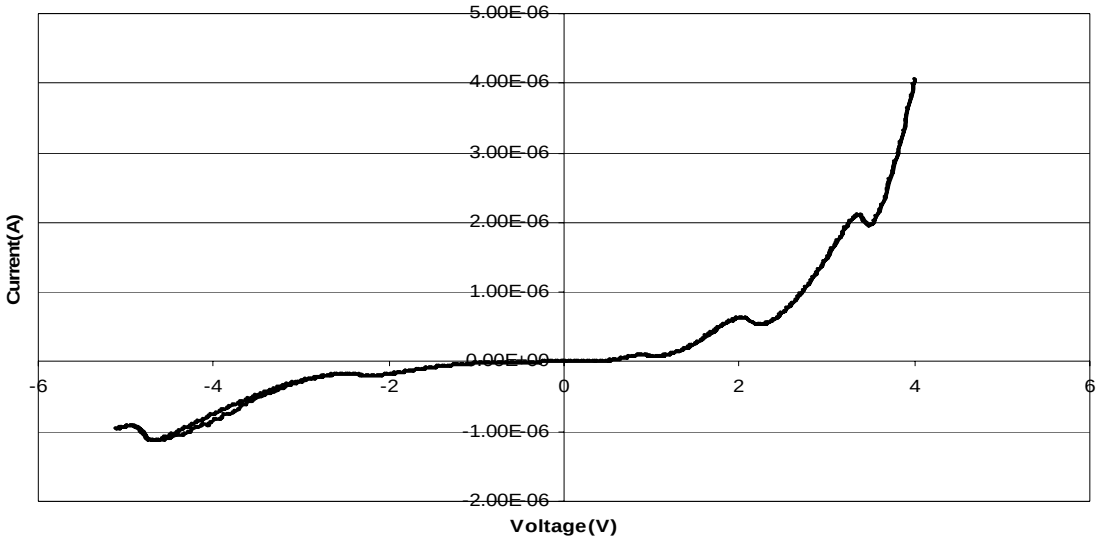


Fig 3.3 I-V characteristics of sample Z 543

The sample Z 543 was the first device in which NDR was observed. The device exhibited 3 NDRs on the positive bias and 2 NDRs on the negative bias The PVRs for the positive and negative bias NDRs are given in Table 3.1.The peak current densities as well as the peak voltages are listed represented by '$P_{CD}$' and '$P_V$' respectively.

Table 3.1 Sample Z 543 NDR parameters

| PVR | $P_{CD}$(A/cm$^2$) | $P_V$(volts) |
|---|---|---|
| 1.12 | 5.42E-04 | 0.9 |
| 1.21 | 3.66E-03 | 2.04 |
| 1.09 | 1.20E-02 | 3.39 |
| | | |
| 1.16 | 1.13E-03 | -2.16 |
| 1.23 | 6.42E-03 | -4.65 |

Sample Z 543 showed PVRs ranging from 1.09 to 1.23 with lowest and highest peak current densities being 0.542 mA/cm$^2$ and 12 mA/cm$^2$ respectively. The overall current density is in the milli-ampere range. There is a small hysteresis seen in the plot between -3V and -4.65V on the negative bias, this could be because of the charging of the device in the forward sweep. This hysteresis was seen only in a few devices and not all the devices which were tested, otherwise the round-trip sweep retraced very well on other parts of the curve.As it can be seen in the plot there is an asymmetry in NDRs as well as magnitude. The asymmetry in magnitude can be seen by taking positive and negative voltage biases of equal magnitude and looking into the current density at those points shown in Table 3.2. There is a higher current in the positive bias than for the negative bias. The devices were biased to higher voltage looking for more NDR regions for positive and negative biases, but seem to break down for biases more than 8V and -

8V.The cause for this asymmetry in NDRs and magnitude of current in I-V characteristics was suspected to come from the Aluminum-ZnSe contact which is investigated in the next section of this chapter.

Table 3.2 Magnitude asymmetry of sample Z 543

| Bias points(V) | Current density(A/cm$^2$) |
|---|---|
| 1 | 5.10E-04 |
| -1 | -1.32E-04 |
| 2 | 3.65E-03 |
| -2 | -1.02E-03 |
| 3 | 8.47E-03 |
| -3 | -1.53E-03 |
| 4 | 2.30E-02 |
| -4 | -4.34E-03 |

The I-V characteristics of sample Z 563 is shown in Fig 3.4.This sample showed NDR regions only in the positive bias and no NDRs on the negative bias.

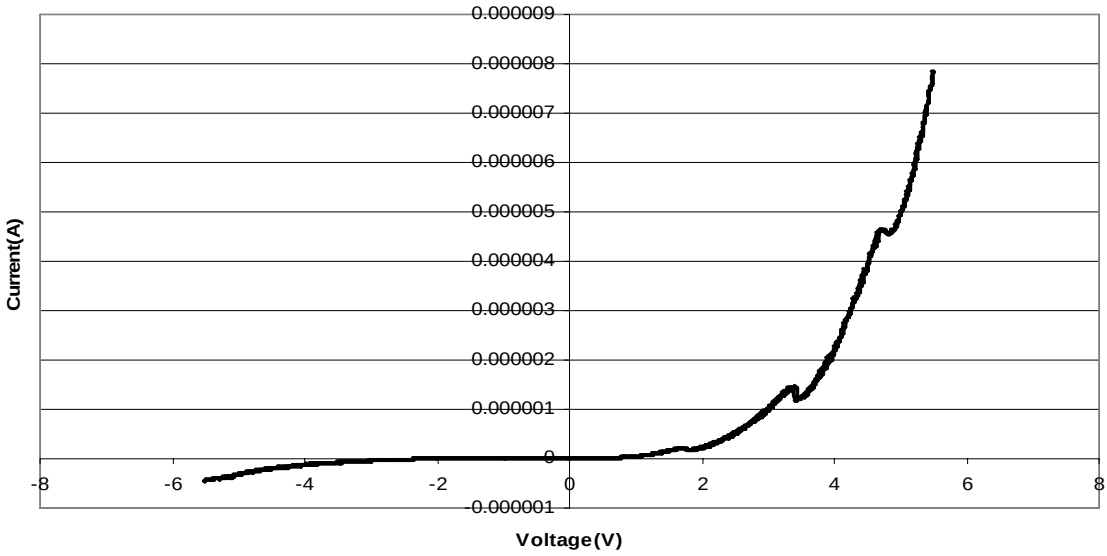


Fig 3.4 I-V characteristics of sample Z 563

There are 3 NDRs in the positive region whose PVRs, Peak current densities and peak voltage is listed in Table 3.3.Hysteresis in the forward and reverse sweeps were not observed. The PVRs range from 1.01 to 1.23 and peak current density in the positive bias region is comparable to the sample Z 543.The current density in the positive bias range is in milli-amperes. The current density in the negative bias were checked at bias points of -1V,-2V,-3V and -4V and were 7.50E-06 A/cm$^2$, 5.45E-05 A/cm$^2$ , 2.94E-04 A/cm$^2$ and 7.90E-04 A/cm$^2$ respectively. The difference between the positive and negative side is and magnitude asymmetry is given in Table 3.4.This sample is more asymmetric in magnitude than sample Z 543.

Table 3.3 Sample Z 563 NDR parameters

| PVR | $P_{CD}$(A/cm$^2$) | $P_V$(volts) |
|---|---|---|
| 1.19 | 1.17E-03 | 1.71 |
| 1.23 | 8.24E-03 | 3.42 |
| 1.01 | 2.63E-02 | 4.74 |

Table 3.4 Magnitude asymmetry of sample Z 563

| Bias points | Current density |
|---|---|
| 1 | 2.06E-04 |
| -1 | 7.50E-06 |
| 2 | 1.32E-03 |
| -2 | 5.45E-05 |
| 3 | 5.80E-03 |
| -3 | 2.94E-04 |
| 4 | 1.26E-02 |
| -4 | 7.90E-04 |

The next I-V characteristic is for sample Z 586 which is shown in Fig 3.5.This sample showed 3 NDRs in the positive bias and 2 NDR in the negative bias. There is an asymmetry in the number of NDRs and magnitude of current between the positive and the negative bias. The PVRs range between 1.01 and 1.09.The peak current densities are between 23.1 mA/cm$^2$ and 242 mA/cm$^2$.The current density has increased atleast 10 to 200 times compared to samples Z 543 and Z 563.

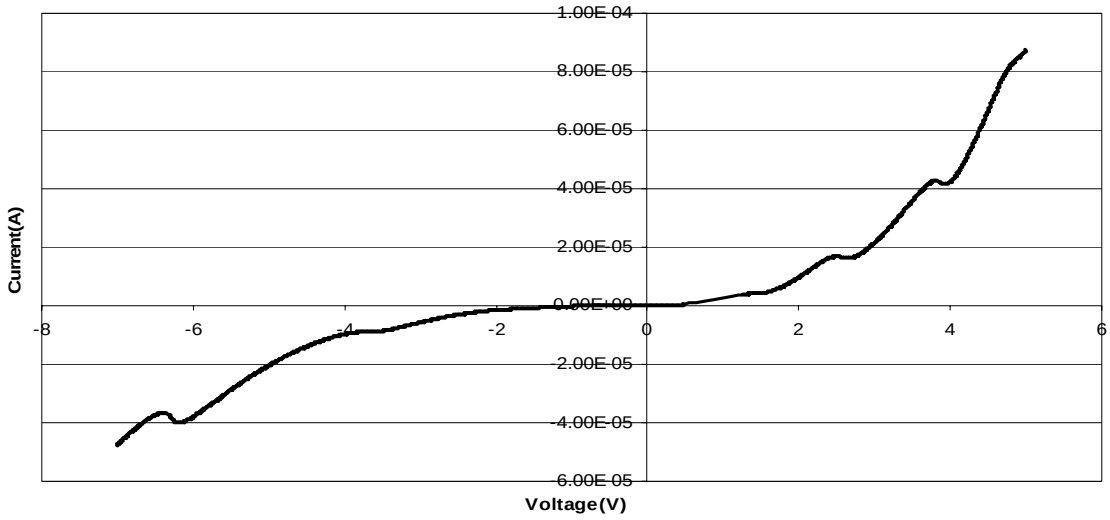


Fig 3.5 I-V characteristics of sample Z 586

There was no hysteresis observed in this sample. The NDR parameters are shown in Table 3.5 and the magnitude of asymmetries are shown in Table 3.6.There is also a reduction in asymmetry when compared to Z 563 in terms of magnitude of current.

Table 3.5 Sample Z 586 NDR parameters

| PVR | $P_{CD}$ (A/cm2) | $P_V$ (Volts) |
|---|---|---|
| 1.01 | 2.31E-02 | 1.41 |

Table 3.5 – *continued*

| | | |
|---|---|---|
| 1.04 | 9.55E-02 | 2.5 |
| 1.03 | 2.42E-01 | 3.8 |
| | | |
| 1.01 | 5.19E-02 | -3.66 |
| 1.09 | 2.28E-01 | -6.18 |

Table 3.6 Magnitude asymmetry of sample Z 586

| Bias points(V) | Current density(A/cm$^2$) |
|---|---|
| 1 | 9.60E-03 |
| -1 | -1.68E-03 |
| 2 | 5.40E-02 |
| -2 | -9.32E-03 |
| 3 | 1.11E-01 |
| -3 | -3.34E-02 |
| 4 | 2.40E-01 |
| -4 | -5.64E-02 |

Sample Z 586 was grown with half the thickness of emitter and collector doped layers keeping the other thicknesses such as undoped spacer, barriers and quantum well thickness. The change was a large increase in current densities and a small decrease in PVRs.

The next sample which is Z 593 was grown without the lightly doped ZnSe also the undoped ZnSe spacer was made smaller changing it from 100 Å to 20 Å.

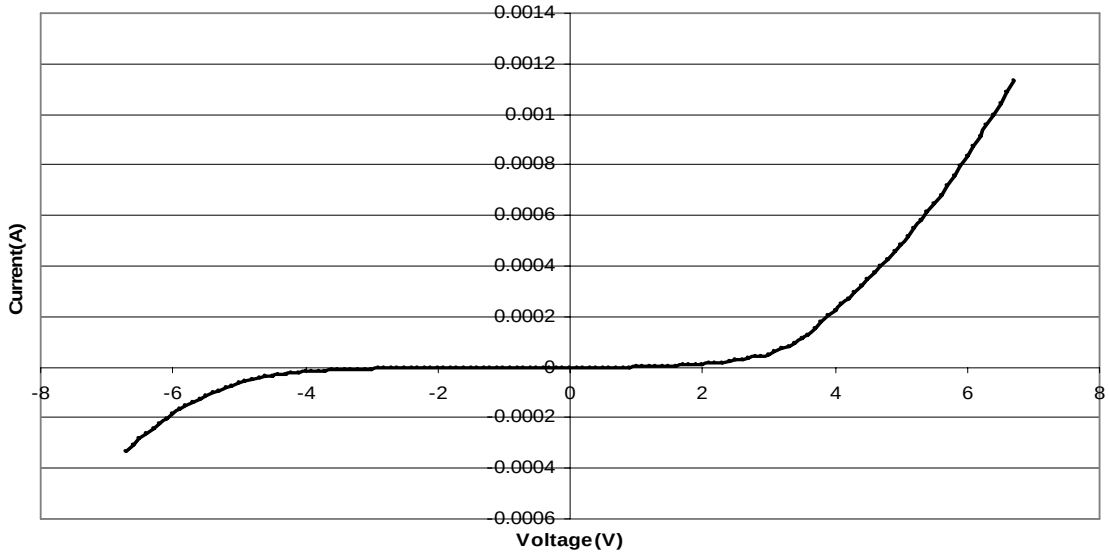


Fig 3.6 I-V characteristics of sample Z 593

The I-V characteristics of sample Z 593 are shown in Fig 3.6.There was no NDR observed in this sample at room temperature. The same kind of a magnitude asymmetry is observed in this sample. One of the reasons for asymmetric characteristics in ZnSe-BeTe RTDs could have been from asymmetric doping on either side of the quantum well in the emitter and collector. There could have been some dopant segregation in which the dopant profile changes resulting to be more near the surface and lesser away from the surface.Z593 had only the higher doped ZnSe on either side of the quantum well along with the 20 Å un-doped spacer and asymmetry in the I-V characteristics was still observed. The dopant profile and dopant gradient is present in the previous samples and hence NDR is observed at room temperature.

A triangular potential well is formed between the quantum well and the emitter because of having the undoped ZnSe spacer, lightly doped ZnSe and higher doped ZnSe

which constitute the dopant grading. The dopant grading in the emitter and collector play an important role in high performance RTDs.The removal of lower doped ZnSe and smaller spacer was to check the effect of triangular potential well on characteristics. Although no NDR was exhibited by this sample at room temperature it was understood that asymmetric doping did not contribute to asymmetry which is later shown in Chapter 4 in simulations also. It was also understood that the dopant grading is necessary for getting room temperature NDR.

Sample Z 594 was grown by removal of lower doped ZnSe and increasing the un-doped ZnSe spacer to 100 A. The I-V characteristics of sample Z 594 is shown in Fig 3.7.This sample did not show any NDR at room temperature. The asymmetric I-V characteristics are still observed.

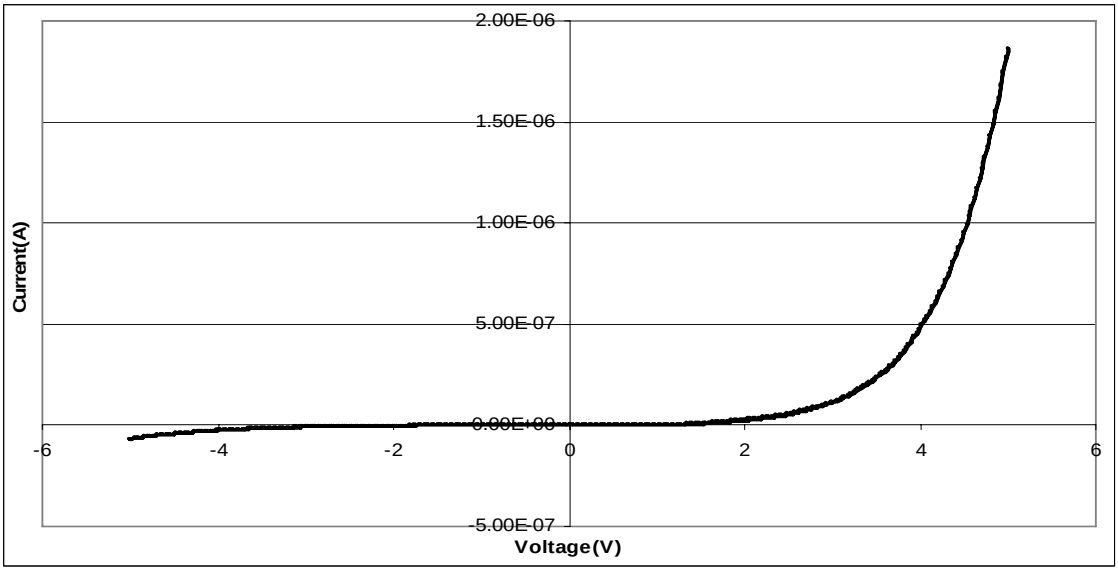


Fig 3.7 I-V characteristics of sample Z 594

The only difference between sample Z 593 and Z 594 is the un-doped ZnSe spacer which is 20 Å in Z 593 and 100 Å in Z 594.The current density of Z 593 is much higher than Z 594.The effect of reducing the spacer increases the current density. The change in width and depth of the triangular potential well can be brought about by increasing the thickness and doping gradient. It is known that having a lower doping near the well increases the PVR but decreases the current density. This is an additional parameter which can be used to get better characteristics.

The sample Z 599 was grown with identical parameters of Z 586 but the doping in the emitter and collector graded doping was increased. A plot of the Z 599 is shown in Fig 3.8.

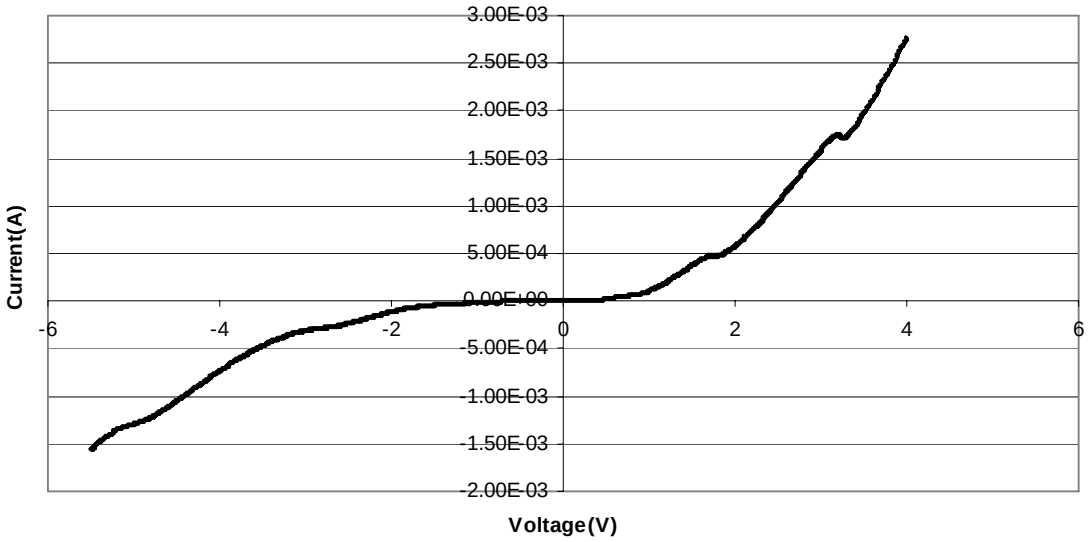


Fig 3.8 I-V characteristics of sample Z 599

The sample Z 599 showed 3 NDRs in the positive region and 1 NDR in the negative region whereas the Z 586 has 3 NDRs in the positive and 2 NDRs in the

negative. The second NDR in the negative of Z 599 as seen in the figure is very small at lower temperatures it will surely show NDR in these regions. Qualitatively comparing Z 586 and Z 599 it looks almost the same but smaller PVRs. There is a large increase in current density of Z 599 compared to Z 586 which is expected from higher doping. Z 586 the current for a 150um device is in microamperes and the current in Z 599 is in milliamperes for a 150 um device. The asymmetric nature of the current voltage characteristics is similar to Z 586.There was no hysteresis seen in the current-voltage characteristics of Z 599.The expected results for Z 599 was to reduce the temperature dependence of current-voltage characteristics compared to regular doping of Z 586.Another result was to increase the PVR but Z 586 has higher PVR than Z 599.Since the barriers are as small as 6 nm there could be a mismatch between the barriers which cause the NDR to decrease. There could be other defects and scattering causing the NDR to decrease which will be explained in Chapter 5 in detail. The current density at the peak voltage points and the PVRs are shown below for Z 586 and Z 599.

Table 3.7 Comparison of current density and NDR of Z 586 and Z 599

| | Z 586 | | Z 599 | |
|---|---|---|---|---|
| NDR | $P_{CD}$(A/cm$^2$) | PVR | $P_{CD}$(A/cm$^2$) | PVR |
| NDR1(+) | 2.31E-02 | 1.01 | 3.20E-01 | 1.01 |
| NDR2(+) | 9.55E-02 | 1.04 | 2.69 | 1.01 |
| NDR3(+) | 2.42E-01 | 1.03 | 9.94 | 1.02 |
| | | | | |
| NDR1(-) | 5.19E-02 | 1.01 | 1.61 | 1.01 |
| NDR2(-) | 2.28E-01 | 1.09 | 7.27 | none |

## 3.3 Ohmic contacts and rectifying effect

One of the reasons for having asymmetrical current-voltage characteristics in our ZnSe/BeTe RTDs was suspected to come from the contact between n-ZnSe and the in-situ aluminum deposited on top. It has been known that Al/n-ZnSe has a barrier of 0.54eV to 0.56eV [47]. It is in general very difficult to get ohmic contacts on ZnSe, because ZnSe gets oxidized almost instantaneously. There has been a lot of work done to get in-situ and ex-situ ohmic contacts on ZnSe [48]. It is easier to get ohmic contacts of highly doped samples which are very close to be metallic and hence a reduction in the schottky barrier. Some of the methods of annealing metal/semiconductor contacts like Al/n-ZnSe contacts basically cause the 'Al' to dope the n-ZnSe semiconductor interface to a high level and reduce the barrier in order to get ohmic contacts. Indium has been used to get good ohmic contacts on n-ZnSe [49],also Ti/Pt/Au on ZnSe have been used to get ohmic contacts [50].The most interesting and practical results were obtained by evaporating indium tin oxide(ITO) on ZnSe whether oxidized or clean and annealing it to get good ohmic contacts [48].For perfect top to bottom measurement of current-voltage characteristics of ZnSe-BeTe RTDs, the ZnSe beside the devices needs to be etched all the way down to bottom doped layers and an ohmic contact needs to be established on the ZnSe surface to conduct to the bottom of the device. This requires ex-situ methods of making ohmic contacts on n-ZnSe. Our method was to use in-situ deposited aluminum avoiding the surface of ZnSe to be exposed and get oxidized. The doping of n-ZnSe is 5e18 $cm^{-3}$.

We suspected our device characteristics to be over written by the schottky effect because of the Al/n-ZnSe barrier. The following experiment was done in order to check whether our Al/n-ZnSe contacts were ohmic or schottky. Following the steps in Chapter 2, section 2.2 of processing upto the fourth step of etching. After the metal was etched away, very small etch steps into the n-ZnSe were done. In each step the current voltage characteristics were checked for and showed ohmic contacts when it was etched between 0.1um to 0.46um. The theoretical target thickness of n-ZnSe in MBE was 0.5um.The range of resistances started with 35 ohms and went upto 150 ohms for 0.46um. The method of measurement is same as in Section 3.1.The current will travel from the positive electrode on the small contact through the metal into the n-ZnSe and through the n-ZnSe back into the metal on the negative probe on the bigger contact. This shows that the Al/n-ZnSe contact is ohmic. Two plots are shown which are for 0.1um and 0.46um, trend lines were fitted to the data and the resistance showed 34.7 ohms and 133.5 ohms respectively. It was confirmed that the Al/n-ZnSe contact was an ohmic contact. The plots are shown in Fig 3.9 and Fig 3.10.

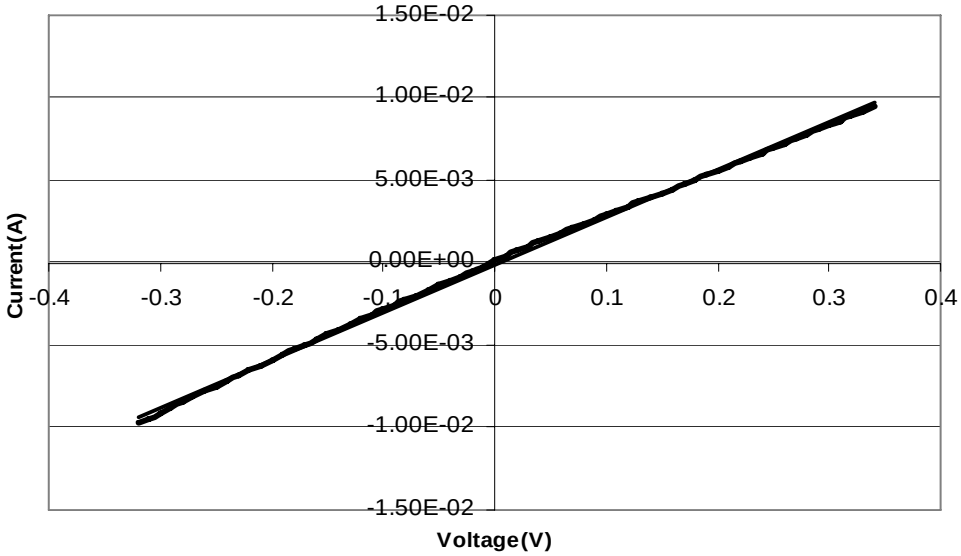


Fig 3.9 Ohmic contact in Al/n-ZnSe after etching of 0.1um of n-ZnSe

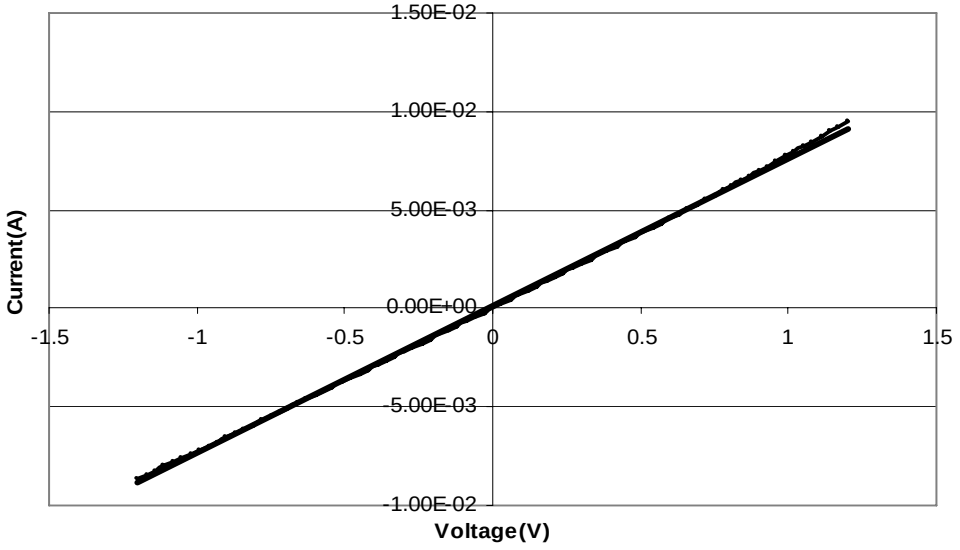


Fig 3.10 Ohmic contact in Al/n-ZnSe after etching of 0.46um of n-ZnSe

Another interesting characteristic was seen during the etching experiments. After etching some more and after we think we crossed the double barrier region we saw a rectifying characteristic shown in Fig 3.11. The characteristic shown was

observed before etching into the bottom doped grading of the RTD. Since the quantum well region is only 0.016um this thickness cannot be controlled in the etch and cannot be monitored using theoretical thicknesses. In order to see NDR the device was etched further into the bottom doped layers and NDR was seen and this was done on sample Z 586 which is shown in Fig 3.5 of the previous section.

We suspected that the schottky characteristic could have come when the current goes from the doped ZnSe regions and undoped quantum well regions but the opposite effect would have been present when the devices were etched all the way to the bottom end and measured. This would generate symmetrical characteristics.

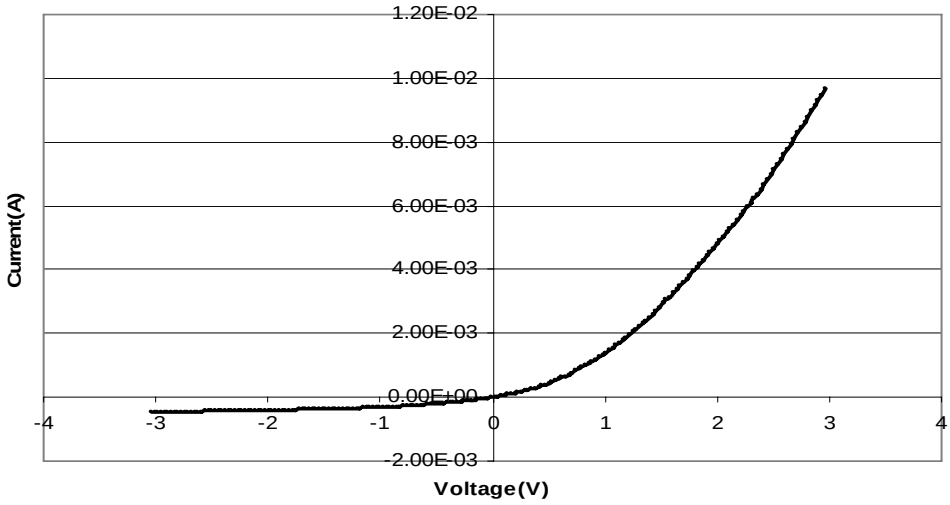


Fig 3.11 Rectifying effect seen during the fabrication of RTD

Therefore in-situ deposited aluminum showed good ohmic contacts and the Al/n-ZnSe contact was ruled out as a cause of asymmetry in current-voltage characteristics. Simulations in NEMO are used to explain this effect in the Chapter 4

## 3.4 Low temperature measurements

Quantum electronic devices behave differently at temperatures lower than room temperature of 300K.The characteristics of RTD obtained at lower temperature is a result of only quantum mechanical phenomena and other transport happening through the device excluding thermal current. In ZnSe-BeTe RTDs the I-V characteristics is a result of resonant electron tunneling in the conduction band, indirect band transitions because of the type-II band alignment and carriers which are thermally excited over the barriers, all these factors contribute to the overall current. At lower temperatures the current contributed by thermal excitation over the barriers is eliminated

ARS cryostat is used to get low temperatures down to 3.2K.The system is a closed cycle cryogenic refrigerator based on the Gifford-McMahon refrigeration cycle. The refrigerant gas used is 99.999% helium. The whole system consists of a expander, water cooled helium compressor and a coolpac closed loop cooling system shown in Fig 3.12.A mechanical pump is used to remove all air in the expander down to $10^{-3}$ Torr. The expander consists of two stages in which the second stage has a sample holder under which the helium gas is sent through very small lines. The expanding of helium allows for the cooling of the sample. The low pressure helium is sent back to the compressor. The helium is again pressurized and again allowed to expand allowing it cool further, this happens in a cycle.

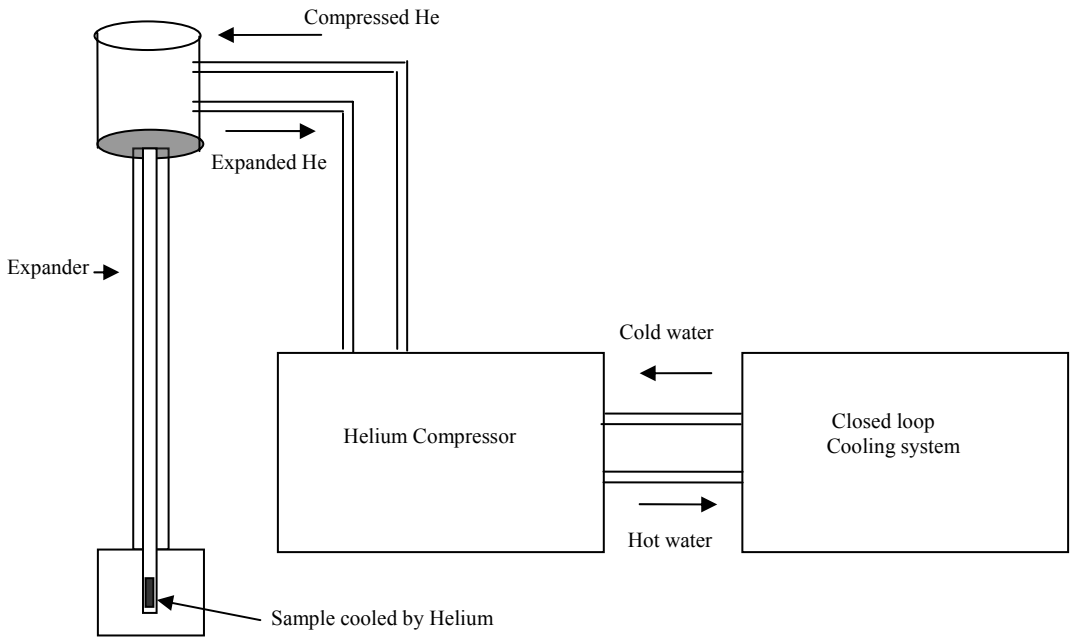


Fig 3.12 Cryostat and cooling system

There is some heat induced during compression and this heat is removed by the closed loop cooling system. The closed loop water-air cooling system sends the hot water from the compressor cooling coil in which heat is exchanged by forcing air over the coils using an electric fan. The cold water re-enter the compressor and the cycle continues. There is a temperature sensor located in the second stage beside the sample holder indicating the temperature to which the sample is cooled. The measurement of I-V characteristics was done in a similar way as shown in Section 3.1.

The sample Z 586 was measured at a temperature of 3.2K using the cryostat and the I-V characteristics are shown in Fig 3.13.

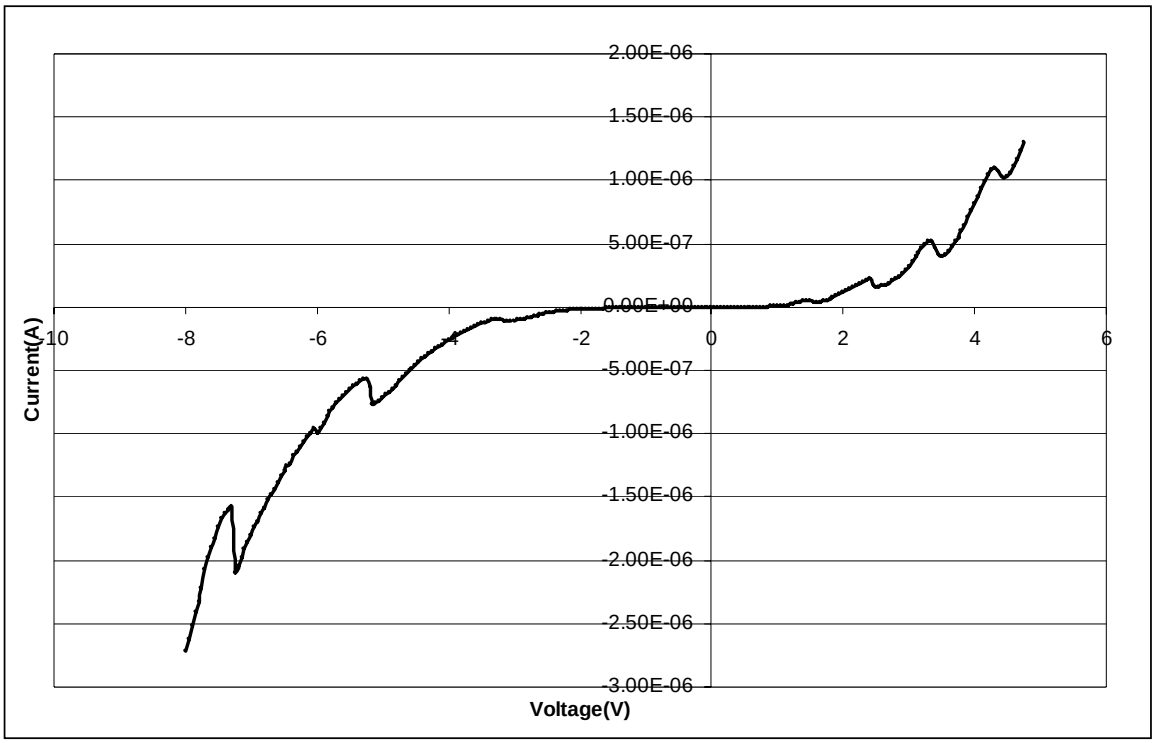


Fig 3.13 I-V characteristics of Z 586 at 3.2K

The measurements showed an additional NDR region on positive as well as the negative bias region. The sample Z 586 showed 3 NDRs on positive and 2 NDRs on the negative side at 300K and 4 NDRs on the positive side and 3 NDRs on negative side at 3.2K.There is also an increase in PVR which is expected at low temperatures the increase in PVR for this sample is shown in Table 3.8.The NDR regions are counted from '0V' to a positive or negative voltages. The sign in the brackets indicate a positive bias or negative bias NDR. There is a feature at '-6V' but it could not be reproduced hence was not considered to be a NDR. The device even at low temperatures seems to be asymmetric in nature.

Table 3.8 PVR comparison at 300K and 3.2K

| Regions | PVR (300K) | PVR (3.2K) |
|---|---|---|
| NDR1(+) | 1.01 | 1.3 |
| NDR2(+) | 1.04 | 1.42 |
| NDR3(+) | 1.03 | 1.31 |
| NDR4(+) | none | 1.07 |
| | | |
| NDR1(-) | 1.01 | 1.15 |
| NDR2(-) | 1.09 | 1.33 |
| NDR3(-) | none | 1.33 |

At room temperatures the peak current and valley current are influenced by current caused by thermal carriers. When the device is biased in the valley region theoretically the resonant states are out of phase and current should be zero but current is influenced by thermal carriers, scattering and there is a small probability of electron tunneling even though the states are not coinciding. At low temperatures the thermal carrier current contributing to the valley current is not there and hence the valley current decreases causing PVR to increase. The increase in PVR at low temperatures depends upon the percentage of thermal carrier current contributing to valley current. Additional NDR regions which can only be seen at low temperature are a result of thermal carrier current influencing the valley current at room temperatures. Another inference drawn from this experiment is that the current density of the device decreased with temperature. At 3.2K the current density decreased by 10 $A/cm^2$ compared to 300K.This dependence of current density on temperature is termed thermally assisted tunneling in which the Fermi-level in the emitter and collector are spaced much lower than the first resonant state in the quantum well. The carriers are thermally excited from

the Fermi-level to a resonant point and scattered into the resonant state. This will be discussed in detail later with the help of simulations in Chapter 5.

# CHAPTER 4

# NEMO SIMULATIONS

In this chapter the tight binding theory and non-equilibrium Green's functions used in NEMO is explained. The building of the material parameters set used for NEMO simulations of ZnSe-BeTe RTD structure is shown. NEMO simulations of the structure with different thicknesses of barriers and wells are simulated. NEMO is used to explain the asymmetric current-voltage characteristics seen experimentally and the effect of temperature change and increase and decrease of doping in the emitter and collector on the current-voltage characteristics have been simulated.

## 4.1 Parameters used in NEMO simulations

As the critical dimensions of semiconductors in devices reach the nanometer scale, there is a requirement to model these devices with atomic resolution. Tight binding models are known to retain the quantum mechanical basis with reduced computation and good accuracy compared to other models. The tight binding approach incorporates the atomistic representation of semiconductors with a localized basis set. Tight binding methods lie between the accurate and expensive *ab initio* methods and the fast but lesser accurate empirical methods. Tight binding methods of representation of band structures are far more superior than envelope function or k.p methods because of proper representation of the full band structure. The full band structure representation

using tight binding models have non-parabolic bands when compared to other parabolic band structure models have lower second resonant state and hence lower second turn-on voltage in RTDs. Also non-parabolic models cause a lesser attenuation of carriers and hence present more current density compared to single band parabolic models. Another advantage of tight binding models is that the accurate modeling of hetero-interfaces which are present in quantum confined hetero structures.

Tight binding models evolved from linear combination of atomic orbital (LCAO) which is based on the localized character of the valence electrons of the semiconductor [51].Hamiltonian operator represents the total energy of the system in quantum mechanics. The Schrödinger equation is the Eigen value function for the Hamiltonian in which the Eigen values are the energy levels of the system. The interest of tight binding models is the transferability of the Hamiltonian matrix from bulk semiconductors to low dimensional systems like quantum wells and quantum dots and fitting of the band structure to experimental data to obtain the electronics properties of semiconductors [52]. The use of the tight binding theory in the application of forming the band structures relies on the construction of the Hamiltonian matrix.

The electron is represented by the wave function which satisfies the Schrödinger equation. The forces acting on the electron from the atoms in a periodic lattice is given by the periodic potential of the lattice. The atomic orbitals are transformed into Bloch type orbitals because of the crystal symmetry, finally this is converted into Bloch sums. The Eigen functions of Schrödinger equation are written as linear combinations of block sums. The mathematical equations for the above are shown in [53].Suppose the matrix

is represented by AxB rows and columns, where A is the number of atoms per unit cell and B is the number of orbitals per atom. Depending upon the crystal structure of the semiconductor and the orbitals needed to be included the size of the matrix varies. Suppose if the model requires to use s, px, py, pz or $sp^3$ orbitals there will be four columns in the matrix. NEMO is capable of representating $sp^3$ , $sp^3s^*$, and $sp^3d$ models for obtaining band structures. The more the number of orbitals used the more accurate the band structure is represented. Of course with the increase in orbital inclusion the parameter set becomes larger and calculations for transport become more intensive. In this work the $sp^3s^*$ model is used in which $s^*$ is the excited state of the orbital for an isolated atom. The $sp^3s^*$ model was developed because the $sp^3$ model had too much dispersion and could not reproduce the minima at the 'X' point in the conduction band of indirect semiconductors, whereas the $sp^3s^*$ model drives the lowest conduction band to a lower energy. The basis of this model is given by Vogl et al [12].Further modification to include the excited 'd' orbital is given by Jancu et al [ 54].

The reason for using $sp^3s^*$ tight binding parameters in our simulations is that it has 15 parameters which represents the band structures a particular material, whereas $sp^3d^5$ tight binding parameters uses 37 parameters to represent a material. The $sp^3s^*$ tight binding parameters are also available for materials like ZnSe, BeTe, BeSe and ZnTe which are used in ZnSe-BeTe RTD simulations. The $sp^3s^*$ Hamiltonian consists of five orbitals for each atom the $sp^3$ plus the excited orbital s* .The total matrix is a 10x10 matrix. There are a total of 15 $sp^3s^*$ tight binding parameters in which 6 are orbital energies E(s,a), E(s,c),E(p,a),E(p,c),E(s*,a) and E(s*,c).It includes 7 tight

binding transfer matrix elements V(s,s),V(pa,sc),V(sa,pc)V(s*a,pc),V(pa,s*c),V(x,x) and V(x,y).The 'a' stands for anion and 'c' stands for cation. These are all based on the nearest neighbor interactions. The two other parameters are for the spin orbit coupling represented as $\Delta a$ and $\Delta c$. All the 15 parameters mentioned above are related to the band edges of the material at 'Γ','X' and 'L' in a non-trivial manner explained in [53].

The use of $sp^3s^*$ tight binding parameters for simulations needs an additional element which makes it into empirical tight binding parameters. Usually for simulations to be more realistic and model the experimental curves the $sp^3s^*$ tight binding parameters are modified to reproduce certain experimentally available band edge energies, effective masses and band-offsets. For transport simulations of RTDs the proper representation of relative band edges and curvature of the conduction and valence bands is important. The building of $sp^3s^*$ parameters can be from ab-initio methods and later modified to empirical $sp^3s^*$ tight binding parameters.

One of the best methods used for parameter fitting to get empirical $sp^3s^*$ tight binding parameters for simulations is genetic algorithms [55].In a genetic algorithms suppose we have a set of parameters in which we need to modify it in order to fit a certain experimental value, this requires a fitness function to tell us how close we are getting to the experimental value or whether we are getting far from the experimental value. Then a range must be set for the parameters, in which they can be varied or not varied, this is usually done using a software program in which the set of parameters are varied and the fitness function is checked for and if it is getting closer then it keeps the set of changed values, but if it is getting farther it goes back and again changes it. The

parameters evolve to get a good fitting to experimental values sacrificing other parameters which are not important. After some iterations some random values within the specified range must be given in order for the program not to get stuck in the local minima. Genetic algorithms can be applied to the actual simulations of current-voltage characteristics of RTD compared to experimental current voltage characteristics such that the layer thicknesses and the doping are changed and the difference between curves are used as a fitness function. This requires a genetic algorithm software to be interfaced with the NEMO program completely parallel getting outputs and analyzing and changing inputs and giving it back to NEMO.A genetic algorithm software package called PGAPACK is used at NASA's JPL laboratories for simulations. Another more important use of genetic algorithms in modeling of hetero structures is the application to get empirical tight binding parameters. Empirical tight binding parameters for simulations have been calculated for various III-V materials by Klimeck et al [56] and for Si [57].Since the ZnSe-BeTe RTD is relatively new there are very few empirical tight binding parameters available in literature for this structure. This work is the first simulation of ZnSe-BeTe RTD using NEMO. This is more complex since we are dealing with 15 parameters and they have be fitted to experimental values. Genetic algorithms when applied to tight binding parameters have been used to fit experimental band offsets, band edges and effective masses, these are the important values required for RTD transport simulations. The $sp^3s^*$ model represent 10 valence and conduction bands of a material sometimes the accuracy of only the lowest conduction band and the highest three valence bands are fitted sacrificing the other bands since most of the

transport which affect the characteristics happen here. All that has been discussed above is related to the building of electronic band structure of semiconductors and how to get better results in modeling of experimental characteristics.

The success of NEMO as a quantum device simulator has been the combination of $sp^3s^*$ tight binding parameters to define the band structure and using non-equilibrium Green functions (NEGF) formalism for simulating current voltage characteristics [58].The central device region which consists of the double barrier and the quantum well in the RTD is where the NEGF is applied. In a quantum device simulation a transport equation is self-consistently solved with Poisson's equations. The transport equation calculates the electron density n(r) or the current (I) and the Poisson's equations are used to calculate the effective potential U(r) felt by the electrons. The n(r) and U(r) are iteratively solved till they converge [16, 59].The non-equilibrium Green's functions are defined as expectation values of single particle creators and annihilation operators and they describe the state and time evolution of a system. The Green's functions are obtained by solving a set of Dyson's equations which is integral form of Schrödinger equation. $G^<$ represents the distribution of electrons and $G^>$ represents the distribution of holes. Using the Hamiltonian for a particular for a particular device the transmission coefficients are calculated and from there the tunneling formula. The Hamiltonian of system excluding the scattering effects is shown in equation 16.

$$H_0 = H_0{}^D + H_0{}^L + H_0{}^R + H_0{}^{LD} + H_0{}^{RD} \text{ -------} (16)$$

where $H_0{}^{D}$ is the Hamiltonian of the double barrier quantum well the central device of RTD, followed by the Hamiltonians for the left and right contact and the coupling of the left and right contact to the device. The transmission coefficients for the RTD are calculated and this is shown by Lake et al [60].Using the Fisher-lee formula [61] for transformation to find current density. The electron density and current is calculated using the transformation and also the tunneling formula by Lake et al [18].The current density formula represents the current flowing through the emitter quasi-bound states as well as the current through the central device. The tunneling formula in a simple form for the NEMO simulator is shown in equation 17 [62].

$$J = \frac{2e}{\hbar A}\sum_{K}\int \frac{dE}{2\pi} * T(E.k) * (f_L - f_R) \text{ ----------} (17)$$

where T (E,k) is the transmission probability, $f_L$ and $f_R$ are the Fermi factors in the left and right contacts, 'A' is the cross-sectional area and 'e' is the electron's charge.

### 4.1.1 Tight binding parameters for ZnSe, BeTe, BeSe and ZnTe

NEMO has a material package in which material parameters according to the model used can be stored. New materials can be added and simulated provided the required parameters are available. The model used for our simulations is a 10-band $sp^3s^*$ model including split-off bands. The $sp^3s^*$ tight binding parameters have been taken from literature which are either empirical tight binding parameters or parameters in which calculations were done using *ab-initio* methods.

Various parameters sets were inputted into NEMO and primarily checked for band gaps of the materials and band edges for ZnSe and BeTe since they are the well and barrier materials. The band gap of ZnSe is 2.8eV and in direct band gap of BeTe is 4.1eV and the conduction band offset 2.3eV. The $sp^3s^*$ parameter sets for ZnSe and BeTe [63, 64, 65] were inputted in NEMO such that it was closest to the above mentioned band-gap and band-offset. The $sp^3s^*$ tight binding parameters used for ZnSe and BeTe are found in [66].Since BeSe and ZnTe are the interface materials which were included in the simulations their parameters and band-offsets were taken from [67, 68, 69].The $sp^3s^*$ tight binding parameters for ZnSe, BeTe, BeSe and ZnTe are shown in Table 4.1, Table 4.2, Table 4.3 and Table 4.4 respectively.

NEMO has the capability to generate band structures of materials from $sp^3s^*$ parameters. The generated band structure in NEMO is shown below the parameters of materials in the table. The parameters generate 10 bands but only 4 bands are shown in the diagrams below.

Table 4.1 $sp^3s^*$ parameters for ZnSe

| Parameters | ZnSe |
|---|---|
| E(s,a) | -10.19 |
| E(s,c) | 0.76 |
| E(p,a) | 0.06 |
| E(p,c) | 7.22 |
| E(s*,a) | 10 |
| E(s*,c) | 12 |
| V(s,s) | -5.17 |
| V(pa,sc) | 6.62 |
| V(sa,pc) | 5.41 |
| V(s*a,pc) | 5.63 |
| V(pa,s*c) | 5.75 |
| V(x,x) | 1.22 |

Table 4.1 - *continued*

| | |
|---|---|
| V(x,y) | 5.48 |
| $\Delta a$ | 0.43 |
| $\Delta c$ | 0.038 |

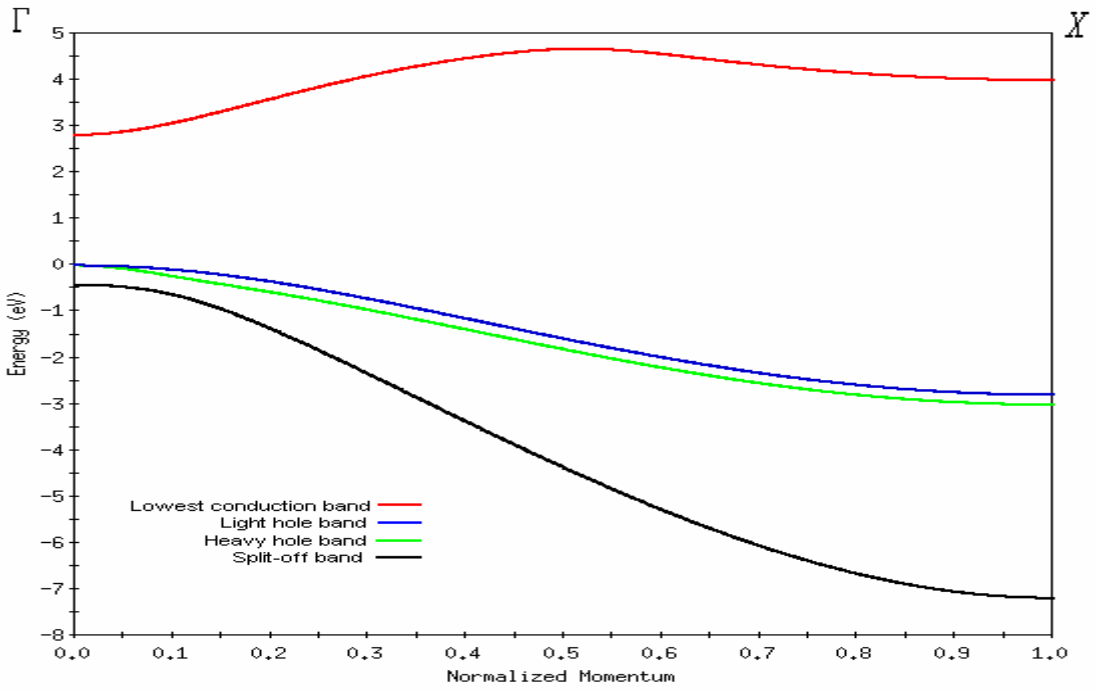


Fig 4.1 Band structure of ZnSe in NEMO

The lowest conduction band, light hole band , heavy hole band and the split-off band of ZnSe is shown in Fig 4.1

Table 4.2 $sp^3s^*$ parameters for BeTe

| Parameters | BeTe |
|---|---|
| E(s,a) | -9.307 |
| E(s,c) | 2.64 |
| E(p,a) | 1.18 |
| E(p,c) | 4.56 |
| E(s*,a) | 8.6 |
| E(s*,c) | 9.66 |
| V(s,s) | -6 |

Table 4.2 - *continued*

| | |
|---|---|
| V(pa,sc) | 7.5 |
| V(sa,pc) | -1 |
| V(s*a,pc) | 2.8 |
| V(pa,s*c) | 5.5 |
| V(x,x) | 1.96 |
| V(x,y) | 5.5 |
| $\Delta a$ | 1.1 |
| $\Delta c$ | 0.26 |

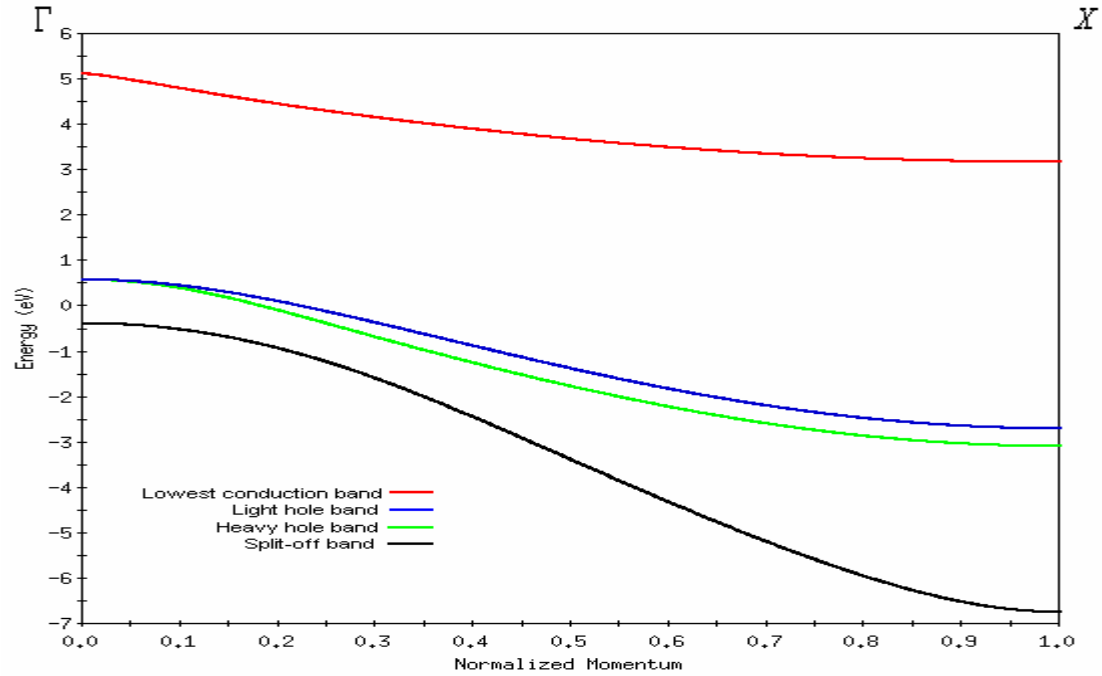


Fig 4.2 Band structure of BeTe in NEMO

The lowest conduction band, light hole band, heavy hole band and the split-off band of BeTe is shown in Fig 4.2

Table 4.3 $sp^3s^*$ parameters for BeSe

| Parameters | BeSe |
|---|---|
| E(s,a) | -20.953 |
| E(s,c) | 5.56003 |
| E(p,a) | 0.30003 |
| E(p,c) | 5.02603 |
| E(s*,a) | 24.433 |

Table 4.3 – *continued*

| | |
|---|---|
| E(s*,c) | 21.656 |
| V(s,s) | -8.195 |
| V(pa,sc) | 5.633 |
| V(sa,pc) | 4.89 |
| V(s*a,pc) | 7.462 |
| V(pa,s*c) | 4.572 |
| V(x,x) | 1.531 |
| V(x,y) | 6.324 |
| Δ*a* | 0.499 |
| Δ*c* | 0 |

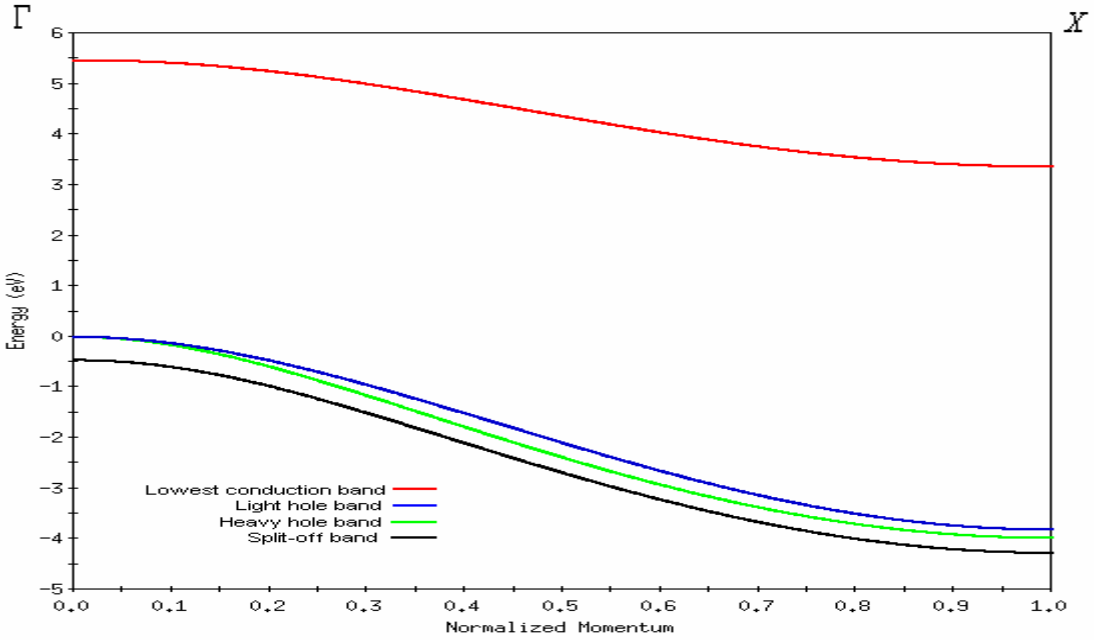


Fig 4.3 Band structure of BeSe in NEMO

The lowest conduction band, light hole band, heavy hole band and the split-off band of BeSe is shown in Fig 4.3

Table 4.4 $sp^3s^*$ parameters for ZnTe

| Parameters | ZnTe |
|---|---|
| E(s,a) | -7.0787 |
| E(s,c) | 1.73315 |
| E(p,a) | 0.85399 |
| E(p,c) | 6.62408 |

Table 4.4 - *continued*

| | |
|---|---|
| E(s*,a) | 7 |
| E(s*,c) | 8.5 |
| V(s,s) | -4.44786 |
| V(pa,sc) | 5.74609 |
| V(sa,pc) | 1.5482 |
| V(s*a,pc) | 3.1615 |
| V(pa,s*c) | 0.25598 |
| V(x,x) | 1.05466 |
| V(x,y) | 5.00065 |
| Δ*a* | 0.33241 |
| Δ*c* | 0.01952 |

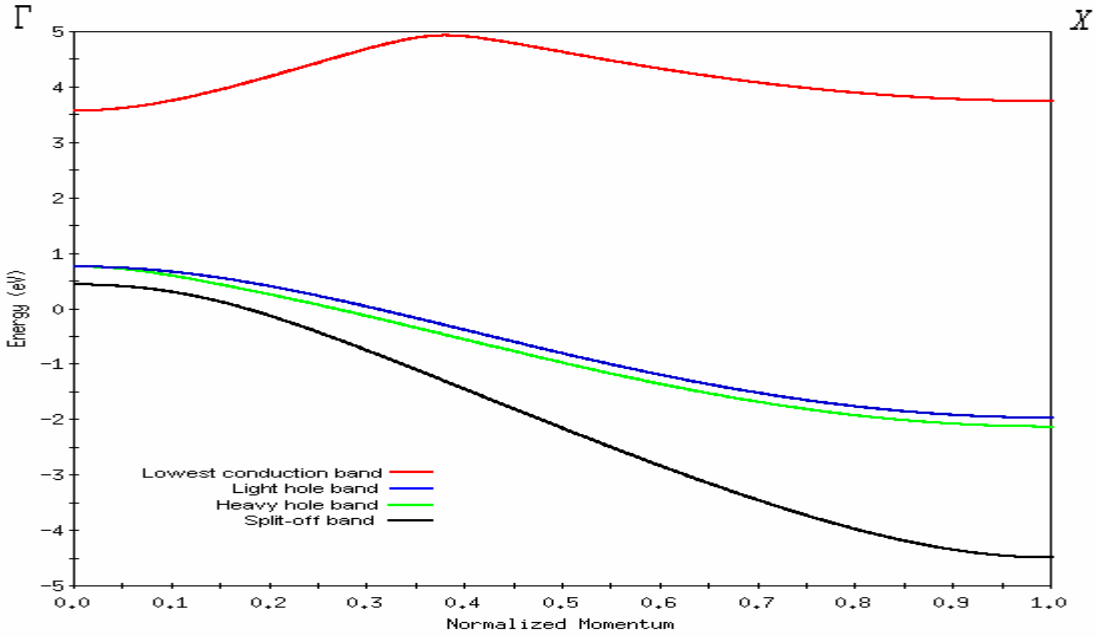


Fig 4.4 Band structure of ZnTe in NEMO

The lowest conduction band, light hole band, heavy hole band and the split-off band of ZnTe is shown in Fig 4.4.The band gaps of the materials were adjusted by changing the first four $sp^3s^*$ tight binding parameters E(s,a),E(s,c),E(p,a),E(p,c).The band gaps were adjusted at the Γ point for ZnSe and BeTe to be 2.8eV and 4.1eV direct band gap and for BeSe and ZnTe to be 5.5eV and 2.4eV.In the initial simulations only

the ZnSe-BeTe RTD system was used such that the band-gaps were maintained and the conduction band offset of 2.3eV and a valence band offset of 0.9eV was also maintained as close as possible by changing the band edges.

## 4.2 ZnSe-BeTe RTD simulations

NEMO mainly consists of two functionalities the first is resonance finding and the second the finding the current voltage characteristics. The process in which NEMO calculates the current-voltage characteristics is that first it calculates the resonances pertaining to the particular d.c. bias and then calculates the transmission coefficient and then the current density is plotted against voltages.

The resonance finding has different options in which the resonance finding region can be specified to be within the active region or outside, the resonances which can be eliminated depending upon the width and different potential models.

Apart from getting the current-voltage characteristics of the RTD the other output options along with it are transmission probability, total charge density, electron density, doping profile and resonance width as a function of bias.

The band structure initially simulated is shown in Fig 4.5 which has ZnSe and BeTe band gaps of 2.8eV and 4.1eV and ZnSe/BeTe conduction band offset of 2.3eV.The resonances are also shown E1=0.1464 and E2=0.245.

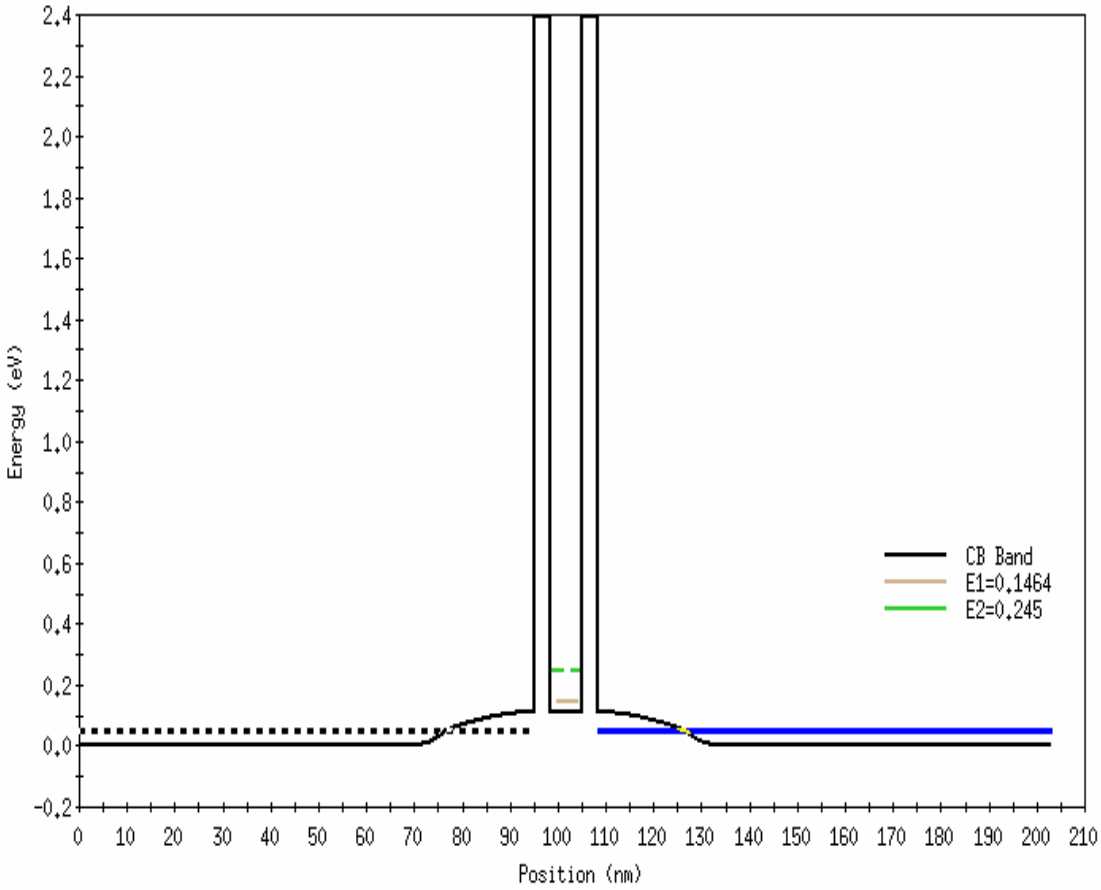


Fig 4.5 Initial band profile of ZnSe-BeTe RTD and resonances

The ZnSe-BeTe RTD was initially simulated using 4-band model in which the conduction band edges and the valence band edges needs to be specified. The potential model used was Thomas-Fermi model and the transverse integration used was analytical. The thickness and doping of emitter, collector and active region were taken from the target MBE values. The details of the structure simulated are given in Table

4.5.The BeTe barrier thickness is 5nm or 18ml and the ZnSe well is 6nm or 22ml are the experimental target thicknesses.

Table 4.5 Structure of ZnSe-BeTe RTD simulated in NEMO

| Material | Thickness (nm) | Doping n-type ($cm^{-3}$) |
|---|---|---|
| n+ZnSe | 500 | 5e+18 |
| n-ZnSe | 150 | 5e+17 |
| ZnSe | 10 | - |
| BeTe | 5 | - |
| ZnSe | 6 | - |
| BeTe | 5 | - |
| ZnSe | 10 | - |
| n-ZnSe | 150 | 5e+17 |
| n+ZnSe | 500 | 5e+18 |

### 4.2.1 Four-band simulations

For the I-V simulations using 4-band model also called the Cle_he_Vhh_lh model in which the four bands, two conduction bands and two valence bands. Different thickness of barriers and wells were tried and the I-V characteristics were seen to whether they qualitatively follow the experimental curves. The simulations which were found to be close to experimental curves were the BeTe barrier thickness of 16ml and ZnSe well thickness of 29ml.The simulations are shown below for different thickness. The representation used for simulations will be ‘Xb_Yw_Xb ‘ , the ‘X’ represents the barriers and the ‘Y’ represents the well. For example 17b_34w_17b represents 17ml barrier on either side of a 34 ml well. The I-V simulation of 12b_29w_12b is shown in Fig 4.6.

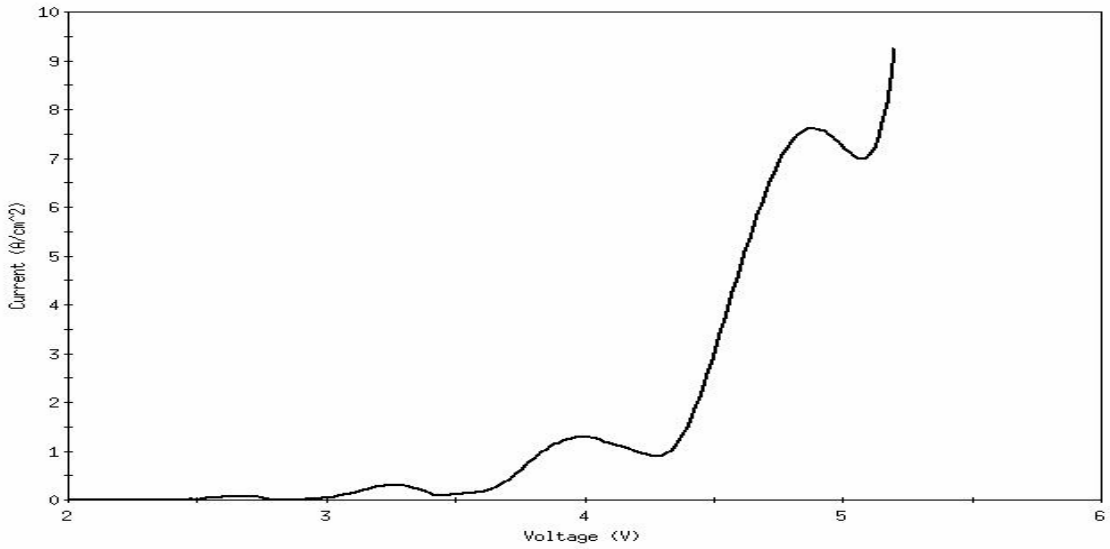


Fig 4.6 Four-band simulations of 12ml BeTe and 29ml ZnSe.

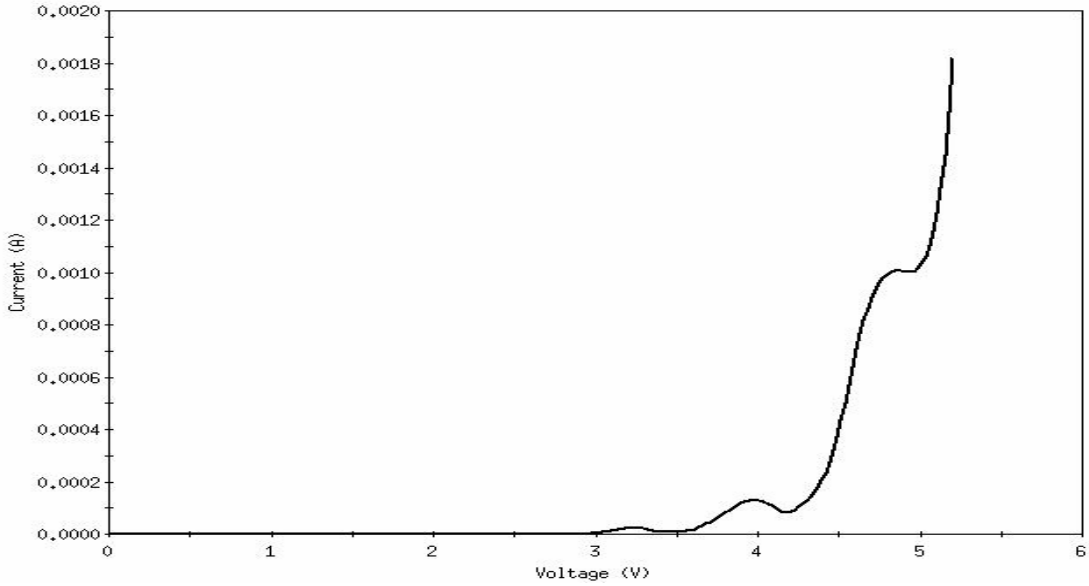


Fig 4.7 Four-band simulations of 14ml BeTe and 29ml ZnSe

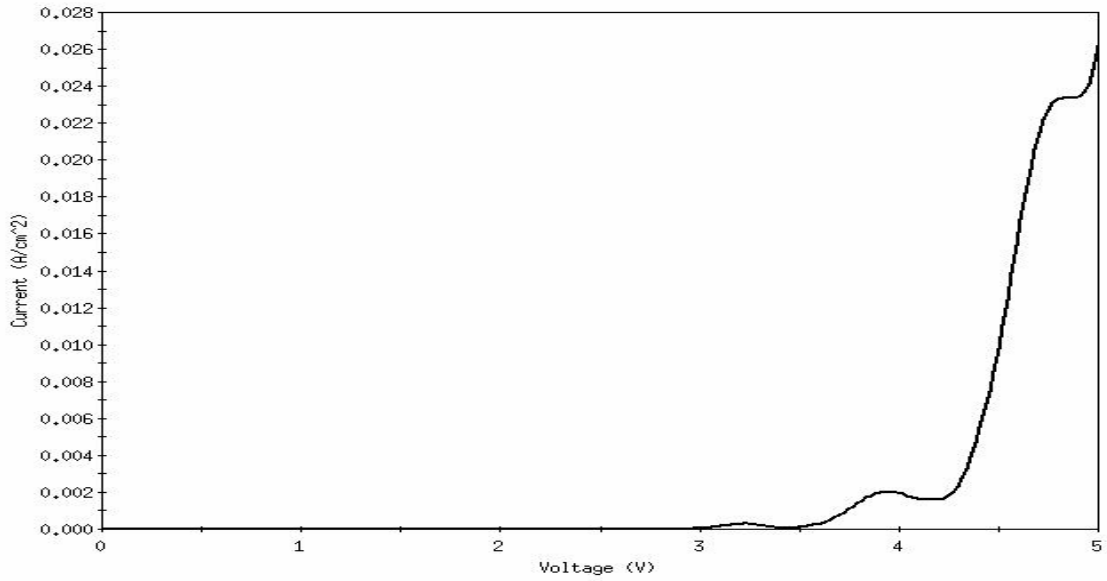


Fig 4.8 Four-band simulations of 16ml BeTe and 29ml ZnSe

The I-V simulation of 14b_29w_14b is shown in Fig 4.7. The I-V simulation of 16b_29w_16b is shown in Fig 4.8. The 29ml ZnSe well was chosen because the resonance finding program was used in NEMO for different thickness of well and the number of resonant states in the well were 3 for 29ml. As the thickness of the well is increased more resonant states come into the well and as they thickness is decrease resonant states are removed from the well. It is seen for the above three simulations for a constant well thickness as the barrier thickness is changed to 12ml, 14ml and 16ml the NDR decreases as well as the current density of the devices. Other results were obtained with similar qualitative NDR regions as shown above for 13b_34w_13b and 14b_34w_14b but the ones shown above were the best 4-band simulations obtained.

The four band simulations showed good qualitative comparison to the positive bias of experimental curves. It showed 3 and 4 NDR regions similar to the experimental

curves. The bias points of the NDR regions were found to start only after 3V and this is typical for parabolic band models in which the resonant states are over predicted and hence the NDR regions. The ten band $sp^3s^*$ model is a non-parabolic model which accurately predicts the resonant states compared to parabolic models and also since the band transport is calculated for ten bands the model is used to model experimental I-V characteristics.

### 4.2.2 Ten-band simulations

The ten band $sp^3s^*$ model was chosen because it can better model our structures with good quantitative and qualitative results. The method in which the $sp^3s^*$ parameters are built has already been shown in Section 4.1.1.The I-V simulations of different parameter sets have also been tried and none gave good results. Ten band simulations of the structure described in Table 4.5 did not show any good curves.

It has already been explained earlier in Chapter 2 of fabrication that the interfaces between ZnSe and BeTe are of no-common atom type interfaces in which the interface does not have a common atom with either of the host materials. These no common atom type interfaces generally have band structure properties very different from the host materials. NEMO has only been used to simulate III-V materials in which usually they have a common anion interface. This work is the first in simulating II-VI materials using multi band models. NEMO does not recognize the interfaces and apply them accordingly. Now these interfaces could be BeSe or ZnTe. Hence the $sp^3s^*$ tight binding parameters for BeSe and ZnTe were obtained and inputted into NEMO. The interfaces are believed to be 2ml to 3ml.Initially addition of BeSe and ZnTe interfaces

did not result in any good simulated curves, therefore only BeSe interfaces were added to the ZnSe-BeTe RTD structure and the simulated structure is shown in Table 4.6.

Table 4.6 Structure of ZnSe-BeTe RTD including BeSe interfaces

| Material | Thickness (nm) | Doping n-type ($cm^{-3}$) |
|---|---|---|
| n+ZnSe | 500 | 5e+18 |
| n-ZnSe | 150 | 5e+17 |
| ZnSe | 10 | - |
| **BeSe** | 2 | - |
| BeTe | 5 | - |
| **BeSe** | 2 | - |
| ZnSe | 6 | - |
| **BeSe** | 2 | - |
| BeTe | 5 | - |
| **BeSe** | 2 | - |
| ZnSe | 10 | - |
| n-ZnSe | 150 | 5e+17 |
| n+ZnSe | 500 | 5e+18 |

The introduction of interfaces gave good qualitative simulations which are shown for different thicknesses. The simulations were done using analytical transverse integration and numerical transverse integration. The effective masses of ZnSe, BeTe ,BeSe and ZnTe were taken from [70,71].The simulation of 1ml interface layer in NEMO is not possible, NEMO needs a minimum of 2ml to simulate any structure. Simulations were also tried with 2ml interface layer and 3ml interface layer. Good results were obtained only with 2ml interface layer. Simulations of structure including BeSe interfaces for different thickness were tried and are shown below. Simulation of 12b_32w_12b is shown in Fig 4.9.Simulation of 13b_29w_13b is shown in Fig 4.10. Simulation of 16b_29w_16b is shown in Fig 4.11.

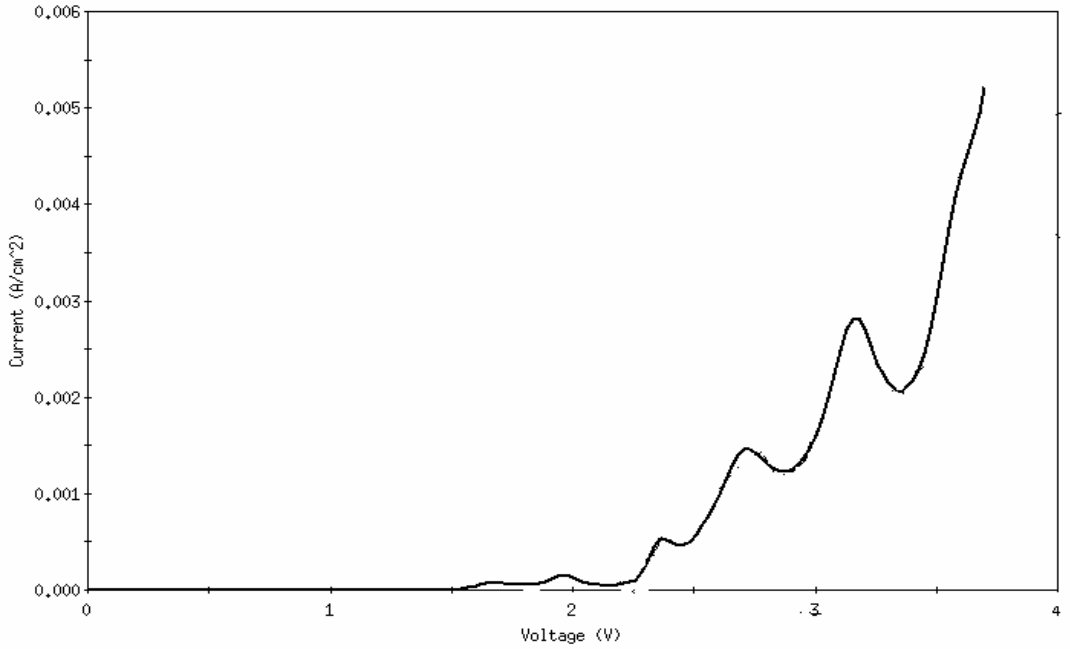


Fig 4.9 Simulation of structure with 12ml BeTe and 29ml ZnSe and 2ml BeSe

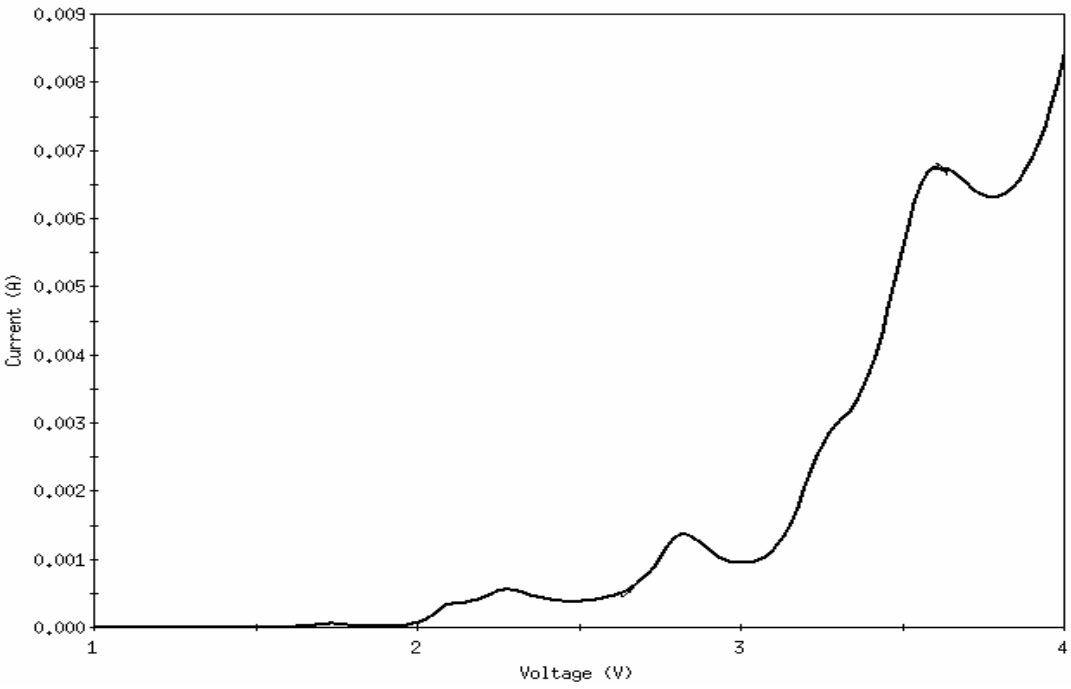


Fig 4.10 Simulation of structure with 13ml BeTe and 29ml ZnSe and 2ml BeSe

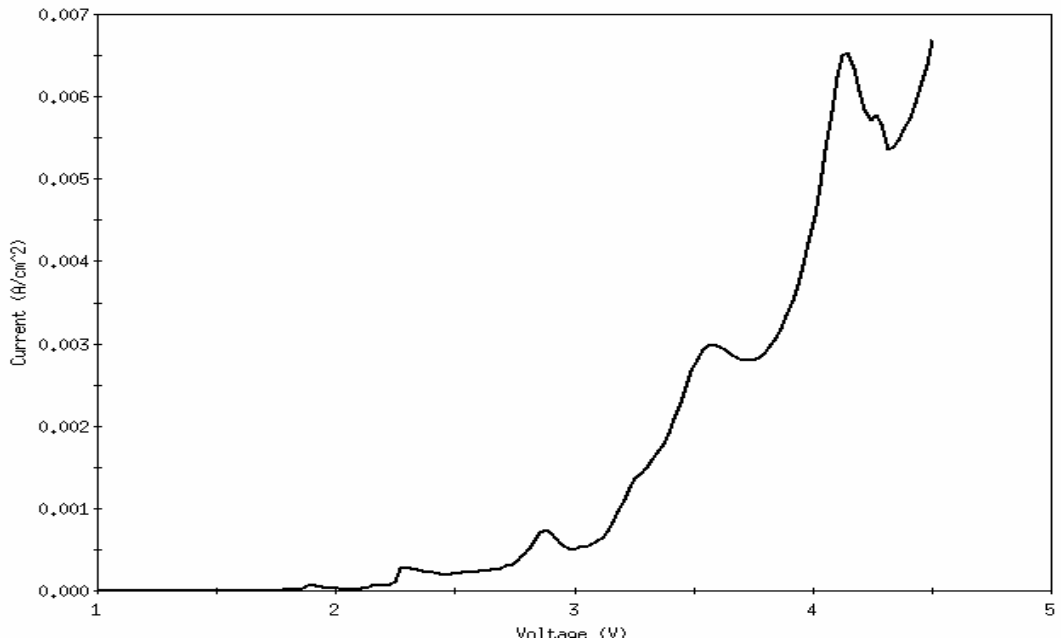


Fig 4.11 Simulation of structure with 16ml BeTe and 29ml ZnSe and 2ml BeSe

As seen in Chapter 3 the experimental characterization of our devices showed asymmetrical I-V characteristics. Some of the sources of asymmetrical I-V characteristics could have been from the interfaces being non-equivalent during MBE growth and asymmetric doping in the on either side of the quantum well in the emitter and collector. The above two sources were explored using NEMO simulations. In order to check for asymmetry whether it was inherent of the type-II transitions happening in in the ZnSe-BeTe RTD.A scan from negative to positive voltages for the structure with only BeSe interfaces was simulated. The I-V characteristic simulation of 12b_25w_12b with only BeSe interfaces is shown in Fig 4.12.The result showed symmetrical I-V characteristics. Although there is a known optical anisotropy in ZnSe-BeTe hetero

structures with different interfaces [72], but no results reported of asymmetrical I-V characteristics of ZnSe-BeTe RTD.

The band offset between ZnSe-BeTe proved to be very important to get simulation results with good comparison to experimental values. The valence band offset between ZnSe and BeTe is known to be 0.9eV.The $sp^3s^*$ tight binding parameters were modified to get this band offset. I-V simulations were tried for band offsets of around 0.9eV the theoretical value. Valence band offsets of 0.6eV, 0.7eV, 0.8eV, 0.9eV and 1eV were simulated, but only 0.6eV showed good results.

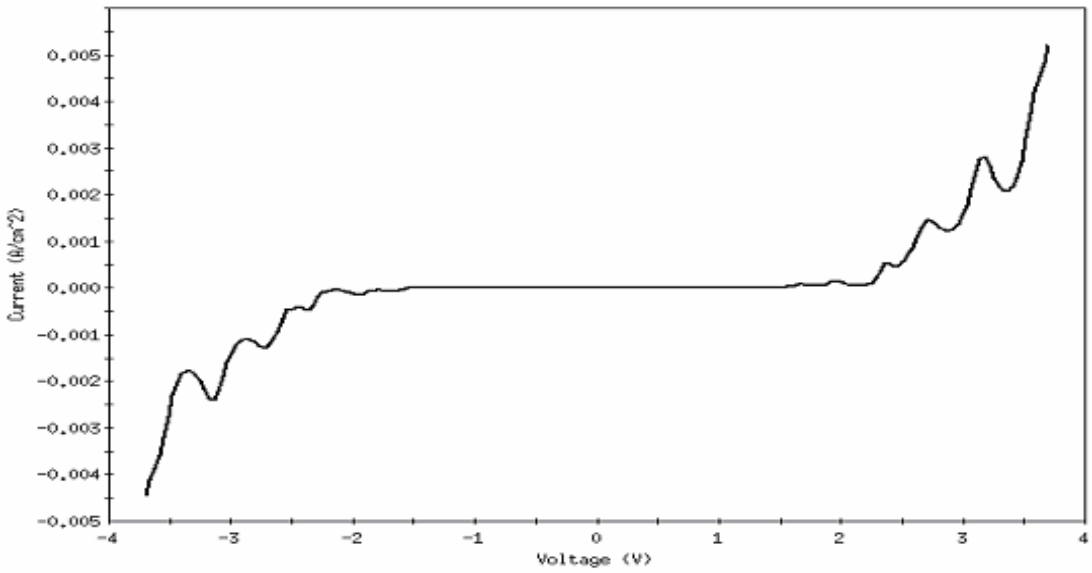


Fig 4.12 Simulation of structure with 12ml BeTe and 25ml ZnSe and 2ml BeSe only

It has been explained in Chapter 2 during MBE growth of ZnSe-BeTe RTD, the interfaces of BeSe and ZnTe are expected to be alternating in our type of growth. When BeTe is grown on ZnSe the interface is ZnTe and when ZnSe is grown on BeTe the

interface is BeSe. The interfaces are added to the simulation structure and the expected band profile is shown in Fig 4.13.

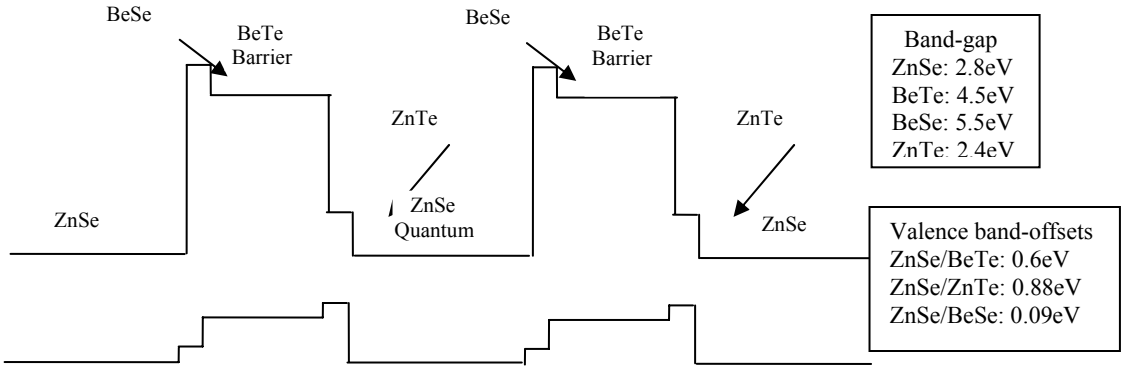


Fig 4.13 Staggered band profile generated by inclusion of interfaces

Staggered band profiles for other type-II semiconductors modified by interfaces are shown in [73].The band gaps of BeSe and ZnTe are taken as 5.5eV and 2.4eV.The band offsets between different materials which are mentioned in Fig 4.13 were taken from theoretical calculations by Bernadini *et al* [69].The details of the simulated structure including both BeSe and ZnTe interfaces is shown in Table 4.7.

Table 4.7 Structure of ZnSe-BeTe RTD including BeSe and ZnTe interfaces

| Material | Thickness (nm) | Doping n-type ($cm^{-3}$) |
|---|---|---|
| n+ZnSe | 500 | 5.00E+18 |
| n-ZnSe | 150 | 5.00E+17 |
| ZnSe | 10 | - |
| **BeSe** | 2 | - |
| BeTe | 5 | - |
| **ZnTe** | 2 | - |
| ZnSe | 6 | - |
| **BeSe** | 2 | - |
| BeTe | 5 | - |
| **ZnTe** | 2 | - |

Table 4.7 - *continued*

| | | |
|---|---|---|
| ZnSe | 10 | - |
| n-ZnSe | 150 | 5.00E+17 |
| n+ZnSe | 500 | 5.00E+18 |

By keeping the simulations parameters and band offsets between ZnSe and BeTe constant as for the simulation shown in Fig 4.12.Only by changing the interfaces from all BeSe interfaces to alternating BeSe and ZnTe interfaces a simulation with similar thickness of 12b_25w_12b was simulated and is shown in Fig 4.14.

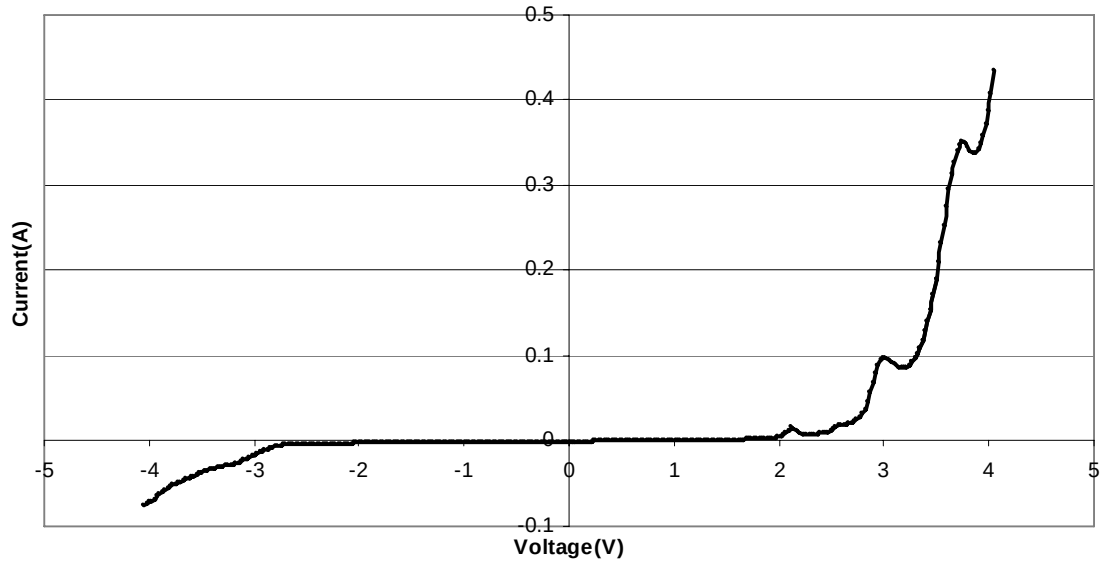


Fig 4.14 Simulation of structure with 12ml BeTe and 25ml ZnSe and 2ml BeSe, ZnTe

The comparison of simulated curves in Fig 4.12 and Fig 4.14 tell us that by changing the interfaces from pure BeSe interfaces to alternating interfaces of BeSe and ZnTe showed a difference from symmetrical characteristics to asymmetrical I-V characteristics. The simulated curve in Fig 4.14 has 3 NDR regions in the positive side and no NDR regions on the negative side, but there is an asymmetry in magnitude of

current from the positive bias to the negative bias, this qualitatively follows the experimental characteristics seen in Chapter 3 except for the NDR regions in the negative side

The band profiles generated in NEMO for only BeSe interfaces is shown in Fig 4.15 and that of alternating interfaces of BeSe and ZnTe is shown in Fig 4.16.

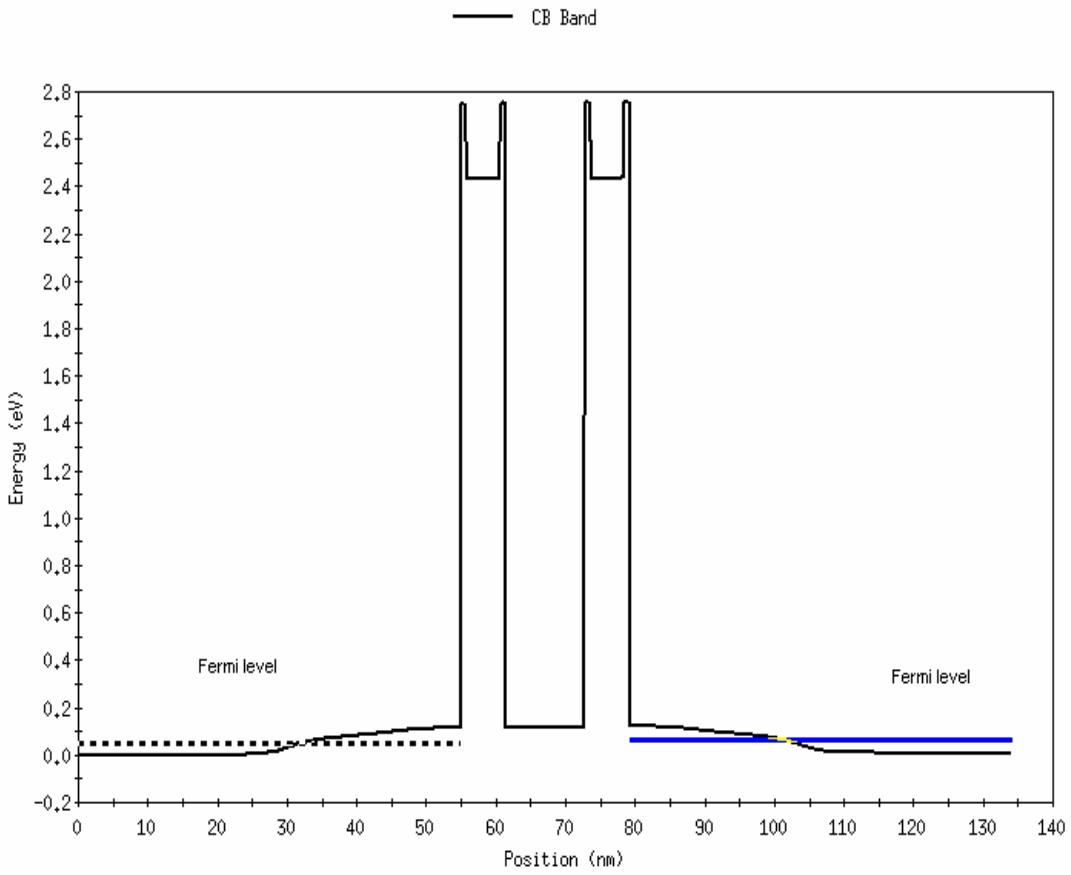


Fig 4.15 Band profile of ZnSe-BeTe RTD with only BeSe interfaces in NEMO

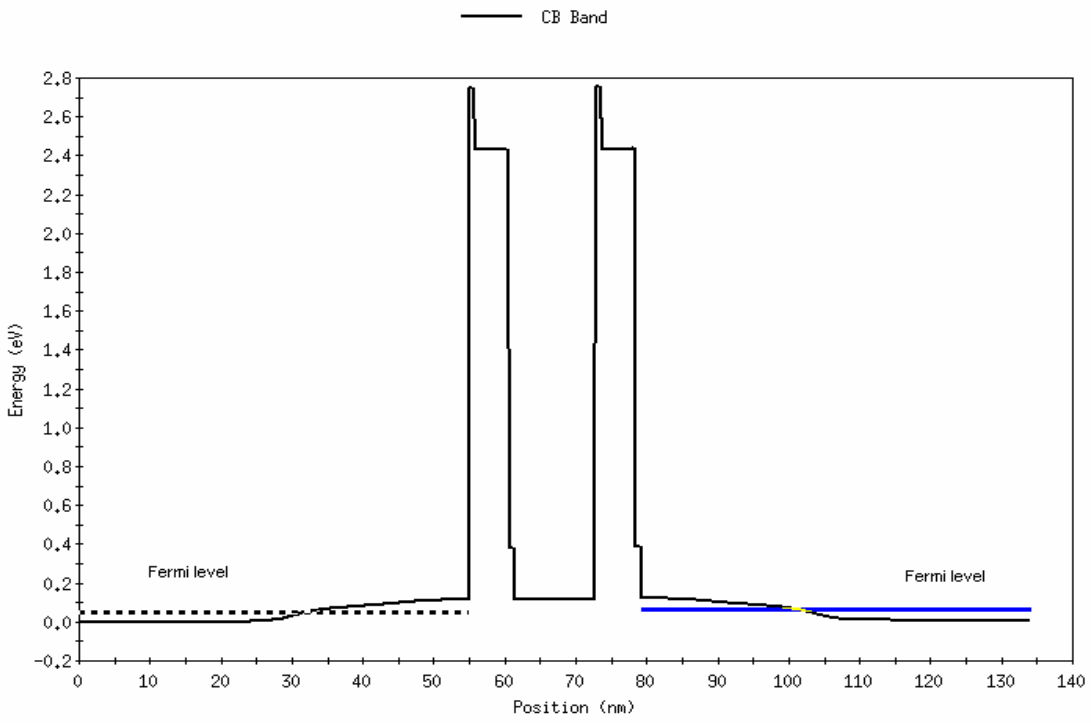


Fig 4.16 Band profile of ZnSe-BeTe RTD with BeSe and ZnTe interfaces

It can also been seen from the band profiles that the resonant electron tunneling is affected by the difference in interfaces. When the electron is moving from left to right which is for a positive bias applied in the case of only BeSe interfaces it experiences the same potential barriers as when the electron is moving from right to left for a negative applied bias. Considering the case of alternating BeSe and ZnTe interfaces the electron experiences different potential barriers for positive and negative biases. Since this is a type-II band alignment, the type-II transitions are also affected by these alternating interfaces. For the total current there is a contribution from the resonant electron tunneling in the conduction band as well as the type-II transitions. Our investigation for asymmetric I-V characteristics using NEMO simulations shows asymmetric NDRs as

well as asymmetry in current magnitude by using alternating interfaces of BeSe and ZnTe as expected from our MBE growth.

Another source for asymmetry in I-V characteristics in experiment could be from asymmetric doping on either side of the quantum well. Keeping the configuration with all BeSe interfaces which yielded symmetrical curves (Fig 4.12) we changed the doping of emitter and kept the collector doping constant. The target doping for $n^+$-ZnSe was $5e^{18}$ $cm^{-3}$ and n-ZnSe was $5e^{17}$ $cm^{-3}$. We have changed the doping of emitter to $7e^{18}$ $cm^{-3}$ ($n^+$-ZnSe) and $7e^{17}$ $cm^{-3}$(n-ZnSe). We have also changed the doping of emitter to $9e^{18}$ $cm^{-3}$ ($n^+$-ZnSe) and $9e^{17}$ $cm^{-3}$(n-ZnSe).The curves with different asymmetric doping are shown in Fig 4.17.In the negative side the characteristics coincide because the doping of the collector was kept contant, whereas on the positive side the curves had different current magnitudes and positions of NDRs for different doping.

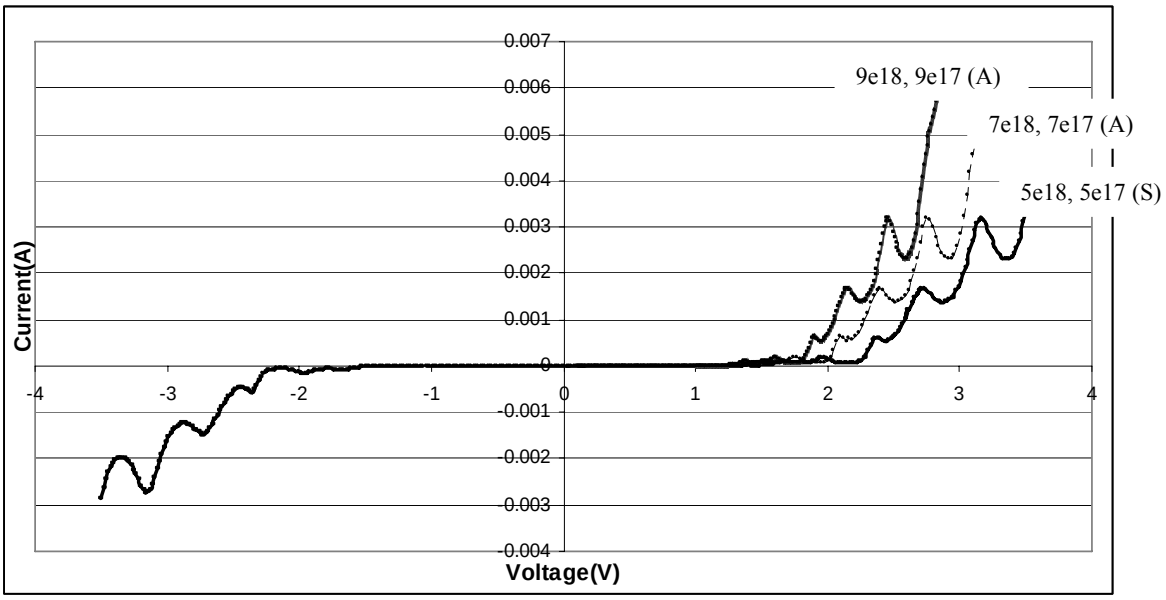


Fig 4.17 -Asymmetric doping simulations, (A) indicates asymmetric doping and (S) indicates symmetrical doping

The change in doping would change the Fermi-level in the emitter and hence make a change in the current magnitude and position of NDR regions, but did not change the number of NDRs. The effect of asymmetric doping did not impact the asymmetry of the current-voltage characteristics as much as the change interfaces did in our simulations. Asymmetric doping in the emitter and collector can be seen as a smaller factor compared to inclusion of alternating interfaces.

To further model the experimental characteristics using NEMO the band-offsets between the interface materials of BeSe and ZnTe were changed with respect to the ZnSe. So far the simulation curves showed 3 NDRs in the positive region and no NDRs in the negative region. In our experimental curves there were 3 NDRs in the positive region and 2 NDRs in the negative region. Band offsets between BeSe and ZnSe as well as ZnTe and ZnSe were changed in order to get better simulation results. All the valence band offsets were adjusted with respect to the valence band of ZnSe. The band offsets between the interface materials taken from Ref [69] are theoretical band-offsets which in experiment might be different , therefore the band offsets were changed to model experimental curves by changing the band offsets around the theoretical value. The theoretical valence band offset between ZnSe/BeSe is 0.09eV and ZnSe/ZnTe is 0.88eV.Initially the ZnSe/BeSe was changed between 0.08eV and 0.12eV and 0.1eV gave very I-V simulations similar to the experimental curves in positive bias. Adjust - ments of valence band offsets were done by keeping the overall band gap of the material constant. Now the requirement was to model the experimental curve both in the

positive and the negative bias. Adding of ZnTe interfaces along with BeSe interfaces gave us good results as shown in Fig 4.14. The ZnSe/ZnTe valence bands offset were changed between 0.75eV and 1eV.Good qualitative results were obtained for ZnSe/ZnTe of 0.9eV keeping the ZnSe/BeSe offset constant at 0.1eV shown for 12b_18w_12b in Fig 4.18.These simulations showed an increase in current in the negative bias maintaining the positive NDRs.There are some features in the negative bias but no NDR compared to the experimental curves. The band offsets were further tweaked to get a ZnSe/BeSe band offset of 0.11eV and ZnSe/ZnTe band of 0.93eV offset to get better simulation results which is shown for 12b_25w_12b in Fig 4.19.

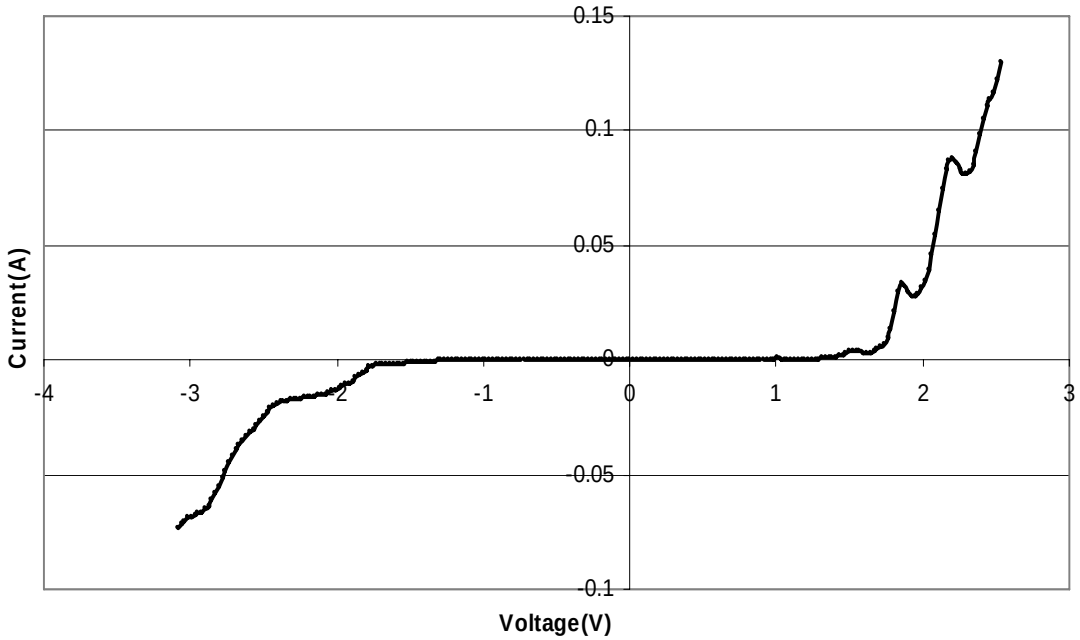


Fig 4.18 I-V simulations by changing the ZnSe/ZnTe valence band offset

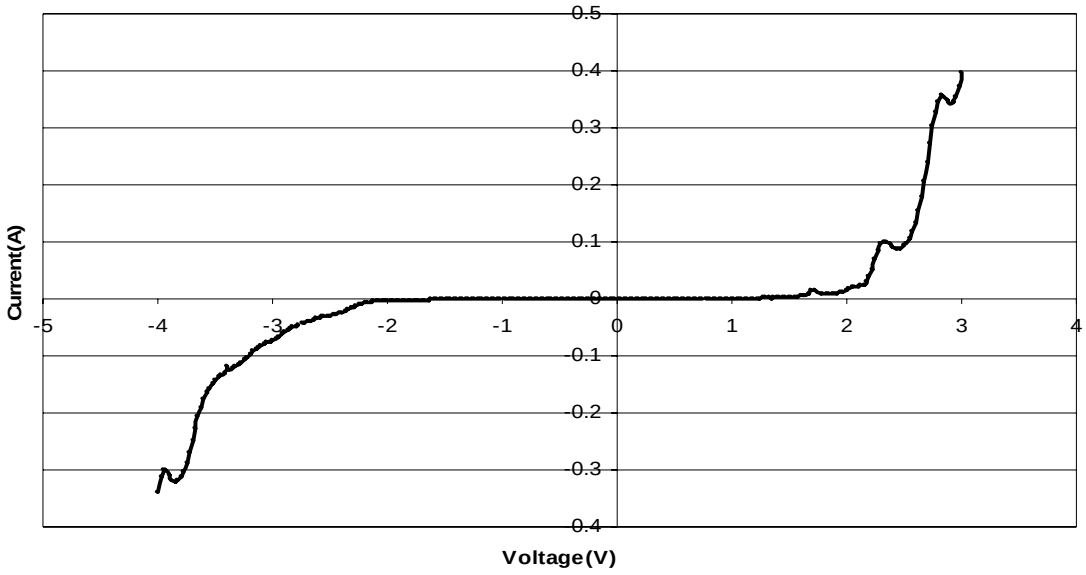


Fig 4.19 I-V simulations by changing the ZnSe/BeSe and ZnSe/ZnTe band offsets

The I-V simulations shown in Fig 4.19 show a qualitative comparison with experimental characteristics of sample Z 543 and Z 586.There are 3 NDRs in the positive region and 2 NDRs in the negative region for simulated and experimental curves. In order to get good simulations for target thickness of barriers and wells which are 18ml BeTe barriers and 22ml ZnSe wells, the thickness of barriers and wells were increased close to theoretical thickness and to get good results the ZnSe/ZnTe and ZnSe/BeSe offset was further tweaked. The conduction band offset of ZnSe/BeSe was changed while still maintaining the valence band offset and compensating the band gap. The conduction band offset was changed from 2.8eV to 2.7eV reducing the band gap of BeSe from 4.5eV to 4.4eV. Some of the simulations with barrier and well thickness close to experimental target thickness are shown below. An I-V simulation of 14b_18w_14b is shown in Fig 4.20.

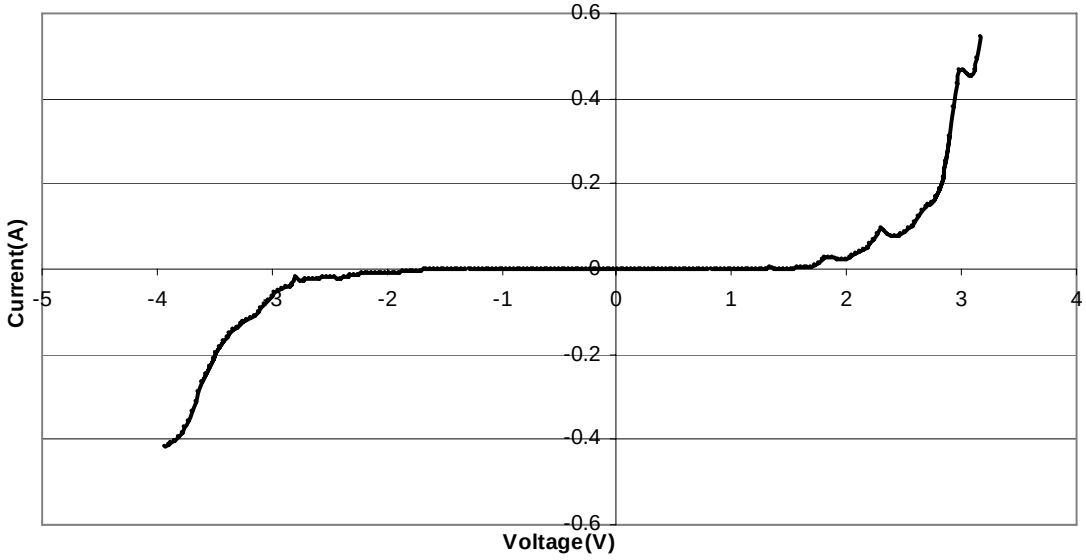


Fig 4.20 I-V simulations of 14ml BeTe barriers and 18ml ZnSe well

An I-V simulation of 18b_18w_18b is shown in Fig 4.21 with the same parameters as for simulation in Fig 4.20.

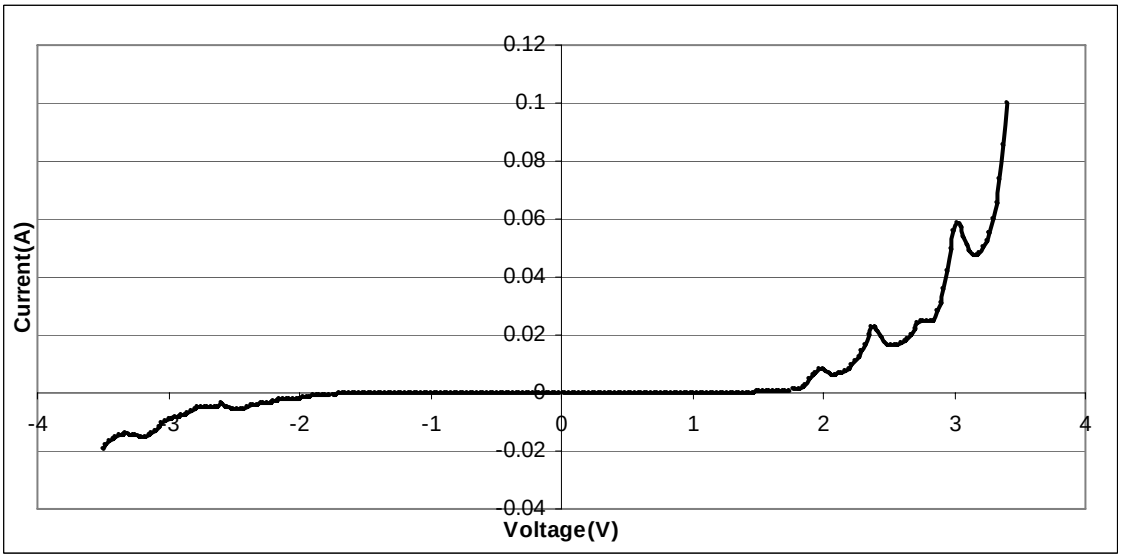


Fig 4.21 I-V simulations of 18ml BeTe barriers and 18ml ZnSe well

Simulation showed in Fig 4.21 in which the well thickness is about 4ml different from the target thickness of 22ml.The barrier thickness is the same as target thickness. The curve looks qualitatively similar to the experimental ones but there is an additional small peak between the 2nd and 3rd NDR which was not observed in simulations with thinner barriers. The negative bias region has 2 NDR regions and the curve has asymmetric magnitude of current. Another I-V simulation of 16b_20w_16b is shown in Fig 4.22.This one is similar to the previous simulation in terms of NDRs on the positive and negative biases , there is an additional feature between the 1st NDR region and the 2nd NDR region for the positive region. Another simulation closest possible to the target MBE thickness was simulated for 17b_22w_17w which is shown in Fig 4.23. For simulations of exact target thicknesses, adding one more monolayer showed additional pronounced NDRs between the regular NDR regions observed.

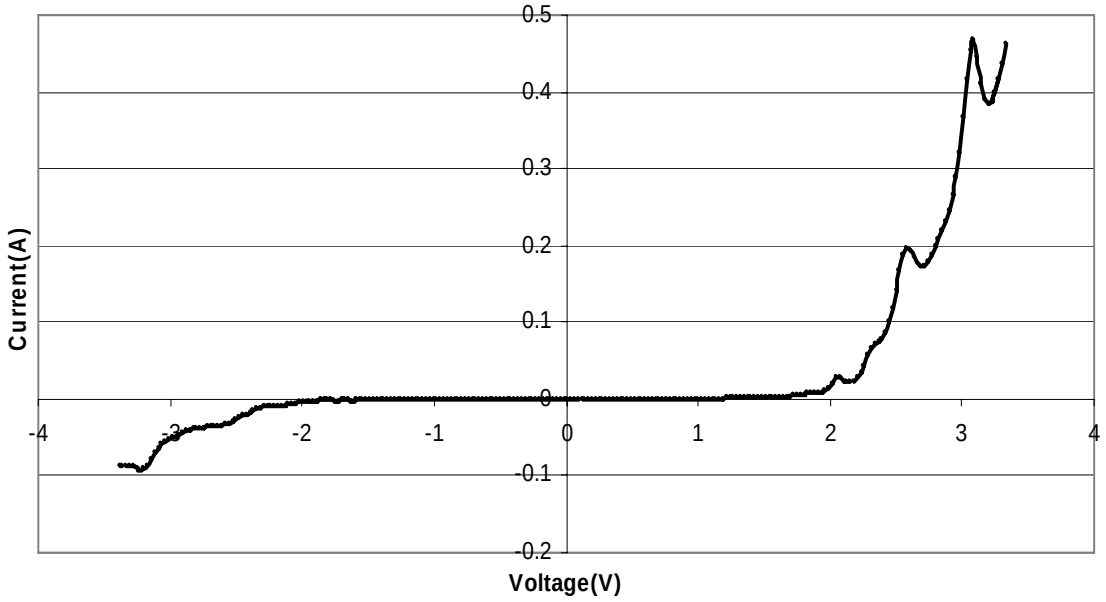


Fig 4.22 I-V simulations of 16ml BeTe barriers and 20ml ZnSe well

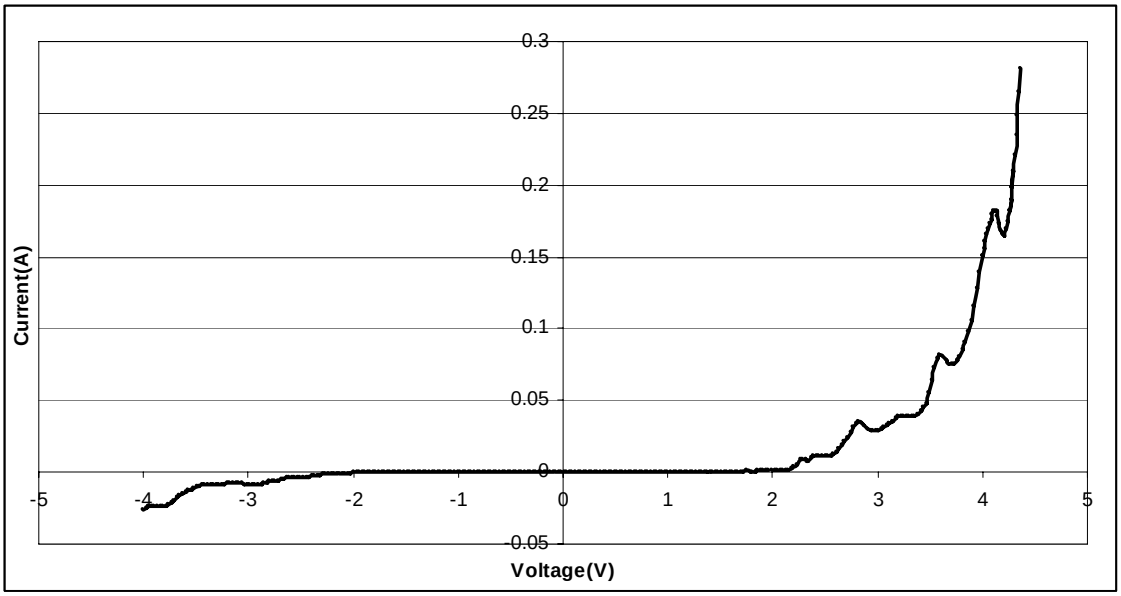


Fig 4.23 I-V simulations of 17ml BeTe barriers and 22ml ZnSe well

As thicker barriers and wells were simulated there were additional resonances formed which showed additional NDRs in the I-V characteristic simulations. It was found in simulations that increasing the width of the well not only introduced more resonances into the well but for a fixed number of resonances in a well increasing the width of the well caused the resonances to be closer to each other, whereas if the width of the well was decreased then this would cause the resonances to get further apart from each other and move to higher resonant energies. This would mean that the position of the NDR regions can be controlled by changing the width of the well and keeping other parameters constant. For multiple NDR devices like ZnSe-BeTe devices they need to be spread as far as possible, because the valley region of the first NDR depends on how close the second NDR is, if it is farther the valley current will be lower and hence more PVR.This also applies to the second and the third NDR.The most important factor in

getting good qualitative curves compared to experiment was addition of alternating interfaces of BeSe and ZnTe and adjusting the band offsets between the interface materials and ZnSe.Some of the simulations shown above had currents in milli amperes which quantatively compares to experimental values of sample Z 599.Simulations for different doping showed an increase in current density as well as the position of NDRs moving closer to zero bias. Qualitative and quantitative comparisons of simulations and experiment will be discussed in Chapter 5.

# CHAPTER 5

# DISCUSSIONS

In this chapter the different sources of asymmetric I-V characteristics in our ZnSe-BeTe RTDs investigated will be discussed. The qualitative and quantitative comparison of simulated curves to experimental curves will be discussed. A summary of all samples grown and their corresponding I-V characteristics will be discussed. The use of NEMO simulation tool in this work is summarized. Thermally assisted tunneling and effect of Fermi-level adjustment on PVR using NEMO simulations is investigated. The effect of having BeSe and ZnTe interfaces on structural aspects of ZnSe-BeTe heterostructures will be outlined based on literature.

## 5.1 Asymmetric I-V characteristics

The asymmetrical I-V characteristics in experiment were shown in Chapter 3 of different samples. There has been no report in literature of investigation of asymmetrical I-V characteristics of no-common atom system ZnSe/BeTe RTDs.We have studied the different sources of asymmetry in these devices.

SEM(Scanning electron microscopy) and TEM(transmission electron microscopy) were done on sample Z 543 which is shown in Table 5.1.The thickness of barriers were symmetrical in both the experiments.

Table 5.1 SEM and TEM thickness of Z 543 showing symmetrical barriers

| | Target(MBE) | SEM | TEM |
|---|---|---|---|
| Barrier(BeTe) | 50 | 61 | 50.2 |
| Well(ZnSe) | 60 | 72 | 78.2 |

The asymmetrical thickness in barriers did not show much difference in NEMO simulations, it did not change the qualitative results too much and remained symmetrical on both positive and negative side. The result in which the doped layers were halved in experiment from sample Z 543 to Z 586 did not change characteristics qualitatively.

The thickness of emitter and collector doped layers did not show much change in the I-V simulations. The thicknesses of doped layers were made asymmetric and did not cause much difference in characteristics as long as the doping was preserved. This was also experienced in experiment when the etching was done through the double barriers and into the bottom doped layers once the highly doped ZnSe is reached, the I-V characteristics do not change even after it is etched more into the ZnSe.

The Al/n-ZnSe contact of our devices was suspected to induce the asymmetry in our devices. The Al/n-ZnSe contact was suspected to be schottky in nature. In section 3.3 of Chapter 3 the Al/n-ZnSe was experimentally shown to be ohmic in nature. In our process the n-ZnSe top is transferred in-situ into a III-V group chamber and Aluminum is grown on it to provide for protection against oxidation of ZnSe as well as a good electrical contact on n-ZnSe.In-situ deposited aluminum proved to have good ohmic contacts on ZnSe for doping of 5e18 $cm^{-3}$. The higher doping the more ohmic the

Al/ZnSe contact. This source was eliminated as a contribution to the overall asymmetric characteristics. During the fabrication of RTD a rectifying effect was seen in the I-V characteristics shown in Section 3.3 of Chapter 3 which seemed to be coming from the active region or quantum well part of the device. Different sources of this rectifying effect were checked. This rectifying effect was suspected to come from the n+-ZnSe and n-ZnSe although both regions were highly doped close together. This was eliminated by observation of the same rectifying effect seen in samples Z 593 and Z 594 during fabrication which were grown only with one highly doped ZnSe on either side of the quantum well. Another source of this rectifying effect was thought to come from the top doped ZnSe layers and un-doped quantum well, but the argument is that a reverse effect to be seen when going from the un-doped quantum well to the bottom doped ZnSe layers which would result in symmetrical characteristics. The etching in the fabrication were done using theoretical thickness and the etch depth using a profilometer.The theoretical grown thickness compares very close with the experimental thickness and during etching it was found that the thickness where the rectifying effect was seen was just after crossing the quantum well.

In section 2.1 of chapter 2 it is understood that in our type of MBE growth of ZnSe-BeTe RTDs the interfaces between ZnSe and BeTe are alternating BeSe and ZnTe interfaces because the growth of ZnSe and BeTe is terminated with Se and Te respectively. The termination of Se or Te was confirmed by the RHEED patterns seen during the growth. The non-equivalent interfaces of BeSe and ZnTe in the quantum well of ZnSe-BeTe RTDs were investigated for the source of asymmetry in I-V

characteristics. The band profile generated in NEMO for with interfaces is shown in Fig 5.1.The Fermi-levels and also the graded doping caused by un-doped spacer , lower doped ZnSe and higher doped ZnSe is shown.

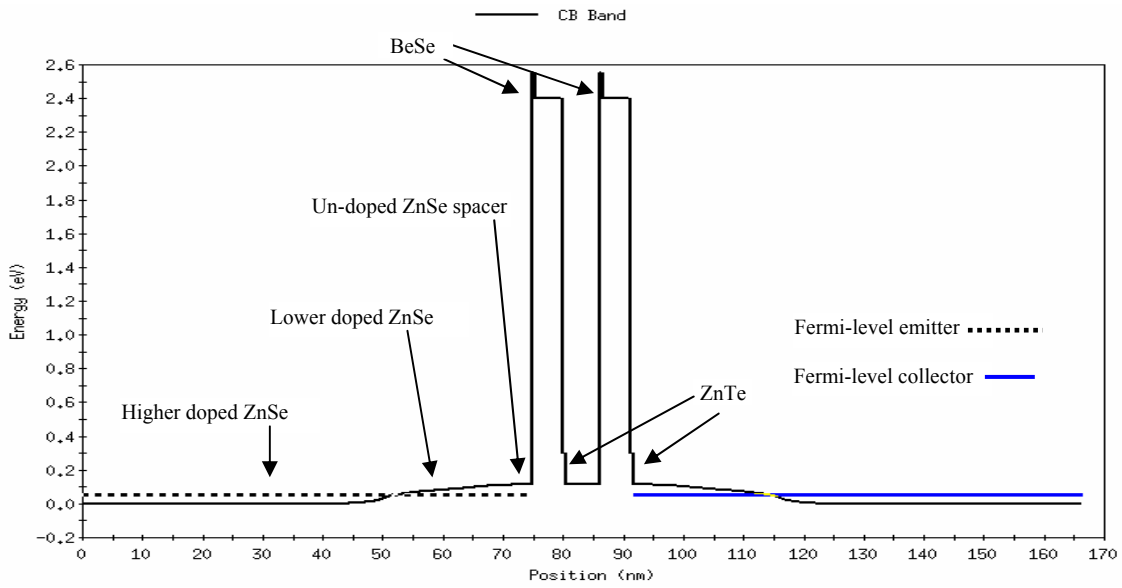


Fig 5.1 Band profile simulated in NEMO showing interfaces and graded doping

In section 4.2.2 of Chapter 4, NEMO simulations of ZnSe-BeTe RTD structure with both BeSe and ZnTe interfaces showed asymmetrical characteristics compared to symmetrical characteristics with only BeSe interfaces simulations. It was seen that the inclusion of interfaces of BeSe and ZnTe in the RTD structure altered the band profile and made it asymmetric about the center ZnSe quantum well. These interfaces although only 2ml thick showed a different in transport for positive and negative biases and hence I-V characteristics in NEMO simulations. The inclusion of alternating interfaces of BeSe and ZnTe similar to our growth conditions in our samples showed good qualitative comparison of simulation with experiment.

Another source of asymmetric doping in the emitter and collector was investigated using NEMO simulations in section 4.2.2 of Chapter 4. The doping of the emitter was kept constant changing the graded doping of the collector only and this showed difference in current density and position of NDRs but it qualitatively preserved the curves. This was not the case in our experimental curves, where the positive bias regions were qualitatively different from the negative bias regions. The positive regions have 3 NDRs and negative regions have 2 NDRs which are spaced further apart than the positive ones. The doping on either side of the quantum can change the Fermi-level which would increase or decrease the current , but the number of NDRs changing cannot be explained with asymmetric doping. The dopant segregation and change in dopant profile in the emitter and collector can change the shape of the triangular potential well formed between the doped layers and the quantum well when biased. The formation of the triangular potential well from the graded doping is under a bias is shown in Fig 5.2. In samples Z 593 and Z 594 the altering of dopant profile was minimal since there was only one doped ZnSe and an un-doped spacer on either side of the quantum well and these devices still showed asymmetrical characteristics. The change in the undoped spacer causes a change in the triangular well which seemed to increase the current but the asymmetry was still prevailing.

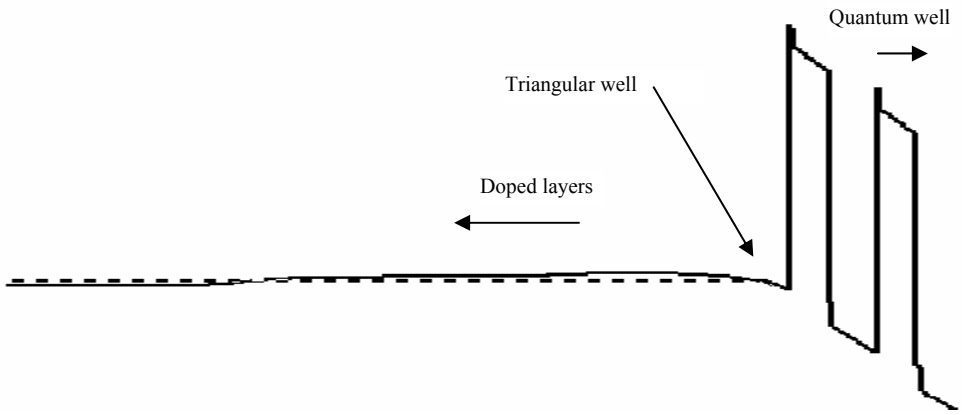


Fig 5.2 Formation of triangular well at the un-doped spacer region between the doped layers and the quantum well

There has been a lot of research done on optical anisotropy of ZnSe/BeTe super lattices with different interface configurations [74, 75].They indicate in no-common atom systems like the ZnSe/BeTe the optical anisotropy is purely due to the different interfaces and their configurations. In a ZnSe/BeTe single quantum well there are 4 interfaces possible and they can be all BeSe or all ZnTe or BeSe and ZnTe alternating starting with either BeSe or ZnTe.

It has been reported with photoelectron spectroscopy results that the band offsets between ZnSe and BeTe depend on the growth process and more specifically the stoichiometry. The ZnTe interfaces were reported to have a valence band offset of 1.26 ± 0.15 and BeSe-like interfaces 0.46 ± 0.15 eV [76].There is a small variation within the band offsets depending upon the strain induced effects, but there is still a large difference between offsets of interfaces of ZnTe and BeSe.Yamakava et al have done cross-sectional tunneling microscopy (XSTM) to characterize ZnSe/BeTe heterojunctions and found by changing the biases there was brightness difference

attributed to the offsets in the conduction and valence bands of different interfaces in growth of ZnSe/BeTe quantum wells. The structures which they have studied have similar growth details compared to our growth. They have also found that the roughness amplitudes and correlation lengths of different interfaces. The interface with BeTe on ZnSe has a correlation length of 15.5nm which is longer compared to interface with ZnSe on BeTe having a correlation length of 12.5nm [77].The interface roughness due to BeSe and ZnTe will be different and hence will cause difference in scattering. They have also found using XSTM and X-ray diffraction (XRD) the existence of BeSe and ZnTe at the interfaces of ZnSe and BeTe depending upon the growth [78].All these experimental details lead to a point of saying that growth of no common atom ZnSe/BeTe quantum wells will have either BeSe or ZnTe interfaces which will eventually alter the electronic properties of the ZnSe/BeTe quantum well devices.

Other no-common atom III-V systems like the AlSb/InAs system have interfaces of InSb and AlAs. Whitman et al demonstrated AlSb/InAs RTD and obtained asymmetrical I-V characteristics when the interfaces were mixed InSb and AlAs, when the interfaces were forced to be all InSb they obtained symmetrical I-V characteristics. It was also found by them that the interfaces and their roughness played an important role in their characteristics [79].The asymmetry in I-V characteristics in RTDs was also studied by Rudberg et al [80] and was attributed to the interface roughness being different at the transition from one material to the other. The roughness difference at different interfaces of the quantum well is shown as an example in Fig 5.3. Roughness A is more than Roughness B.

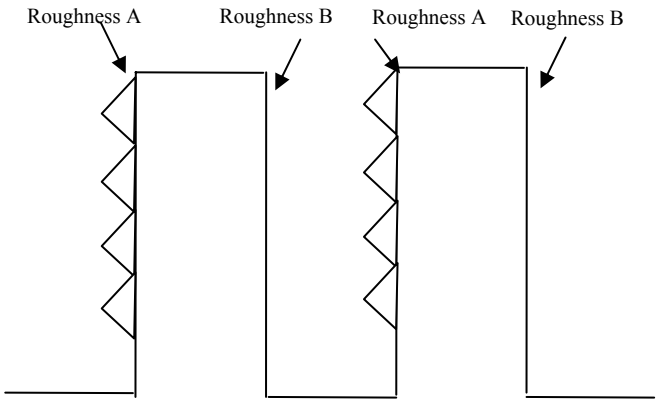


Fig 5.3 Roughness at alternating interfaces of quantum well

After investigating different sources of asymmetry in I-V characteristics using NEMO simulations and I-V characteristics during fabrication and evidence of a difference in valence band offset in literature, the main source of asymmetry should come from the interfaces in the no common atom system of ZnSe/BeTe RTDs being non-equivalent.

5.2 Summary and comparison of simulated and experimental characteristics

The I-V characteristics of samples Z 543, Z 586, Z 563, Z 593, Z 594 and Z 599 is shown in Chapter 3 of characterization. These samples were obtained by making changed in thickness of doped layers, increasing doping of doped layer, changing the spacer thickness and removal of lower doped ZnSe layers on either side of the quantum well. There were neither changes made in the type of quantum well growth nor the thickness of the barriers and well. Samples Z 543, Z 586 and Z 599 had good qualitative comparison of curves among them in which there were 3 NDRs in the positive and 2 NDRs in the negative with asymmetrical current magnitude. The common feature

among all samples is the asymmetric current magnitude for the positive and negative biases. It was found that the graded doping formed by the un-doped spacer, lower doped ZnSe and higher doped ZnSe on either side of the well was essential to get NDR at room temperature. The graded doping in the emitter and collector essentially forms the triangular potential well. The width and depth of the triangular potential well depends on the thickness and doping of the doped layers. The removal of lower doped ZnSe in samples Z 593 and Z 594 resulted in no NDR at room temperature. The increase in thickness of un-doped spacer causes the width of the triangular well to increase and cause more accumulation of electrons and hence will increase the current density. Although no NDR was observed in sample Z 593 and Z 594 there was an increase in current density by increasing the un-doped spacer thickness. There was also a large increase in current density in Z 599 when compared to Z 586 by increasing the doping of the emitter and collector.

NEMO simulations of the ZnSe-BeTe RTD structure including BeSe and ZnTe interfaces shown in Chapter 4 showed good qualitative comparison with samples Z 543, Z 586 and Z 599.The I-V characteristic of Z 586 is compared with NEMO simulation below in Fig 5.4 and Fig 5.5.

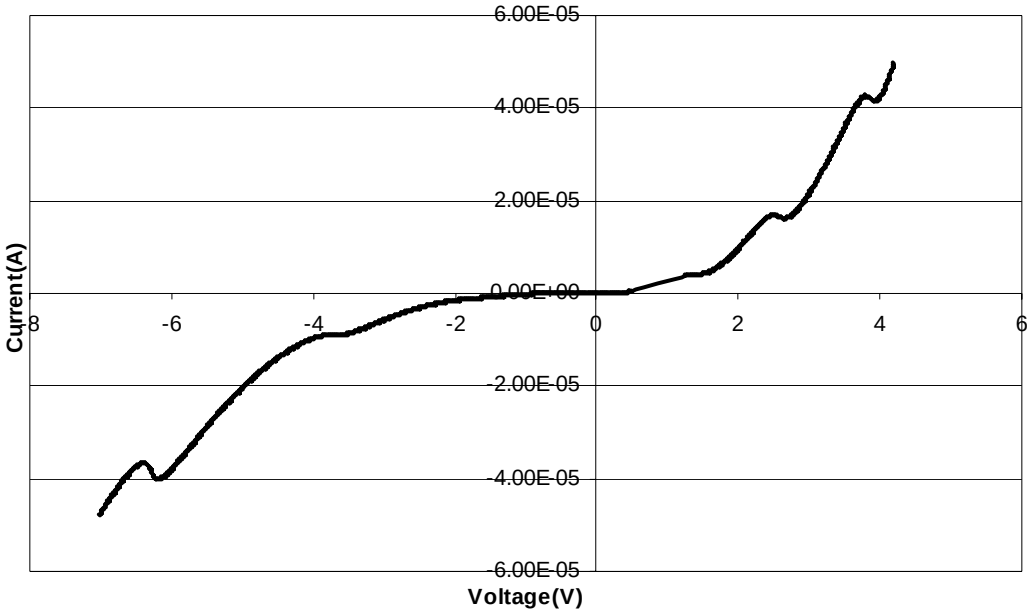


Fig 5.4 Experimental ZnSe/BeTe RTD of sample Z 586

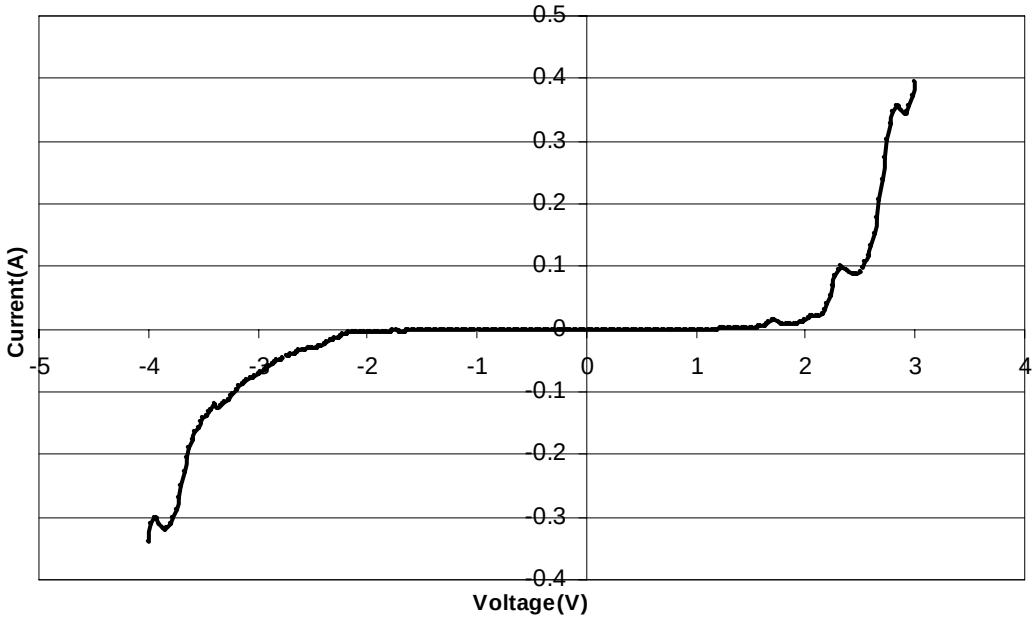


Fig 5.5 NEMO simulated curve of ZnSe/BeTe RTD

Simulated curve has good qualitative comparison with the experimental curve both the curves have 3 NDRs in the positive region and 2 NDRs in the negative region. All the experimental characteristics were done for 150um devices and all the simulations were also done for 150um cross-section of the device.The current is in the range of micro-amperes for most of the experimental characteristics. The above comparison of experimental to simulated curves the experimental current is in the range of micro-amperes and the simulated curve is tenths of amperes. Some of the simulated curves for thicker barriers and wells shown in Chapter 4 have currents in the range of micro-amperes which compares well with sample Z 599 which also has currents in the range of micro-amperes. Although the doping in simulations used were lower than that of Z 599.Better quantitative simulation results can be obtained by further tweaking the valence band offsets. The valence band offset between ZnSe and BeTe used was 0.6eV, the current was seen to increase by lowering this band-offset. The improvements that can be made to get better quantitative and qualitative in NEMO simulations will be discussed in Chapter 6. NEMO proved to be a powerful tool in this work.NEMO was used to investigate different sources of asymmetry by inclusion of interfaces , asymmetric thickness of barriers and doped regions in emitter and collector, asymmetric doping. The expected band profiles of the grown RTD structures were understood and simulated using NEMO. The use of $sp^3s^*$ tight binding parameters to generate the band structures and band offsets provided a good understanding of band profiles. NEMO was successfully used to qualitatively model the asymmetric I-V characteristics of multiple NDR ZnSe/BeTe resonant tunneling diodes. Thermally assisted tunneling and effect of

raising the Fermi-level on PVR simulations which will be shown next sections in this chapter were done using NEMO.

## 5.3 Thermally assisted tunneling and Fermi level adjustment

In Chapter 3, section 3.4 low temperature I-V characteristics at 3.2K showed a decrease in current density from room temperature 300K.The current density decreased by an order. There was also a decrease in current density of ZnSe/BeTe RTD by the same amount at 4.2K Lunz *et al* [6] for the same amount of doping.

There was a variation in terms of current density with change in temperature. When the separation between the Fermi level of emitter or collector is far below the first resonant state in the well the energy required for the electrons to get to the first resonant state in order to tunnel through is supplied by thermal energy this is called thermally assisted tunneling.

The ZnSe/BeTe RTD structure was simulated for lower temperatures shown in Fig 5.6.The structure was simulated for 300K, 270K and 250K, for regular doping of 5e18 $cm^{-3}$ in n+ZnSe and 5e17 $cm^{-3}$ in n-ZnSe, lower temperatures in than 200K showed no current through the device.

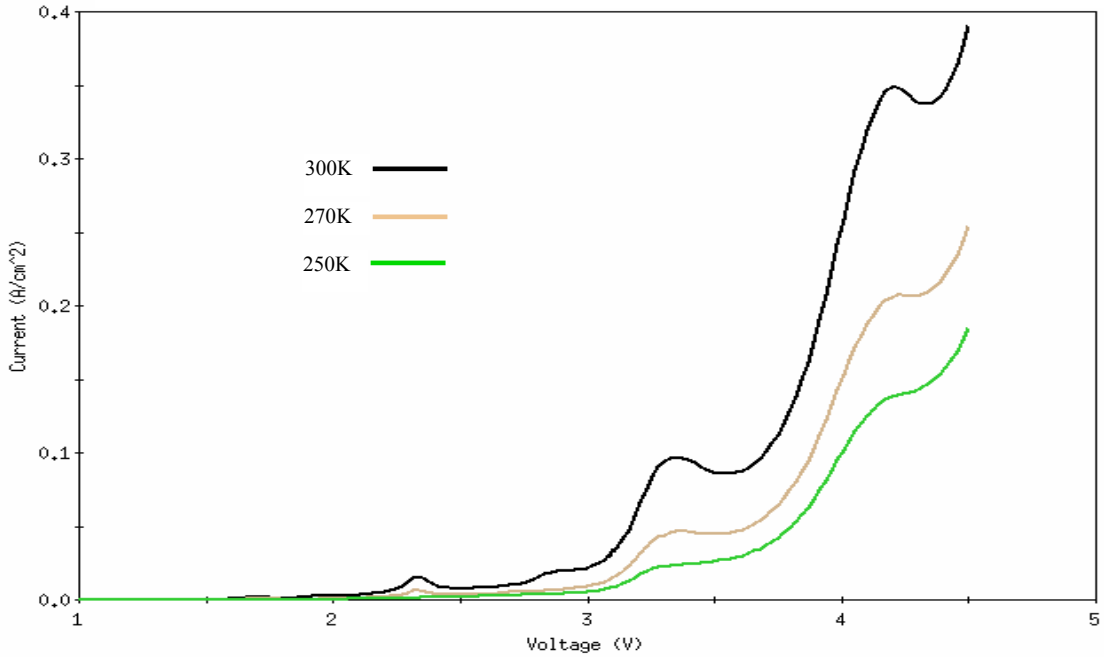


Fig 5.6 ZnSe-BeTe structure with regular doping simulated at 300K, 270K and 250K

Hence experimentally it was found out in that there was a decrease in current density at lower temperatures and in NEMO simulations also showed the same results. For graded doping of 5e18 $cm^{-3}$ in n+ZnSe and 5e17 $cm^{-3}$ in n-ZnSe in the emitter and collectors the Fermi-level was calculated using NEMO.The energy level of the first resonant state in the ZnSe/BeTe RTD for zero bias conditions was calculated using NEMO.The resonant states and Fermi-level is shown in Fig 5.7.The Fermi-level for the given graded doping is $E_F$=0.05203eV and the resonant energy states are,$E_1$=0.1385eV $E_2$=0.2003eV, E3=0.2933eV.The difference between the Fermi-level $E_1$ and $E_F$ was found to be $E_1$- $E_F$= 0.08647eV. The thermal energy $E_T$=KT at 300K is 25meV, therefore the difference is in the order of 3.5KT. The energy difference needs to be as

less as possible for thermally assisted tunneling to be minimal. In order to increase the Fermi-level the contacts can be doped higher.

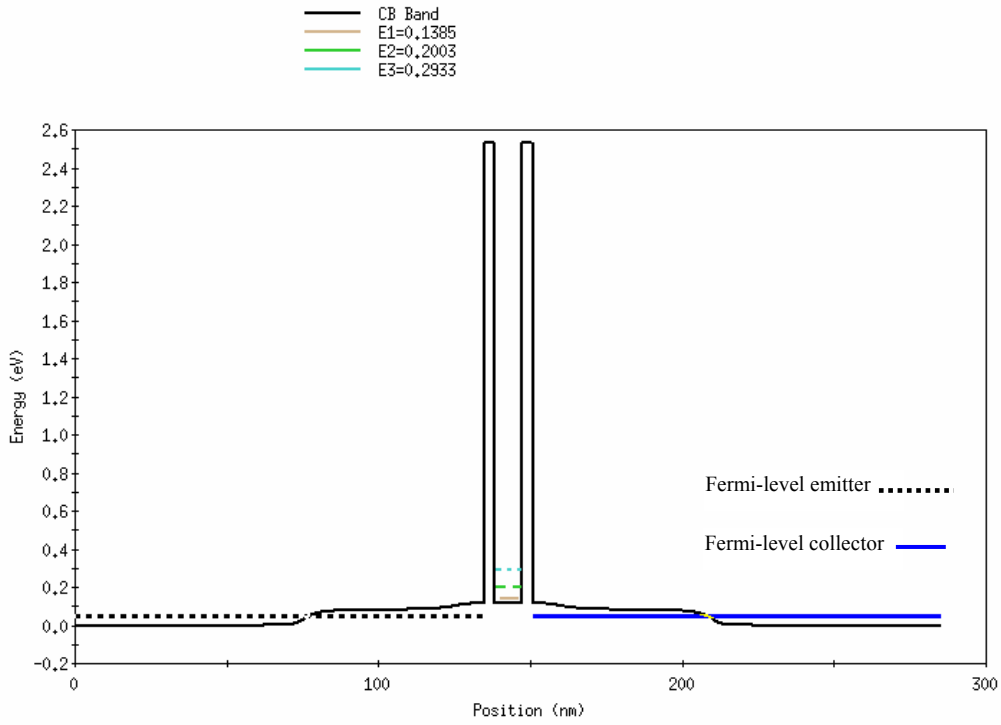


Fig 5.7 Fermi level and resonant states in ZnSe/BeTe RTD

Calculations were made by increasing the doping from 5e18 $cm^{-3}$ in n+ZnSe and 5e17 $cm^{-3}$ in n-ZnSe in the emitter and collectors to 5e19 $cm^{-3}$ in n+ZnSe and 5e18 $cm^{-3}$ in n-ZnSe. Again the energy difference between the Fermi-level and the first resonant state were calculated and found out to be in the order of 2KT.By increasing the doping of the contacts the energy from the Fermi-level to first resonant state decreased by 1.5KT and hence thermally assisted tunneling can be reduced. Another simulation of I-V characteristics with higher doping of 5e19 $cm^{-3}$ in n+ZnSe and 5e18 $cm^{-3}$ in n-ZnSe were done for temperatures of 300K, 270K, 250K shown in Fig 5.8.The figure shows

a decrease in thermally assisted tunneling compared to the regular doping in Fig 5.6.

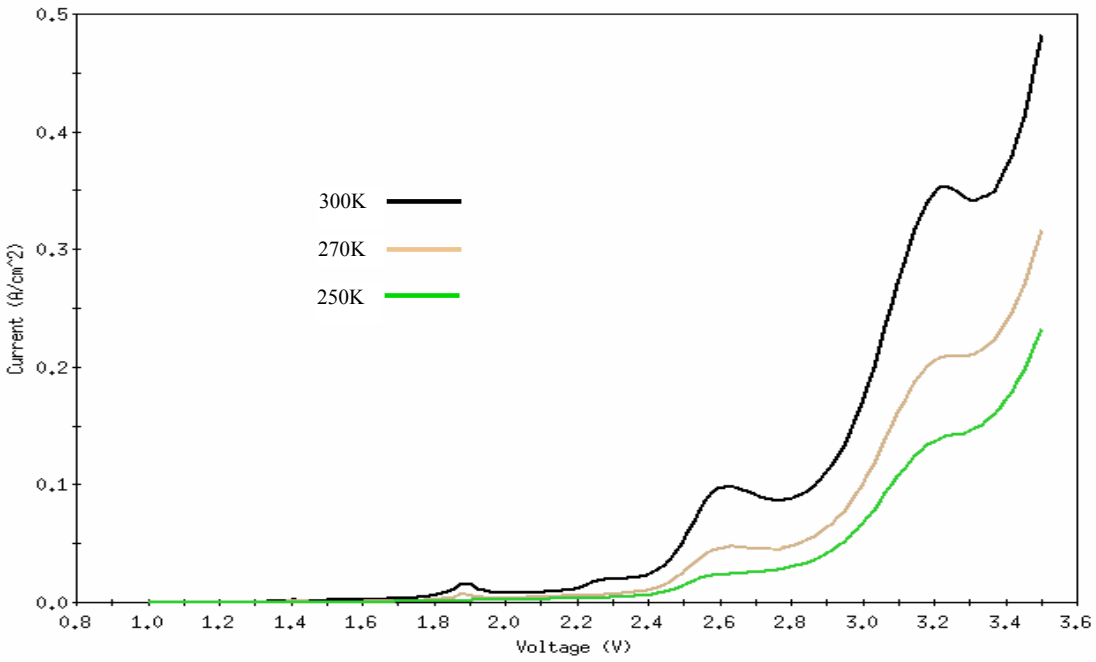


Fig 5.8 ZnSe-BeTe structure with higher doping simulated at 300K, 270K and 250K

The overall current in the I-V characteristics of ZnSe-BeTe RTDs has three components of current contributing to it. The first is the resonant electron tunneling current through the conduction band, the current due to thermal carriers over the barriers and the current from the type-II transitions. Of all these current only the resonant electron tunneling current contributes to NDR and hence PVR. The other current there is no tunneling happening and is mostly a constant increase in current with voltage. The contribution of the thermal and type-II current increases the valley current during off-resonance , hence decreases the PVR. This is the same reason is when the temperature of RTDs are lower there is no contribution from thermal carriers and so the PVR increases. If we can reduce the type-II transitions we can also increase the PVR.

The type-II transitions happen between the conduction band and the valence band, if the Fermi-level is push higher far from the valence band the type-II transitions can be reduced. The method in which type-II transitions can be reduced is by again doping the emitters and collectors to a high level such that the transitions from the conduction band to the valence band is reduced the bands being further spaced apart. Simulations for different doping were done in NEMO shown in Fig 5.9.The increase in PVR by doping depends upon the percentage of current contributed by type-II transitions, if the contribution is less the increase in PVR will be less.

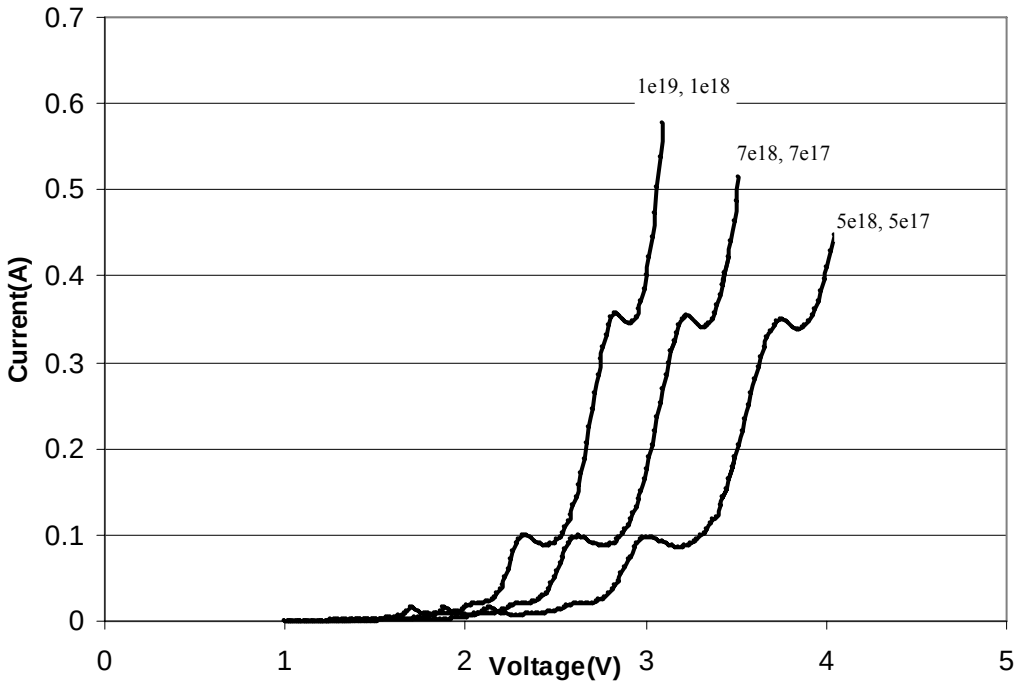


Fig 5.9 I-V simulations showing an increase in PVR by increasing doping

The 3 NDRs are compared for doping of 5e18 $cm^{-3}$ in n+ZnSe and 5e17 $cm^{-3}$ in n-ZnSe denoted as “doping A” and 1e19 $cm^{-3}$ in n+ZnSe and 1e18 $cm^{-3}$ in n-ZnSe denoted as “doping B”.This is shown in Table 5.2.

Table 5.2 PVR increase for change in doping

| | PVR 1 | PVR 2 | PVR 3 |
|---|---|---|---|
| Doping A | 2.077 | 1.128 | 1.0353 |
| Doping B | 2.079 | 1.134 | 1.0357 |

## 5.4 BeSe and ZnTe interfaces in ZnSe/BeTe quantum wells

The structural aspects of grown heterostructures are important, because in the fabrication of heterostructures like quantum well devices materials of different lattice contant are brought together, if they are strained they not only change the band structure but if sufficiently thick layers above the critical thickness are grown they relax to form dislocations at the interfaces. Dislocations disturb the electronic transport through the lattice. The interfaces of RTDs need to be atomically smooth for minimum scattering to take place at the interfaces when electrons are tunneling through the quantum well. The lattice mismatch between ZnSe and BeTe is known to be 0.74%.Although closely lattice matched, the dislocations and defects depend upon the thickness of BeTe barriers and ZnSe wells. $Zn_xBe_{1-x}Te$ with a composition of x =0.08 is lattice matched to ZnSe and x=0.05 is lattice matched to GaAs [41].The composition used as a buffer layer was $Zn_{0.06}Be_{0.94}Te$ which should be between ZnSe and GaAs lattice parameter. The lattice mismatch between GaAs and Si is ~ 4%.The lattice parameter $Zn_{0.06}Be_{0.94}Te$ was calculated theoretically using vegard's law and found to be 5.65538 Å. The lattice mismatch between $Zn_{0.06}Be_{0.94}Te$ and ZnSe was found to be 0.23% and between $Zn_{0.06}Be_{0.94}Te$ and GaAs was found to be 0.036%.Therfore by inserting a buffer layer between ZnSe and Si we are reducing the lattice mismatch from over 4% to ~ 0.23%.

The lattice parameters of ZnSe and BeTe are 5.6687 Å and 5.6269 Å. These materials when grown in alternating layers grow with tensile and compressive stress respectively. The structural quality not only depends upon the thickness ratio of ZnSe and BeTe and the number of periods of quantum wells grown but also the interface configuration being BeSe or ZnTe.A number of groups have studied the structural aspects of ZnSe/BeTe super lattices with the effect of interface configuration, they have characterized their structures using HRTEM( High resolution transmission electron microscopy) and HRXRD (High resolution x-ray diffraction) [37,39,40,43,45].In ZnSe/BeTe RTDs it relates to the effect of thickness ratio between the ZnSe well and BeTe barrier of a single quantum well with the influence of interface configuration on structural quality. The ZnSe/BeTe thickness ratio is checked for between 1.6 to 3.5 with increasing number of periods [39, 40, 43, 45]. There were no dislocations or defects found for smaller super lattices below a period of 20.The smallest super lattice studied was with a period of 5 [39]. The thickness ratio from XRD experiments by Bousquet *et al* [45] concluded that a perfect lattice match can be obtained to GaAs by having a thickness ratio ZnSe/BeTe equal to 2.6.In our case the thickness ratios can be taken into account within the active region and the un-doped spacer, the thickness for un-doped region to quantum-well and again the un-doped spacer are 100 Å ZnSe/ 50 Å BeTe /60 Å ZnSe/ 50 Å BeTe/ 100 Å ZnSe, this region is sandwiched by ZnSe layers. Therefore the lattice constant of the overall structure is around the ZnSe lattice parameter. The thicknesses of the active region can be arranged in such a way that minimum strain is experienced by BeTe layers sitting between ZnSe layers. The alternating ZnSe and

BeTe layers can be increased or decrease to get a constant ratio ZnSe/BeTe thickness. The thickness of barriers and wells also control the number of resonant states and current density.

As understood now that the interfaces of ZnSe/BeTe quantum wells can be either BeSe or ZnTe depending upon growth conditions. The formation of these interfaces as explained earlier alters the electronic properties by changing the band offsets. These no-common atom interfaces also changes the average lattice parameter which in turn changes electronic properties by straining the materials [37].The interface materials although only 1ml-3ml have a adverse effect on the electronic and structural properties [39,40].The lattice contant of BeSe and ZnTe are 5.1477 Å and 6.103 Å respectively. BeSe has a 10% tensile stress and ZnTe has a 7% compressive stress compared to GaAs.The interface type can be controlled to an extent.Chahboun *et al* [81] have grown ZnSe/BeTe structures with different configurations of interfaces and found that the ones only ZnTe-type interfaces had misfit dislocations and the one with BeSe-type interfaces had stacking faults. Song *et al* [43] analyzed ZnSe/BeTe structures with different interfaces and found that the structures with ZnTe-type interfaces have better structural quality than structures with BeSe-type interfaces. It also difficult to control the formation of BeSe interfaces [43, 45], it was found that the formation of BeSe is more likely than ZnTe. In intended samples to be only ZnTe type interfaces XRD revealed that there were a large composition of BeSe-type interfaces [45]. Yamakawa *et al* [78] has calculated the composition of BeSe and ZnTe in interfaces of ZnSe/BeTe structures with different growth conditions. The defects in a grown structure must be

reduced as much as possible. The lattice mismatch between ZnSe and BeTe is inevitable because they are the main materials participating in the formation of the quantum well, but the interfaces highly mismatched can be changed to get better structural quality. Better lattice matching and reduced strains in layers will reduce the dislocations, dislocations are paths for unintended current flow. In case of RTDs the valley current is reduced by reducing structural defects and hence the PVR ratio of these devices can be increased.

# CHAPTER 6

# FUTURE WORK

In order to get symmetrical I-V characteristics in ZnSe/BeTe resonant tunneling diodes, the interfaces in the growth must be changed to equivalent interfaces. If the interfaces can be controlled to be all BeSe interfaces or all ZnTe interfaces during the growth without compromising the structural quality of the heterostructure successful RTDs grown on silicon can be produced. Our group is the first to produce ZnSe/BeTe resonant tunneling diodes on silicon. Different configurations of interfaces can be explored for their effect on structural quality and their effect on electrical characteristics. These structures need to characterized for dislocations and defects in order to reduce them and get better operating characteristics such as PVR. Techniques such as HRTEM (High resolution transmission electron microscopy) and XRD (X-ray diffraction) can be used to characterize defects, structural quality, lattice mismatch and strain effects. The strain effects must be minimized as much as possible, because they not only cause dislocations but also alter the band structure of materials. The compositions of the buffer layer of $Zn_XBe_{1-X}Te$ can be changed and made lattice matched to ZnSe since the whole structure of the RTD is grown on the buffer the structure will be least strained in this way. Another reason is that the interface between the buffer layer and the ZnSe is more important than the interface between buffer layer

and silicon since the electronic transport takes place only in the ZnSe/BeTe layers. The interfaces must be chosen in order to minimize the strain and dislocations.

To get better PVR and better current density the thickness of barriers and well can be changed. By changing the well thickness the number of NDR regions can be increased or decreased. Engineering the triangular potential well by changing the dopant grading or width and increasing the 2D to 2D resonant tunneling sharper resonances are supposed to appear [2]. The dopant gradients in the emitter and collector in the present devices have an un-doped spacer and two regions of different doping. The dopant grading can be made more gradual by increasing the number of doped regions or by using delta-doping in the contacts.

SEM (scanning electron microscopy) and TEM can be used to check for the thicknesses of barriers and wells grown and accordingly changes can be made in the growth. HRTEM can be used for characterizing defects and dislocations. XRD can be used to check for lattice mismatch, strain effects, presence of type interfaces and the composition of ZnSe/BeTe interface. STM (scanning tunneling microscopy) has been widely used for the characterization of interfaces. The dopant profile and segregation of dopant in the contacts comparatively less important than others mentioned above but would prove worthy if there is an experimental method to check for it.

There is very little experimental data available on the band-offsets between the host materials such as ZnSe and BeTe and its interfaces BeSe and ZnTe. By changing the band-offsets to experimental data better quantitative and qualitative simulations can be obtained. The $sp^3s^*$ tight binding parameters sets used can be further tuned to match

experimental data such as band gaps and band-offsets. The best way to change the $sp^3s^*$ tight binding parameters is to implement genetic algorithms, they have been used to change the parameters for various III-V compounds used in NEMO simulations, but none done on II-VI materials. Strain can be included in the $sp^3s^*$ tight binding parameters used for simulations which would produce good quantitative agreement with experimental characteristics. Our group is also the first to produce qualitative I-V simulations of ZnSe/BeTe RTDs using NEMO. There is a genetic algorithm package called PGAPACK used by JPL laboratories at CalTech University which matches experimental characteristics by changing thicknesses of barriers and wells. This can interfaced with NEMO and customized to change band offsets, thicknesses, simulation models and other important parameters which affect the I-V characteristic comparison. In this way simulations can be made easier, faster and more accurate. Resonant tunneling diodes are not only NDR devices which can be used for oscillator, memory and logic applications, but has also served as a test bench to understand important quantum mechanical phenomena. As CMOS technologies shrink to smaller and smaller size and go beyond the quantum limit, quantum electronic devices may become the next workhorse of the semiconductor industry if it meets the reliability and cost of the market. RTDs have already proved to have fast operation, low power consumption and flexibility in design to produce desired output characteristics. RTDs fabricated on silicon hold promising applications when integrated with CMOS technologies. In future when RTDs are implemented in circuits can be used for consumer, military and space electronics.

# APPENDIX A

# MASK DESIGN USING L-EDIT

3-mask layer process for II-VI RTD was designed using L-Edit student version 7.0.This software is freely available. The die size was chosen so that individual dies fit in the 16-pin DIP package. The die spacing was chosen such that individual dies can be cleaved. The minimum feature sizes in the devices were 10um for all mask layers. The alignment mark is placed at the left top corner which has cross-wires of 4um width.

Die size: 4mm by 5mm

Mask type: Soda lime glass

Mask size: 3 inch

It was suggested Clear field/Chrome geometry (All features drawn in design be chrome and rest clear) be used for all masks and change the photo resist to be negative or positive as needed.

**First layer: Mesa layer**

This layer will have features of 10um, 25um, 50um, 150um, 300um and 450um diameter devices. Apart from the devices which are circles of different sizes this layer also contains the back contact which is basically a large area compared to the device size and is brought about by using the rest of the area of the die.

A positive resist need to be used and the aluminum needs to be etched off. The step using either the aluminum as mask or the photo resist retained the II-VI layers ZnSe and BeTe needs to be etched down to the bottom doped layers and until NDR is seen.

**Second layer: Etch holes layer**

A layer of dielectric for insulating these devices is to be put and holes are to be etched through the dielectric.

Dielectric: Sputtered silicon dioxide, sputtered silicon nitride.

**Third layer: Metal lift-off layer**

The metal in third layer makes contact with the first layer metal through the etched dielectric and bonding pads of 200um by 200um are brought away from the device so that the bonding does not affect the devices. The bonding pads are sitting on a dielectric. The fingers used for connecting the device to the bonding pads are 10um for smaller devices and 20um for bigger devices of 150um, 300um and 450um.In order to minimize the series resistance for smaller devices of 10um and 25um a four probe configuration for measurement 2 fingers from the device for voltage and 2 fingers for current measurements.

Mask 1: Red

Mask 2: Blue

Mask 3: Grey

All the colors shown are made of chrome to block light and the rest of the area is made clear glass. Since the minimum feature size was 4um the soda lime glass is chosen. If features size is smaller than 1um then quartz needs to be used.

Mask 1 and Mask 2

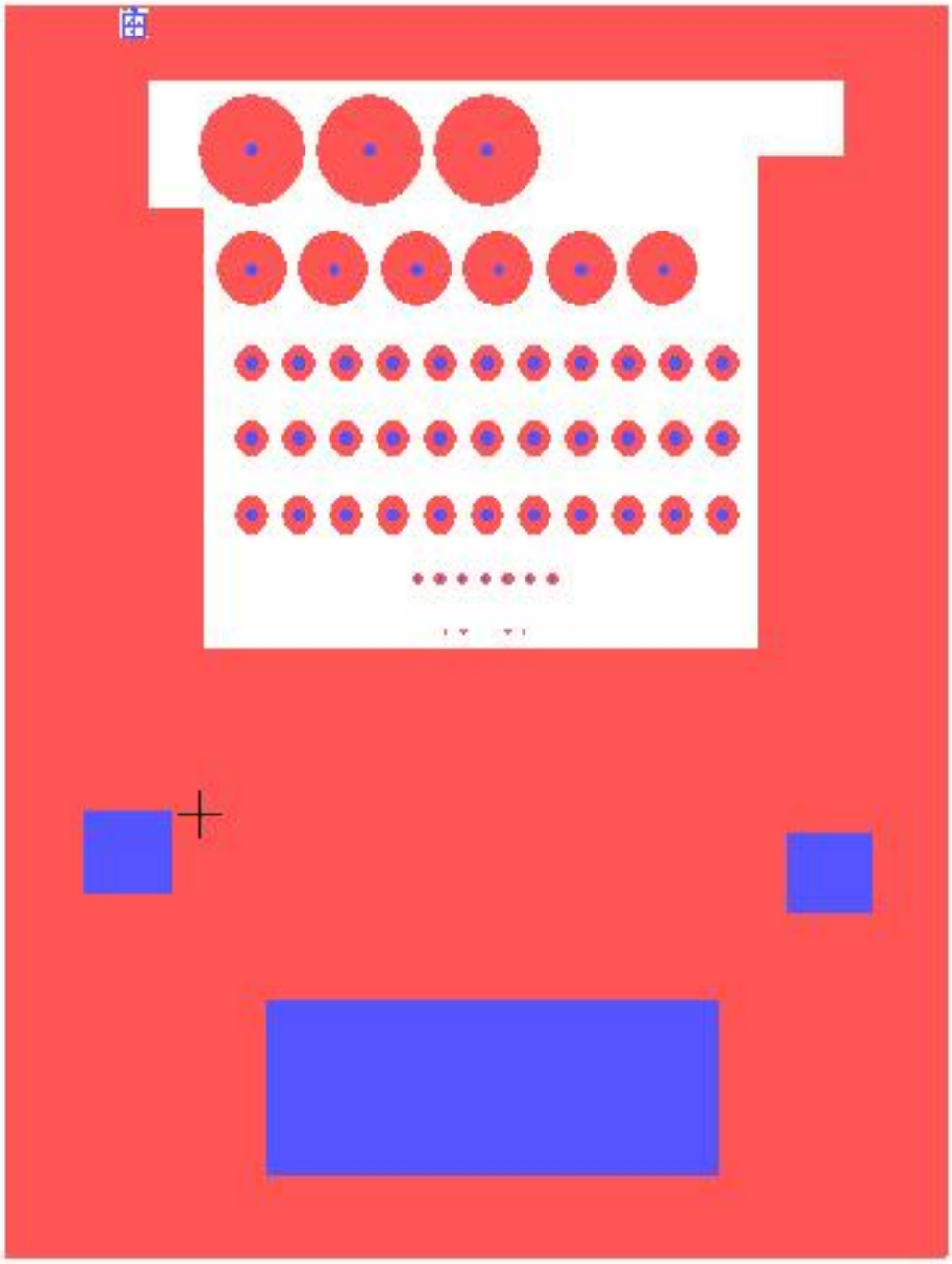

Mask 3:

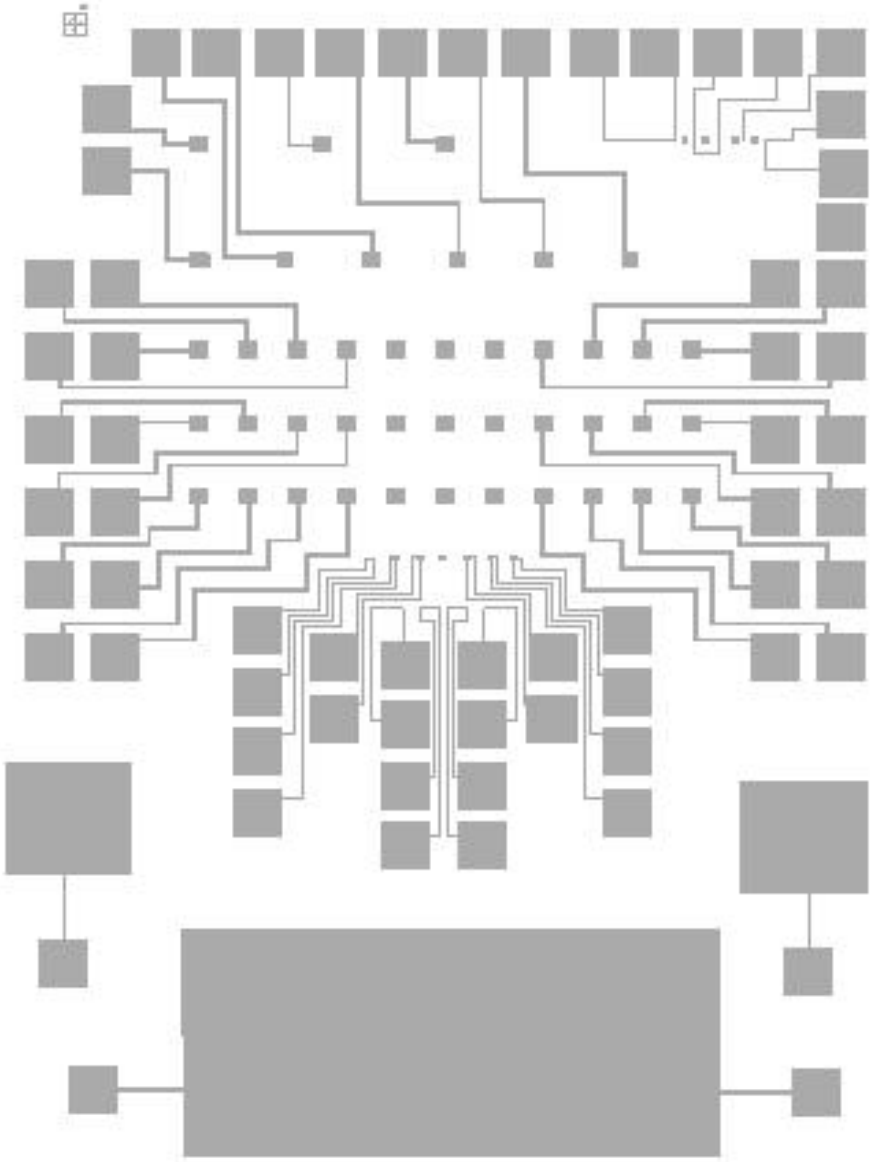

Mask 1, 2 and 3

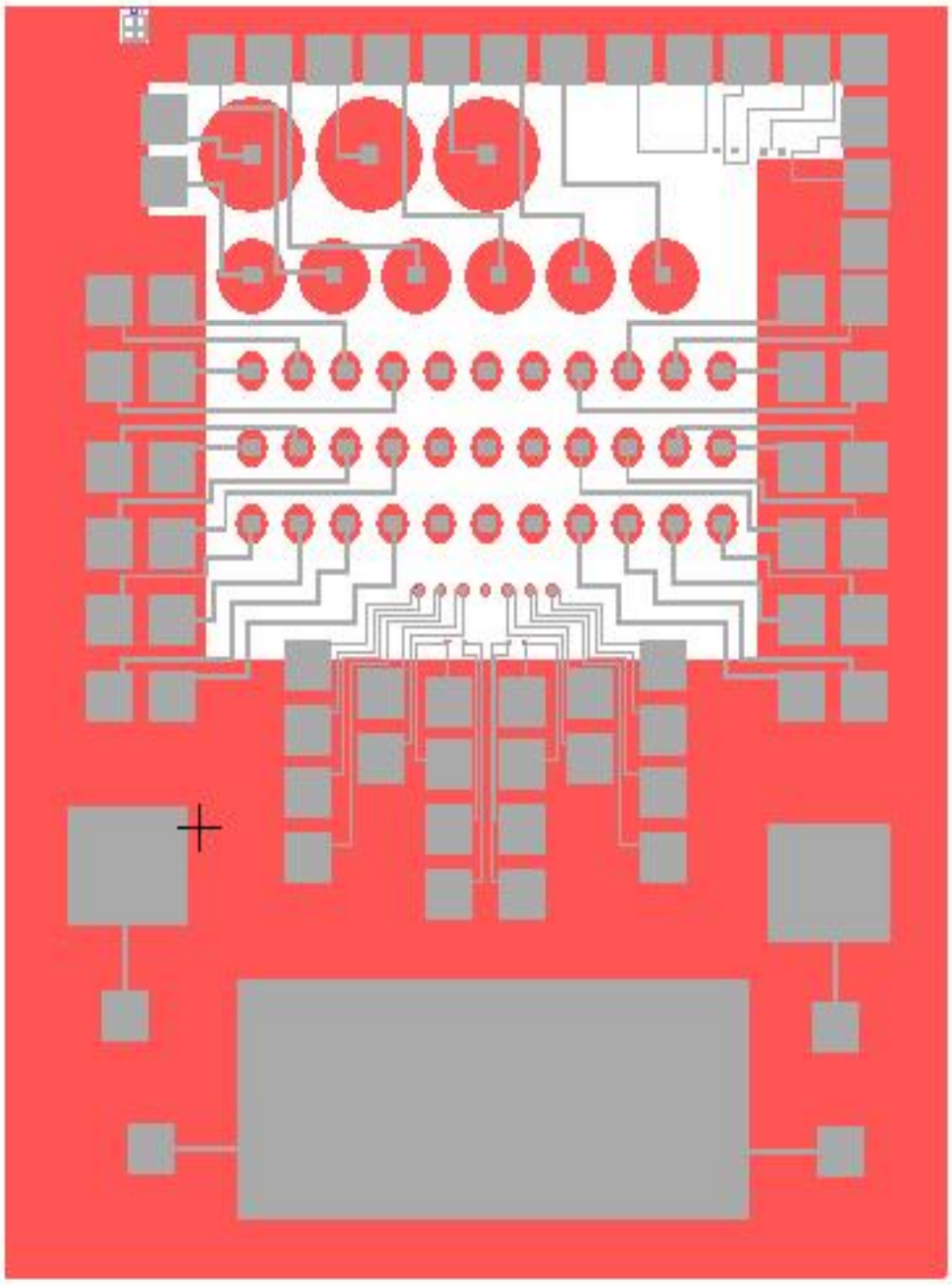

The L-Edit files need to be converted into GDSII format for mask makers. The student version of L-Edit does not contain the file conversion from tanner database files to GDSII format. The L-edit format is .tdb or tanner database file. The GDSII format is a binary format in which the circles are converted into n-sided polygons. In the conversion software the number of vertices of the polygon defines the reproducibility of the circles's edges. In the L-Edit professional version the maximum number of vertices resulted in rough edges of the circles and circles with smaller dimensions were totally disfigured. The L-edit professional version was used to convert it into CIF format or California interchange format. From CIF format the designs were converted GDSII format using coventor software.

# APPENDIX B

# NEMO OPERATION

NEMO software is a quantum device simulator specifically developed by Raytheon TI for resonant tunneling diodes. NEMO 1D is the software used in this work which simulates different characteristics along one dimension. NEMO 1D has two versions NEMO 1D v3.0 and NEMO 1D v4.0.We used NEMO 1D v4.0 for our simulations. . Two versions of NEMO are available, one is installed on the gamma2 server and another on the rir2001 server at the High Performance Computing center at UTA. Using SSH secure shell client software one can connect to the servers and also an X-Windows server is required to view the GUI for NEMO. For this Exceed for Win32 v.6.2.0.0 is used. These software require an installation CD.

NEMO can be run on

1) GUI on the computer
2) Batch mode on rir2001.uta.edu
3) Server at UFL using Web interface.

1) GUI on the computer:

Gamma2 server is a SunOS, and this is an older version of NEMO i.e. v3.0. It does not support batch processing, but multiple simulations can be run directly using the graphical interface. Both gamma2 and rir2001 servers require a login name and a password for access.

Host : gamma2.uta.edu

Username : ****  Password : ******

Host : rir2001.uta.edu

Username : ****  Password : ******

Once logged in the following prompt will show up.

**[kirk@rir2001 ~]$**

The ric 2016 node works for NEMO v4.0 well, the following command needs to be typed.

**ssh kirk@ric2016**

You will be prompted for a password again which is the same password used for login like shown below.

**kirk@ric2016's password:**

Once this is done the environment variable needs to be set to the computer's IP address using the following command.

**setenv DISPLAY "IP address of computer": 0.0**

Once this is done, just type "nemo" and return, this will cause the GUI of NEMO to open in windows and files and simulations can be worked on through the GUI interface.

2) Batch mode operation of NEMO

NEMO v.4.0.0 is installed on a Redhat Linux platform at the High Performance Computing center at UTA on the rir2001 server. In order to run it, we use batch processing which submits the job to a queue with compute nodes on it. We use the 'int' queue that supports serial processing. The hosts on the queue are as follows:

- ric2021  00:10:18:00:45:1A
- ric2022  00:10:18:00:44:74

- ric2023 00:10:18:00:44:7C
- ric2024 00:10:18:00:45:1D

The hardware addresses of these nodes are shown beside them. These nodes are for serial processing and are apt for NEMO simulations. The hardware address typically will not change unless some hardware changes are made. To obtain the hardware address the following line needs to be executed on rir2001.

kirk@rir2001> bsub –q int –m ric2021 "/sbin/ifconfig eth0 | grep 'HWaddr' | sed 's/:/ /' > /home/kirk/outputfile"

In the above example, 'ric2021' maybe replaced by any other node name. The output is saved in the file called 'outputfile' in the home/kirk directory. The license for NEMO needs to be valid on the above mentioned compute nodes else NEMO will not run in the batch mode. The license obtained is placed in the nemo/bin and nemo/lib folder. To run in batch mode, the .nem file is first setup for the kind of simulation to be conducted. This could be done either by opening the .nem file using wordpad or by opening it in the GUI interface on rir2001 as follows:

kirk@rir2001> setenv DISPLAY <ip address of your machine> :0.0

kirk@rir2001> nemo

Once the simulation is setup, the job is submitted to one of the nodes on the queue as follows:

kirk@rir2001> bsub –q int –m ric2021 “nemo_b /home/kirk/test.nem > /home/kirk/nemo_output”

This will submit the job to ric2021 and if any error occurs it will be stored in a file called ‘nemo_output’. If the simulation runs successfully, ‘nemo_output’ will not contain anything and the outputs generated by NEMO are created as files which can be opened in using the GUI interface. eg.: If an IV file is generated, it will be stored in the same folder with an extension .nd_iv

To keep a check on the status of the job several UNIX commands maybe used. Some of them are listed below.

bhist –u kirk

lists all the jobs submitted by user kirk.

bhist –l –u kirk

lists jobs submitted by user kirk in detail.

bjobs <job ID>

lists information about the job with the mentioned job ID.

bjobs –l <job ID>

Lists the above information in more detail.

3) Server at UFL using Web interface

This server can be accessed through a java enabled web interface called In-VIGO by logging into the following URL

http://invigo.acis.ufl.edu/Login

After logging into In-VIGO click on “My sessions” link. You should see a NEMO 1D workspace with an “Open VNC window” link, clicking this link will open a VNC session window with a “xterm” window.

“xterm” is a window in which the interface is with the NEMO program simply type “nemo” in the window and return, NEMO will open up as in the regular GUI.

For each username or login there is a particular folder within “My sessions” itself.

The output files are stored in a NEMO output folder within username’s folders.

The files to be simulated need to be uploaded to the username’s folders which is local space allocated within the NEMO server to be accessed and simulated.

-NEMO usage with GUI on UFL server has a readme file in each individual account.

-Other issues regarding networking and server working can be directed to the following.

In-VIGO Administrator (acis-invigo@acis.ufl.edu) ACIS - ECE -UFL

REFERENCES

[1] R. Tsu , L. Esaki, "Tunneling in a finite superlattice," *Appl. Phys. Lett,* vol. 22, pp. 562, 1973.

[2] H.Mizuta, T. Tangue *The Physics and applications of resonant tunneling diodes,* Cambridge University Press, 1995.

[3] Jian Ping Sun, Haddad, G.I., Mazumder, P. Schulman, J.N," Resonant tunneling diodes: models and properties "*Proceedings of the IEEE,* Volume 86, Issue 4, April 1998 Page(s):641 - 660

[4] T.Inata, S.Muto, "A Pseudomorphic $In_{0.53}Ga_{0.47}As$/AlAs Resonant Tunneling Barrier with a Peak-to-Valley Current Ratio of 14 at room temperature," *Jpn. J. Appl. Phys,* vol. 26, pp. L1332, August 1987.

[5] E. Broekaert, G. Fonstad, "$In_{0.53}Ga_{0.47}As$/AlAs resonant tunneling diodes with peak current densities in excess of 450 kA/cm$^2$," *J. Appl. Phys,* vol. 68, pp. 4310, 15 October 1990.

[6] U. Lunz, M. Keim,G. Reuscher, F. Fischer, K. Schüll, A. Waag, G. Landwehr "Resonant electron tunneling in ZnSe/BeTe double-barrier, single-quantum-well heterostructures" *Journal of Applied Physics,.* Volume 80, Issue 11, pp. 6329-6332, December 1, 1996

[7] K. Ismail, B. S. Meyerson, P. J. Wang "Electron resonant tunneling in Si/SiGe double barrier diodes" *Applied Physics Letters,* Volume 59, Issue 8, pp. 973-975, August 19, 1991

[8] D.K Blanks,G. Klimeck,R. Lake. Jovanovic, D.Bowen, R.C.Fernando.C, W.R.Frensley "NEMO-general release of a new comprehensive quantum device simulator " *IEEE International Symposium on Compound Semiconductors*, 1997 Pages 639-642

[9] Robert.F.Pierret, *Advanced semiconductor fundamentals*, Volume-VI, Modular series on solid state devices, Pearson education, 2003.

[10] E. O. Kane, "The k.p method," *Semiconductors and Semimetals,* vol. 1, pp. 75, 1966.

[11] K.V.Rousseau, K. L. Wang,J. N. Schulman “Gamma and X-state influences on resonant tunneling current in single- and double-barrier GaAs/AlAs structures*”.Appl.Phys.Letters* 54, 1341 (1989).

[12] P. Vogl, H. P. Hjalmarson, and J. D. Dow” A semi-empirical tight-binding theory of the electronic structure of semiconductors”. *Phys. Chem. Solids,* 44, 365 (1983).

[13] T. B. Boykin, G. Klimeck, R. C. Bowen, and F. Oyafuso,”Incorporation of incompleteness in the k-p perturbation theory” *Phys. Rev. B 66, 125207 (2002).*

[14] R. C. Bowen, G. Klimeck, R. K. Lake, W. R. Frensley and T. Moise, "Quantitative simulation of a resonant tunneling diode," *J. Appl. Phys.,* vol. 81, pp. 3207, April 1997

[15] H.Kosina, G.Klimeck, M.Nedjalkov, S. Selberherr "Comparison of Numerical Quantum Device Models", *International Conference on Simulation of Semiconductor Processes and Devices, September 3-5, 2003*

[16] Datta, S “The non-equilibrium Green's function (NEGF) formalism: An elementary introduction” *International Electron Devices Meeting, 2002, pages: 703- 706*

[17] Raytheon TI Systems, *NEMO Documentation - User’s Guide, Theory Guide, Technical Guide,* 1998.

[18] R. Lake, G. Klimeck, R.C. Bowen, D. Jovanovic.” Single and multiband modeling of quantum electron transport through layered semiconductor devices” *J. of Appl. Phys.*, 81, 7845-7869 (1997)

[19] D. J. Chadi” Spin-orbit splitting in crystalline and compositionally disordered semiconductors”, *Phys. Rev. B,* Vol 16, pp 790 (1977)

[20] Gerhard Klimeck, Dan Blanks, Roger Lake, R. Chris Bowen et.al., Nanoelectronic Modeling (NEMO) : A New Quantum Device Simulator," *NASA Technical Journal,* 1997

[21] Gerhard Klimeck,"Quantum and semi-classical transport in RTDs in NEMO 1-D", *Journal of Computational Electronics,* Vol 2, pg. 177-182, (2003)

[22] A.Seabaugh R. Lake, "Tunnel Diodes," *Encyclopedia of applied physics* Vol.20 VCH, NY, 1996,p. 335

[23] K. Ismail, B. S. Meyerson, Wang” Electron resonant tunneling in Si/SiGe double barrier diodes” *Applied Physics Letters -August 19, 1991,*Volume 59, Issue 8, pp. 973-975

[24] Rommel, S. L. Dillon, T. E. Dashiell, M. W. Feng, H. Kolodzey, J. Berger, P. R. Thompson, P. E. Hobart, K. D. Lake, R. Seabaugh, A. C "Room temperature operation of epitaxially grown Si/SiGe/Si resonant interband tunneling diodes" *Applied Physics Letters,* Vol 73, Number 15, pages 2191-2193,1998

[25] F.Rinaldi "Basics of Molecular beam epitaxy (MBE)", *Annual report on optoelectronics* , University of Ulm, 2002.

[26] P. Mazumder, S. Kulkarni, M. Bhattacharya, J. P. Sun, and G. I. Haddad, "Digital Circuit Applications of Resonant-Tunneling Devices," *Proceedings of the IEEE,* vol. 86, no. 4, pp. 664-686, April 1998

[27] J. P. A. van der Wagt, A. C. Seabaugh,E. A. Beam "RTD/HFET Low Standby Power SRAM Gain Cell " *IEEE Electron Device Letters*, Vol 19, No 1, January 1998

[28] Wei, S.-J, Lin, H.C." Multivalued SRAM cell using resonant tunneling diodes" *IEEE Journal of Solid-State Circuits,* Volume 27, Issue 2,1992,pp:212 - 216

[29] T.-H. .Kuo, H.C.Lin, R.C.Potter, D.Shupe, " A Novel A/D Converter Using Resonant Tunneling Diodes", *IEEE Journal of Solid-state Circuits*, vo1.26, No.2, pp. 145-149,1991

[30] S.-J.Wie, H.C.Lin, R.C.Potter,D.Shupe,"A Self-Latching A/D Converter Using Resonant Tunneling Diodes", *IEEE Journal of Solid-state Circuits*, v01.28, No.6, pp.697-700, 1993

[31] E.R.Brown, J.R.Soderstrom, T.C.McGill, "Oscillations up to 712 GHz in InAs/AISb Resonant-Tunneling Diodes", *Applied Physics Letters*, vo1.58, no. 20, pp. 2291-2293,1991

[32] Lin, H.C. "Resonant tunneling diodes for multi-valued digital applications" *Proceedings, Twenty-Fourth International Symposium on Multiple-Valued Logic* 25-27 May 1994

[33] L.Esaki, R.Tsu "Superlattice and negative differential conductivity in semiconductors",*IBM research note RC 2418.* Yorktown heights,NY IBM 1969

[34] L. Esaki and L. L. Chang" New Transport Phenomenon in a Semiconductor Superlattice" *Phys. Rev. Lett,* Vol 33, 495–498 (1974)

[35] John H. Davies, *The Physics of Low Dimensional Semiconductors,* Cambridge University Press, 1998

[36] E.Maldonado, K.Clark S. Bhandaru, W.Kirk "Growth of ZnSe/BeTe double-barrier quantum-well heterostructure on vicinal Si (100) surfaces by Molecular Beam Epitaxy " *Nanostructures:Electrical,optical and structural properties*,2005 APS March meeting Los Angeles, CA

[37] A. Waag,M. Keim, G. Reuscher, T. Gerhard, A.V. Platonov, D.R. Yakovlev, L.W. Molenkamp, G. Landwehr "BeTe-ZnSe type-II heterojunctions" *Journal of Crystal Growth* 214/215 (2000) 316-320

[38] A. Waag, F. Fischer, H.-J. Lugauer, T. Baron, K. Schiill, U. Zehnder,, U. Lunz, M. Keim, G. Reuschera, G. Landwehr " Novel beryllium containing II-VI compounds: basic properties and potential applications" *Journal of Crystal Growth,*184/185, pp l-10,1998.

[39] D. Gerthsen,T. Walter, F. Fischer, T. Gerhard, A. Waag, G. Landwehr "Structural properties and relaxation behavior of short-period BeTe/ZnSe superlattices" *Journal of Crystal Growth,* 214/215, pp 330-334, 2000.

[40] T. Walter, A. Rosenauer, R. Wittmann, D. Gerthsen, F. Fischer, T. Gerhard, A. Waag," Structural Properties of BeTe/ZnSe superlattices " *Phys. Rev. B,* Vol 59, pp 8114, 1999.

[41] M.W. Cho, S.K. Hong, J.H. Chang, S. Saeki, M. Nakajima, T. Yao "MBE grown BeTe and ZnBeTe films as a new p-contact layer of ZnSe-based II-VI lasers" *Journal of Crystal Growth,*214/215,pp487-491, 2000.

[42] Robin F. C. Farrow "Molecular Beam Epitaxy-Applications to key materials", *Noyes publications* , Park Ridge, NJ, 1995.

[43] J.S. Song, J.H. Chang, M.W. Cho, T. Hanada, T. Yao "Growth and characterization of ZnSe/BeTe superlattices "*Journal of Crystal Growth,*229, pp 104–108 , 2001.

[44] Leslie A. Kolodziejski , Robert L. Gunshor , Arto V. Nurmikko " Wide bandgap II-V_ heterostructure for blue/green optical sources-key material isuues "*Annual review Material science,*25, pp 711-755, 1995.

[45] V. Bousquet, M. Lauk, E. Tournie , J.-P. Faurie "Investigations by high-resolution X-ray diffraction (HRXRD) and transmission electron microscopy (TEM) of (BeTe/ZnSe) superlattices grown by molecular beam epitaxy onto GaAs buffer epilayer" *Journal of Crystal Growth,*201/202, pp 498-501,1999

[46] M. W. Cho, J. H. Chang, S. Saeki, S. Q. Wang, T. Yao "Characteristics of BeTe films grown by molecular beam epitaxy" *Journal of Vacuum Science & Technology A: Vacuum, Surfaces, and Films,* March 2000, Volume 18, Issue 2, pp. 457-460

[47] Chen, W. Kahn, A. Soukiassian, P. Mangat, P. S." ZnSe(100): The surface and the formation of Schottky barriers with Al and Au" *Journal of Vacuum Science & Technology B: Microelectronics and Nanometer Structures,* Volume 12, Issue 4, July 1994, pp.2639-2645

[48] Schull, K. et al. "Non-metal in situ and ex situ ohmic contacts to a n-ZnSe." *Semicond. Sci. Technol*. Vol 12, pp 485(1997).

[49] Y. X. Wang , Paul H. Holloway "Indium ohmic contacts to n-ZnSe "*AIP Conference Proceedings ,* May 5, 1991, Volume 227, Issue 1, pp. 134-137

[50] T.Miyajima, H.Okuyama, K.Akimoto "Ti/Pt/Au Ohmic Contacts to n-Type ZnSe "*Jpn. J. Appl. Phys*. Vol. 31 (1992) L1743-L1745

[51] J. C. Slater,G. F. Koster "Simplified LCAO Method for the Periodic Potential Problem" *Phys. Rev*. 94, 1498–1524 (1954)

[52] C.M.Goringe, D.R.Bowler, E.Hernández "Tight binding modeling of materials", *Reports on Progress in Physics* 60 (12), 1447 (1997)

[53] T.Sandu"Numerical simulations of quantum devices", *Physics dissertation, Texas A&M University.*2002

[54] J.M.Jancu, R.Scholz, F.Beltram, F.Bassani "Empirical *spds** tight-binding calculation for cubic semiconductors: General method and material parameters "*Phys. Rev. B* 57, 6493–6507 (1998)

[55] G.Klimeck, C.H. Salazar-Lazaro, A.Stoica, T. Cwik, ""Genetically Engineered" Nanoelectronics," *The First NASA/DOD Workshop on Evolvable Hardware,* 1999. p. 247

[56] G.Klimeck, R.Bowen, T.B.Boykin, T.A.Cwik "sp3s* Tight-binding parameters for transport simulations in compound semiconductors" *Superlattices and Microstructures,* Vol. 27, No. 5/6, 2000

[57] G.Klimeck, R.C.Bowen, T.B.Boykin, C.S.lazaro "Si tight-binding parameters from genetic algorithm fitting" *Superlattices and Microstructures,* Vol. 27, No. 2/3, 2000

[58] G.Klimeck "NEMO 1-D: the first NEGF-based TCAD tool", *IEEE SISPAD 2004, Munich, Germany,* September 2-4, 2004

[59] S.Datta "Nanoscale device modeling: the Green's function method" *Superlattices and Microstructures,* Vol. 28, No. 4, 2000

[60] R.Lake, S. Datta "Non-equilibrium Green's-function method applied to double-barrier resonant-tunneling diodes" *Phys. Rev. B* 45, 6670–6685 (1992)

[61] D.S. Fisher, P.A. Lee "Relation between conductivity and transmission matrix" *Phys. Rev. B* 23, 6851–6854 (1981)

[62] G.Klimeck, R. Lake, R. C. Bowen, W.R. Frensley "Quantum device simulation with a generalized tunneling formula" *Appl. Phys. Lett.* 67 (17), 23 October 1995

[63] L.Zhu, L.Zhang "Electronic structure and interfacial properties of BeTe/Si, BeTe/Ge, and BeTe/SiGe super lattices "*J. Phys. Condens. Matter* 9 (1997) pp 8055-8064

[64] D. J. Chadi "Spin-orbit splitting in crystalline and compositionally disordered semiconductors" *Phys. Rev. B* 16, 790–796 (1977)

[65] M. Rabah , B. Abbar , Y. Al-Douri , B. Bouhafs , B. Sahraoui " Calculation of structural, optical and electronic properties of ZnS, ZnSe, MgS, MgSe and their quaternary alloy MgZnSSe " *Materials Science and Engineering* B100 (2003) 163-171

[66] Ivchenko EL, Nestoklon MO "Lateral optical anisotropy of type-II interfaces in the tight-binding approach " *Physical review B,*70 (23): Art. No. 235332 Dec 2004

[67] T.Sandu , W. P. Kirk "Generalized band anticrossing model for highly mismatched semiconductors applied to BeSeTe" *Phys. Rev. B,*72, 073204 (2005)

[68] D. Bertho, D. Boiron, A. Simon, C. Jouanin C. Priester "Calculation of hydrostatic and uniaxial deformation potentials with a self-consistent tight-binding model for Zn-cation-based II-VI compounds" *Phys. Rev. B,*44, 6118–6124 (1991*)*

[69] F.Bernardini, M. Peressi, V.Fiorentini "Band offsets and stability of BeTe/ZnSe (100) heterojunctions" *Phys. Rev. B 62, R16302–R16305 (2000)*

[70] D. J. Stukel "Energy-Band Structure of BeS, BeSe, and BeTe", *Phys. Rev. B,*2, 1852–1858 (1970)

[71] A. R.Ponce,D. Olguín, I. H.Calderón "Calculation of the effective masses of II-VI semiconductor compounds" *Superficies y Vacío* 16(2), 26-28, June 2003

[72] D. R. Yakovlev, A. V. Platonov, E. L. Ivchenko, V. P. Kochereshko, C. Sas, W. Ossau, L. Hansen, A. Waag, G. Landwehr,L. W. Molenkamp "Hidden In-Plane Anisotropy of Interfaces in Zn(Mn)Se /BeTe Quantum Wells with a Type-II Band Alignment" *Phys. Rev. Lett*. 88, 257401 (2002)

[73] C. Priester, Y. Foulon, and G. Allan " Role of localized interface states at type-II hetero-junctions " *Phys. Rev. B* 49, 2919–2922 (1994)

[74] S. V. Zaitsev, A. A. Maksimov, P. S. Dorozhkin, V. D. Kulakovskii, A. Waag "Electric-field effects on the radiative recombination in type-II ZnSe/BeTe heterostructures with equivalent and nonequivalent interfaces" *Phys. Rev. B* 66, 245310 (2002)

[75] S. V. Zaitsev, A. A. Maksimov,V. D. Kulakovskii, I. I. Tartakovskii D. R. Yakovlev, W. Ossau, L. Hansen,G. Landwehr A. Waag "Interface properties and in-plane linear photoluminescence polarization in highly excited type-II ZnSe/BeTe heterostructures with equivalent and nonequivalent interfaces" *Journal of Applied Physics*, Vol. 91, No. 2, pp. 652–657, 15 January 2002

[76] M. Nagelstrasser, H. Dröge,F. Fischer, T. Litz, A. Waag"Band discontinuities and local interface composition in BeTe/ZnSe heterostructures" *Journal of Applied Physics,April 15, 1998,* Volume 83, Issue 8, pp. 4253-4257

[77] I. Yamakawa Y. Akanuma R. Akimoto A. Nakamura "Scanning-tunneling-microscopy observation of heterojunctions with a type-II band alignment in ZnSe/BeTe multiple quantum wells" *Appl. Phys. Lett*. 86, 153112 (2005)

[78] I.Yamakawa, Y. Akanuma, B. Sheng Li," Composition Profile of ZnSe/BeTe Multiple Quantum Well Structures Studied by Cross-Sectional Scanning Tunneling Microscopy" *Japanese Journal of Applied Physics,*Vol. 44, No. 43, 2005, pp. L 1337–L 1340

[79] B. Z. Nosho W. H. Weinberg .W. Barvosa-Carter, A. S. Bracker, R. Magno, B. R. Bennett, J. C. Culbertson, B. V. Shanabrook, Whitman "Characterization of AlSb/InAs surfaces and resonant tunneling devices" *Journal of Vacuum Science & Technology B: Microelectronics and Nanometer Structures,* July 1999, Volume 17, Issue 4, pp. 1786-1790

[80] B G R Rudberg" Interface roughness and asymmetric current-voltage characteristics in resonant tunneling " *Semicond. Sci. Technol.* Vol 5,pp 600-603,1990

[81] A. Chahboun, V. Fink, M. Fleischauer, and K. L. Kavanagh R. P. Lu "Ballistic electron emission microscopy studies of ZnSe–BeTe heterojunctions*" Journal of Vacuum Science & Technology B: Microelectronics and Nanometer Structures* , July 2002 Volume 20, Issue 4, pp. 1781-1787

## BIOGRAPHICAL INFORMATION

Moshe Davis was born on October 14, 1981 at Chittoor, India. He did his Bachelors in Electronics Engineering from University of Madras, India. He finished his Masters of Science at the University of Texas at Arlington with a thesis in the focus of Quantum electronic devices under the supervision of Dr Wiley Kirk. His research included simulation, fabrication and characterization of resonant tunneling diodes. His interests lie in semiconductor devices, semiconductor manufacturing and quantum devices.